UC-426

# FAST ELECTRON GENERATION AND TRANSPORT IN A TURBULENT, MAGNETIZED PLASMA

Matthew Randall Stoneking

DOE/ER/53198-239

May 1994

NOTICE



Printed in the United States of America
Available from
National Technical Information Service
U.S. Department of Commerce
5285 Port Royal Road
Springfield, VA 22161

NTIS Price codes
Printed copy: A08
Microfiche copy: A01

# FAST ELECTRON GENERATION AND TRANSPORT IN A TURBULENT, MAGNETIZED PLASMA

by

MATTHEW RANDALL STONEKING

A thesis submitted in partial fulfillment of the

requirements for the degree of

Doctor of Philosophy

(Physics)

at the

UNIVERSITY OF WISCONSIN-MADISON

1994

FAST ELECTRON GENERATION AND TRANSPORT
IN A TURBULENT, MAGNETIZED PLASMA

Matthew Randall Stoneking
Under the supervision of Assistant Professor Samuel Hokin
at the University of Wisconsin-Madison

## ABSTRACT

The nature of fast electron generation and transport in the Madison Symmetric Torus (MST) reversed field pinch (RFP) is investigated using two electron energy analyer (EEA) probes and a thermocouple calorimeter. The parallel velocity distribution of the fast electron population is well fit by a drifted Maxwellian distribution with temperature of about 100 eV and drift velocity of about $2\text{x}10^6$ m/s. Cross-calibration of the EEA with the calorimeter provides a measurement of the fast electron perpendicular temperature of 30 eV, much lower than the parallel temperature, and is evidence that the kinetic dynamo mechanism (KDT) is not operative in MST. The fast electron current is found to match to the parallel current at the edge, and the fast electron density is about $4\text{x}10^{11}$ $cm^{-3}$ independent of the ratio of the applied toroidal electric field to the critical electric field for runaways ($E_\phi/E_{crit}$). Time resolved measurements of the fast electron distribution indicate that it is not directly correlated with $E_\phi/E_{crit}$ in a single discharge. First time measurements of magnetic fluctuation induced

particle transport are reported. By correlating electron current fluctuations with radial magnetic fluctuations the transported flux of electrons is found to be negligible outside r/a~0.9, but rises the level of the expected total particle losses inside r/a~0.85. A comparison of the measured diffusion coefficient is made with the quasilinear stochastic diffusion coefficient. The measured diffusion is found to be 500 $m^2/s$, smaller than the quasilinear value of 2000 $m^2/s$. Evidence exists that the reduction of the transport is due to the presence of a radial ambipolar electric field of magnitude 500 V/m, that acts to equilibrate the ion and electron transport rates. The convective energy transport associated with the measured particle transport is large enough to account for the observed magnetic fluctuation induced energy transport in MST.

## Acknowledgments

I thank my advisor, Dr. Samuel Hokin, for taking me on, advising me, guiding me, and often letting me struggle on my own as I pursued my degree. I have had an enormous amount of scientific assistance and collaboration from all members of the MST team. I would especially like to thank the plasma faculty, scientists and post-docs, a fantastic group of mentors: Drs. Stewart Prager, Clint Sprott, Paul Terry, John Sarff, Gennady Fiksel, Hantao Ji, Trudy Rempel, Adulgader Almagri, Daniel Den Hartog, and Miodrag Cekic. My fellow plasma graduate students provided a stimulating scientific and social atmosphere in which to pursue this research: Dr. David Newman, Dr. Christopher Watts, Dr. Earl Scime, Dr. Weimin Shen, Dr. Jeffrey Beckstead, Dr. Saeed Assadi, Dr. George Chartas, Brett Chapman, Gene Riggs, Jim Hollenberg, Neal Crocker, Carl Sovinec, Kevin Mirus, John Henry, Gordon Starr, Eduardo Fernandez, Paul Fontana, and Chuang Ren. The MST technical and engineering staff provided invaluable assistance: Tom Lovell, Mark Thomas, Roch Kendrick, John Laufenberg, Jerry Frank, Larry Smith, Paul Quicker, and Todd Kile. I thank Kay Shatrawka for her assistance.

I thank my parents, Randall Stoneking and Jeanne Stoneking for their love and support. My in-laws, Mary and Dick Smythe, have had a big impact on my life and I acknowledge their love and support also. Most importantly I acknowledge Laura Smythe, my wife and life partner. This work results from her constant reassurance and love as much as anything else.

This work has been supported by the U. S. Department of Energy and the U. S. Department of Education.

## Table of Contents

# 1. Introduction

## *1.1 Overview of the RFP*

Aside from its attractiveness as a possible configuration for achieving controlled nuclear fusion, the reversed field pinch (RFP) plasma provides an excellent environment in which to study turbulent plasma physics. In few other laboratory physical system are the laws of classical physics given such free rein. $10^{20}$ electrons and protons are liberated from their hydrogenic prisons and supplied with 500 kiloJoules of energy. The result is a system exhibiting global self-organization in the presence of robust micro-scale turbulence.

The reversed field pinch (Bodin, 1980) along with the tokamak and the stellarator belong to the toroidal class of fusion plasma experiments. However, unlike the tokamak where the equilibrium toroidal magnetic field is determined by currents in the external TF (toroidal field) coils and the stellarator where the entire equilibrium field (toroidal and poloidal) is fixed by the external circuit, the fields of the RFP are in large part determined by currents inside the plasma. The currents and the fields of the RFP are allowed to evolve via a turbulent reconnection of magnetic field lines to a nearly force-free state, a state in which the current is everywhere (nearly) parallel to the magnetic field (Taylor, 1974). Plasma relaxation and the subsequent persistence of the RFP configuration require a dynamo mechanism. Such force-free magnetic configurations and associated dynamo behavior are also observed in astrophysical plasma, e.g. solar flares, as well as other laboratory plasma experiments, e.g. the spheromak (Taylor, 1986). The nature of the RFP dynamo mechanism is a subject of

ongoing research and a contribution toward its understanding is attempted in this work.

*1.2 Observation of fast electrons in the RFP*

While fundamental plasma particle dynamics are described satisfactorily by the equations of Newton and Maxwell, the essentially infinite number of degrees of freedom associated with a laboratory plasma prohibits understanding and predicting its behavior in terms of these equations. Some simplifying assumptions must be made in order to describe plasma behavior. The magnetohydrodynamic (MHD) model is one such simplification, which treats the plasma as a conducting fluid. MHD theory is successful in predicting the equilibrium and in many cases the stability and dynamics of laboratory plasma. A MHD theory for the RFP dynamo (Schnack, 1985) is in broad agreement with experiments, despite the observation that the conducting fluid approximation is quite blatanty violated. A fluid description requires that the plasma be sufficiently collisional so that the velocity distribution for each particle species may be described by the Maxwell-Boltzmann distribution, i.e. each species has a well-defined temperature and pressure. Measurements show that this is not the case for the electrons in many RFP devices. The velocity distribution of electrons in the core and at the edge exhibit an unambiguous non-Maxwellian tail (Ingraham, 1990; Ellis, 1990; Hokin 1992; Chartas, 1991; Antoni 1992; Yagi, 1990). The electrons which make up this tail are referred to variously as "fast," "hot," "superthermal ," or "energetic." In this work, I will refer to the tail of the electron distribution as "fast." A review of fast electron observations and theories in the

RFP was provided by Ortolani (Ortolani, 1992). It has been proposed that the fast electrons in the edge of the RFP plasma are accelerated in the core by the applied electric field and then transported to the edge collisionlessly along stochastic magnetic field lines (Jacobson, 1984). The questions of the generation mechanism and the importance of the fast electron population as a dynamo current carrying population are taken up in chapter 3.

*1.3 Turbulent fluctuation driven transport*

Theoretical models which propose to explain the dynamo rely on the presence of certain instabilities in the RFP, and on their nonlinear interaction. These are the "tearing" modes (Furth, 1963), and their presence and nonlinear coupling is supported by measurements in MST (Assadi, 1992). Given the nonlinear nature of the equations governing plasma behavior it is not surprising that the energy in the large scale tearing fluctuations finds its way to smaller scales by way of a cascade, and that the resulting plasma is robustly turbulent, exhibiting broadband fluctuations in all local plasma quantities. Turbulent fluctuations are undesirable from the standpoint of achieving controlled nuclear fusion because they are known to assist the transport of particles and energy out of the device. This work contributes to the understanding of turbulent plasma transport by presenting measurements of electron particle transport due to magnetic fluctuations (chapter 4).

*1.4 Theses*

The organization of this work is as follows: Chapter 2 discusses the details of the experimental apparatus used to collect the data presented in chapters 3 and 4. In chapter 3, measurements of the equilibrium fast electron distribution are presented and discussed, and conclusions are drawn regarding the RFP dynamo. Measurements of magnetic fluctuation induced transport are presented in chapter 4, and a discussion of the consequences for RFP confinement is presented. Chapter 5 gives a summary of the results presented and the conclusions

The two major theses presented in this work and supported by the accompanying measurements are the following: 1) Measurements of the fast electron distribution at the edge of MST do *not* support the existence of kinetic dynamo as the dominant mechanism for maintenance of the RFP configuration. Rather the data tends to support the fluid dynamo theory picture for the generation of poloidal current in the RFP. 2) Magnetic fluctuation induced particle transport is large enough to account for all observed particle losses inside r/a~0.85. The measurements support the common assumption that magnetic fluctuations dominate the transport in the RFP, although the magnitude of the diffusion coefficient (and thermal diffusivity) are likely influenced by the presence of a radial ambipolar electric field. The convective energy flux carried by the transported particles can explain all observed energy transport in MST.

## References

V. Antoni, M. Bagaton, D. Desideri, and N. Pomaro, "Energy flux investigation in the outer region of the Eta Beta II experiment," Plasma Phys. and Contr. Fusion, **34**, 699 (1992).

S. Assadi, S.C. Prager, and K.L. Sidikman, "Measurement of nonlinear mode coupling of tearing fluctuations," Phys. Rev. Lett. **69**, 281 (1992).

H.A.B. Bodin and A.A. Newton, "Reversed-field pinch research," Nucl. Fusion **20**, 1255 (1980).

G. Chartas, "Manifestations of the MHD and kinetic dynamo through soft x-rays," Ph.D. thesis, University of Wisconsin-Madison (1991).

R.F. Ellis, J.C. Ingraham, P.G. Noonan, and H.W. Tsui, "Fast electrons in the edge region of reversed and non-reversed discharges in HBTX-1C," Maryland Plasma Physics Paper Number 91-060.

H.P. Furth, J. Killeen, and M.N. Rosenbluth, "Finite-resistivity instabilities of a sheet pinch," Phys. Fluids **6**, 459 (1963).

S.A. Hokin, A. Almagri, S. Assadi, M. Cekic, B. Chapman, G. Chartas, N. Crocker, M. Cudzinovic, D.J. Den Hartog, R. Dexter, G. Fiksel, R. Fonck, J. Henry, D. Holly, S. Prager, T. Rempel, J. Sarff, E. Scime, W. Shen, J. Sprott, M. Stoneking, and C. Watts, "Anomalous ion heating and superthermal electrons in the MST reversed-field pinch," in *Proceedings of the 14th Int. Conf. on Plasma Physics and Controlled Nuclear Fusion*, Wurzburg (1992) page 539.

J.C. Ingraham, R.F. Ellis, J.N. Downing, C.P. Munson, P.G. Weber, and G.A. Wurden, "Energetic electron measurements in the edge of a reversed-field pinch," Phys. Fluids B **2**, 143 (1990).

A.R. Jacobson and R.W. Moses, "Sustainment dynamo reexamined: nonlocal electrical conductivity of a plasma in a stochastic magnetic field," Phys. Rev. Lett. **52**, 2041 (1984).

S. Ortolani, "The behaviour of fast electrons in reversed field pinches," in *Proceedings of the Int. Conf. on Plasma Physics*, Innsbruck, Austria (1992).

D.D. Schnack, E.J. Caramana, and R.A. Nebel, "Three-dimensional magnetohydrodynamic studies of the reversed-field pinch," Phys. Fluids **28**, 321 (1985).

J.B. Taylor, "Relaxation of toroidal plasma and generation of reverse magnetic fields," Phys. Rev. Lett. **33**, 1139 (1974).

J.B. Taylor, "Relaxation and magnetic reconnection in plasmas," Rev. Mod. Phys. **58**, 741 (1986).

Y. Yagi, T. Shimada, Y. Hirano, K. Hattori, Y. Maejima, I. Hirota, K. Saito, and S. Shiina, in *Proceedings of the 17th EPS Conf. on Controlled Fusion and Plasma Heating,* Amsterdam Vol. 14BII, 545 (1990).

# 2. Experimental Apparatus

## *2.1 Madison Symmetric Torus*

Experiments presented in this work were carried out on the Madison Symmetric Torus (MST) reversed field pinch (RFP) shown in Fig. 2.1. MST is a large toroidal device with circular poloidal cross-section, major radius $R$=1.5 m, minor radius $a$=0.52 m, and maximum plasma current $I_p$=750 kA. Details of the design and operation of MST can be found in the references (Dexter, 1991), as well as a summary of results during the first five years of operation (Hokin, 1993). Details of major diagnostic systems such as the Thomson scattering (TS) diagnostic for measuring central electron temperature and density (Den Hartog, 1994), the charge exchange analyzer (CXA) for measuring ion temperature (Scime, 1992), the magnetic coil arrays (Assadi, 1994), and the far infrared interferometer (FIR) for measuring electron density profiles (Burns, 1992) can be found in the references also. A summary of the unique features of MST that have significant impact on the theses of this work is provided in this section.

The design of MST was guided in large part by two goals: 1) to minimize magnetic field errors that have been shown to adversely affect confinement in other RFP devices, and 2) to provide good access for plasma diagnostics. Toward these ends the MST vacuum vessel (VCV) made from 5 cm thick aluminum was designed to function also as a single toroidally continuous toroidal field (TF) coil with negligible field ripple and as a close-fitting conducting shell to stabilize ideal MHD instabilities. The VCV is penetrated by

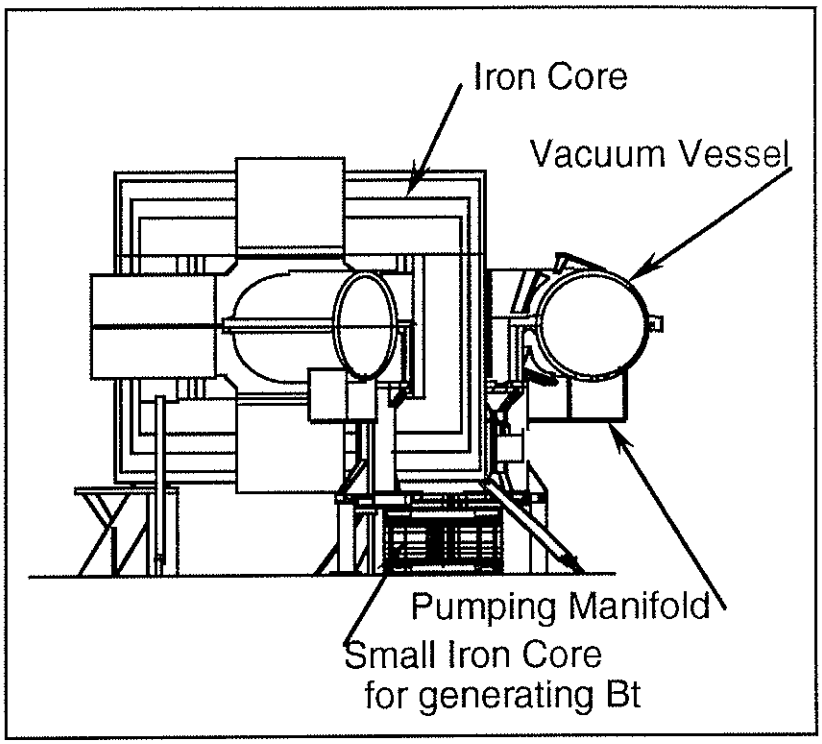


*Fig. 2.1 The Madison Symmetric Torus viewed from the south. The vacuum vessel has been cutaway to show the pumping manifold and the poloidal cross-section.*

193 small (5 cm diam.) holes in the bottom through which it is evacuated, 175 small (5 cm diam.) diagnostic access ports, and 4 larger (11.4 cm diam) ports. This design allows ample diagnostic access unimpeded by the presence of toroidal field coils, but maintains low field errors by elimination of large ports in the conducting shell. The VCV has two insulated gaps to allow toroidal and poloidal flux to enter from the external circuit and it is at the vertical or poloidal gap where concern about field errors is greatest and where the greatest effort has gone into measuring and reducing field errors (Almagri, 1992; Almagri, 1990; Dexter, 1991).

It was important for this work that plasma confinement not be dominated by machine specific field error effects. Discharge conditions have been observed in MST where rotating magnetic fluctuations phase lock to the poloidal gap field error, cease rotation, grow to large amplitude, and cause premature discharge termination. Passive field error correction at the poloidal gap has been successful in eliminating or at least delaying the onset of mode locking until late in the discharge (Almagri, 1992). Data discussed in this work is taken predominately from the early portion of the discharge at and just after peak plasma current when field error affects are minimal and plasma transport is governed by intrinsic RFP plasma dynamics.

## *2.2 Electron Energy Analyzer*

### 2.2.1. Analyzer Design

The desire to recover information about the electron distribution, fluctuations in that distribution and correlations of those fluctuations with magnetic fluctuations motivated the design of two electron energy analyzer (EEA) probes. These probes are more sophisticated versions of the EEA used to measure fast electrons in ZT-40M (Ingraham, 1990) and HBTX-1C (Ellis, 1990). The two-channel EEA samples electrons flowing in both directions along the equilibrium magnetic field. It also incorporates a magnetic coil triplet in order to make correlation measurements locally between $\tilde{J}_{\parallel}$ and $\tilde{B}$. The three-channel EEA samples electron current from one direction only, but can resolve the (effective) temperature in time and the high frequency $k$-spectrum of the electron current fluctuations.

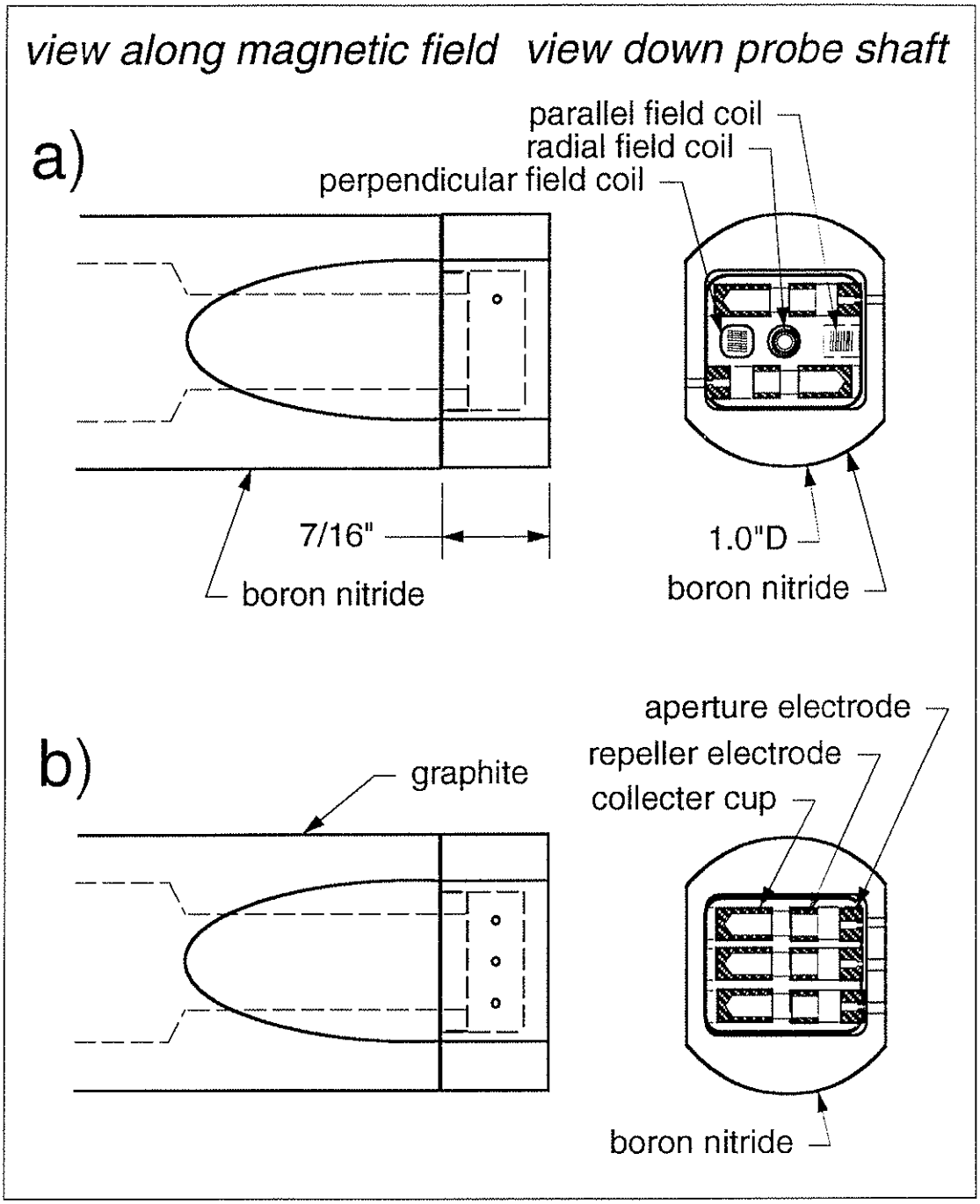


*Fig. 2.2 a) Schematic drawing of the two-channel electron energy analyzer (EEA) incorporating a magnetic coil triplet. b) schematic of the three-channel EEA.*

Diagnosing the edge of a hot magnetized plasma requires the use of robust instruments of simple design in order to survive and deliver clean data in an environment of high heat flux and numerous sources of possible signal contamination. Fig. 2.2 shows schematic drawings of the two EEA probes. Both probes are enclosed in a boron nitride (BN) shroud that serves as a particle and heat shield. BN is a readily machinable and electrically insulating material with low thermal expansion and hence excellent thermal shock resistance. The shroud has 1/32" diameter apertures to allow electrons to enter the analyzer. The apertures are small enough to significantly attenuate ion *and* to a lesser extent, electron flux into the analyzer. The probe shaft of the two channel EEA is also made of BN, while that of the three channel EEA was graphite. Graphite was chosen for the three channel EEA shaft in order to alleviate heat accumulation problems encountered in the earlier two channel EEA design, graphite having higher thermal conductivity than BN (not to mention considerably lower cost). The inside of both BN probe shrouds is painted with a thin coat of silver paint and contact established with MST machine ground potential. The silver paint provides shielding of electrostatic noise, but allows electromagnetic fields to penetrate to well above 1 MHz. Note that the electrostatic shielding is not complete as there are holes in the shield through which electrons enter the probe. The EEA electrodes (and the BN coil forms in the case of the two channel EEA) are housed in a BN cartridge machined to accommodate the electrodes (and coil forms) and provide access for hookup wires that are spot welded to the electrodes and fed through the probe shaft. Hookup wires are coaxial Kapton® insulated wires from MDC Inc. The outer conductor of each lead is grounded to the probe feed shaft back at

the vacuum feedthrough. The probe shaft was grounded to the MST vacuum vessel for all experiments. Magnetic coil leads are tightly twisted and fed through a grounded braid to avoid cross-talk with high-voltage and collecter current leads.

A single EEA channel consists of three cylindrical electrodes: the aperture, the repeller, and the collecter in the order encountered by an incoming electron. Aperture and repeller electrodes are constructed of molybdenum, a metal with a high melting temperature (2617°C) and thus suitable for use in the high heat flux environment at the edge of the MST plasma. The collecter electrodes were fabricated of stainless steel, for no significant reason other than cost and availability.

The standard EEA entrance aperture is .0135" in diameter (#80 drill) and .030" in length widening out to approximately a .1" diameter cylindrical channel after the limiting aperture. The purpose of the aperture electrode is to eliminate ions. The axis of the EEA channel is aligned with the local magnetic field at the edge of MST. Since the typical electron gyro-orbit radius is .3 mm (.01"), a small fraction of the electron current travelling along the field line successfully passes the aperture. The typical ion gyro-orbit is 1 cm so no significant ion current enters the analyzer. More will be said about aperture transparency to both ions and electrons in section 2.2.4. The aperture electrodes were maintained at machine ground potential during all experiments presented in this work.

The repeller electrode serves two purposes: to select the minimum electron energy needed to reach the collecter, and to suppress the loss of secondary electrons produced at the collecter by electron impact. The repeller

bias voltage was varied from -50 V to -700 V (with respect to machine ground potential) to obtain information about the fast electron distribution function. Fig. 2.3a shows the electric potential contours in a single channel of the EEA, for a typical electrode bias configuration. Laplace's equation was solved in cylindrical geometry using the *simultaneous overrelaxation algorithm (SOR)* (Press, 1986). Fig. 2.3b shows the potential on axis, the minimum being the effective repeller potential. Results for a number of bias configurations confirm that the effective repeller potential is 3.3% less than the voltage applied to the repeller electrode. For all data presented in this thesis the repeller potential was at least 50 V more negative than the collecter. This is sufficient to suppress the loss of secondary electrons produced at the collecter, because the energy distribution of secondary electrons emitted from a surface is nearly independent of the incident particle energy and lies almost entirely below 50 eV (Rudberg, 1936). The acceptance angle of the aperture (11°) does not allow an incoming electron to strike the repeller electrode. Secondary electrons are therefore not produced at the repeller electrode.

Electrons that successfully negotiate the aperture and the repelling potential are collected and "counted" by measuring the electric current drawn by the collecter cup. The current (~1 mA) was shunted across a 50 Ω resistor to machine ground. The voltage across the resistor was amplified by a Tektronix AM502 differential amplifier, filtered with an RC filter at 100 kHz, added to a +4 V d.c. offset and the output was sent to a unity gain isolation amplifier before being digitally sampled at 500 ksamples/sec. Fig. 2.4 shows the effective circuit used to measure the electron current collected by the EEA. The measured capacitance to ground of the collecter cup and hookup wires is about 150 pF.

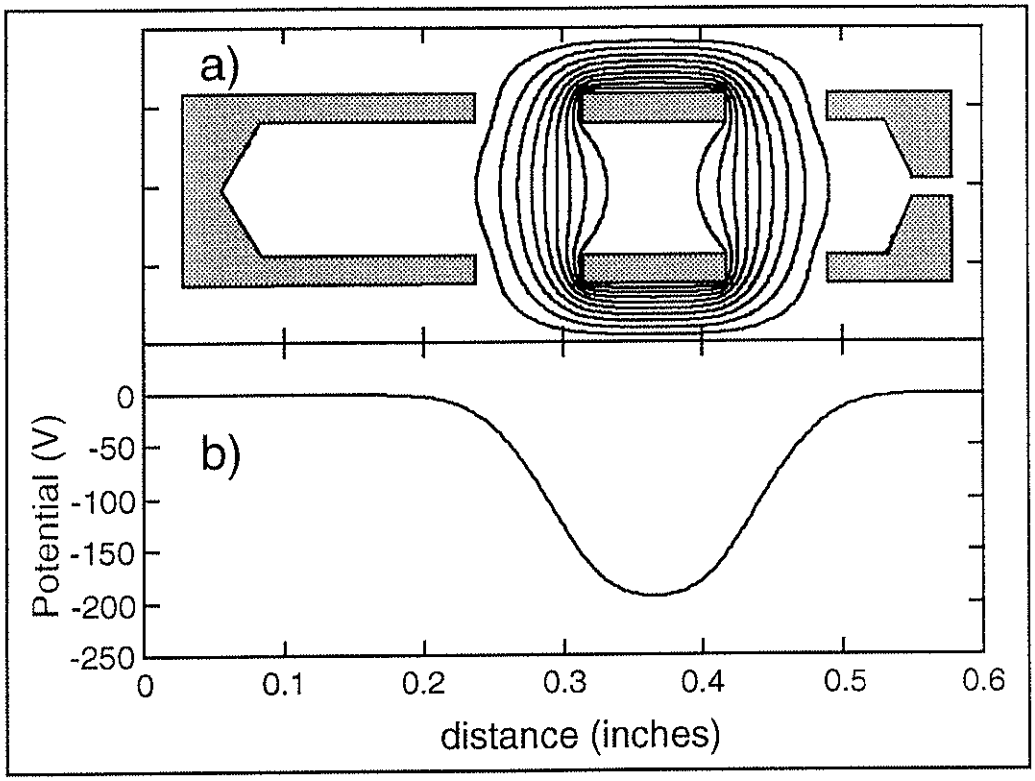


*Fig. 2.3 a) Solution to Laplace's equation for EEA electrode bias configuration with collecter and aperture at ground and repeller at -200 V. Contours are spaced at 20V. b) The potential along the axis of the EEA has a minimum of -193 V.*

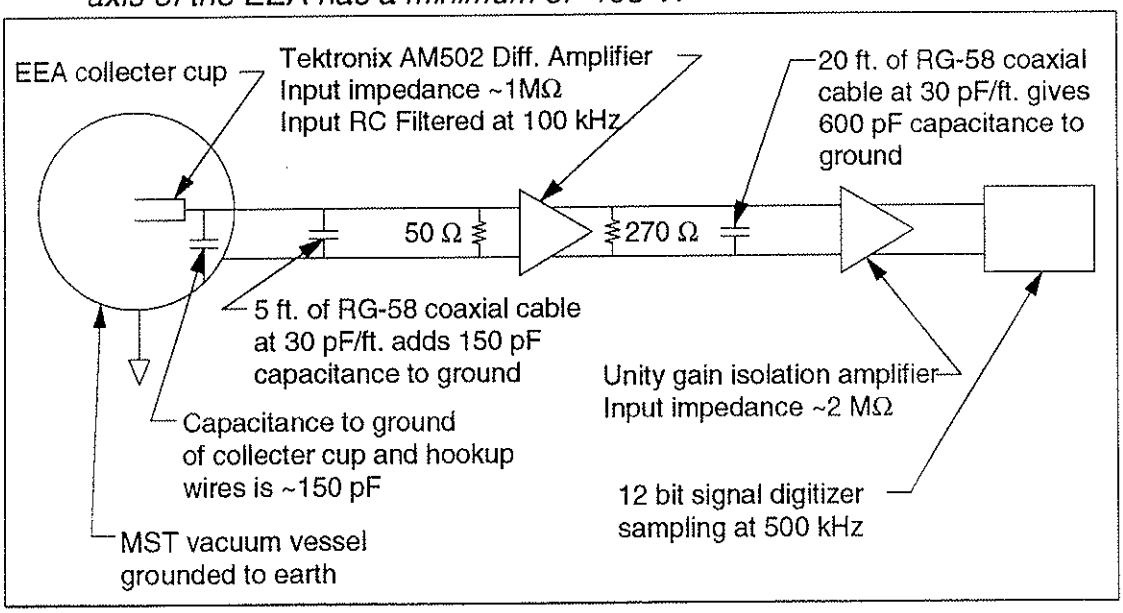


*Fig. 2.4 Schematic of the effective circuit used to collect EEA data.*

Five feet of RG-58 coaxial cable carried the signal from the probe to the amplifier, adding 150 pF more capacitance to ground. Therefore, the frequency response to electron current fluctuations when measured across 50 Ω is good out to 10 MHz. The signal is then filtered at 100 kHz to prevent aliasing when the signal is digitally sampled at 500 kHz. A 270 Ω resistor on the output of the amplifier prevents cutoff of the signal transmitted across 20 feet of coaxial cable (cutoff is at ~1 MHz).

The magnetic pickup coils are wound with about 100 turns of 38 gauge magnet wire on BN coil forms of diameter .063". The leads are tightly twisted and fed through a grounded braid to the vacuum feedthrough. The signals were amplified and filtered with an A.C. coupled differential amplifier (see Banville, 1990), that provided a flat gain in the frequency band 2 kHz to 200 kHz, and also digitally sampled at 500 kHz.

### 2.2.2 EEA Signal Interpretation

The EEA measures electric current carried by some fraction of the electron distribution. The shaded region of Fig. 2.5 shows the region of the electron distribution in velocity space that is collected by the collecter cup. Contours of the electron velocity distribution are shown in the plane $(v_{\parallel}, v_{\perp})$, velocity parallel and perpendicular to the local magnetic field respectively. The repeller voltage provides a minimum parallel electron velocity. The finite aperture size (for the BN particle shroud and aperture electrode) cuts off electrons with large perpendicular velocity (large gyro-orbits). The perpendicular velocity cut-off is not as abrupt as it appears in Fig. 2.5. Whether an electron enters the analyzer depends not only on its perpendicular velocity

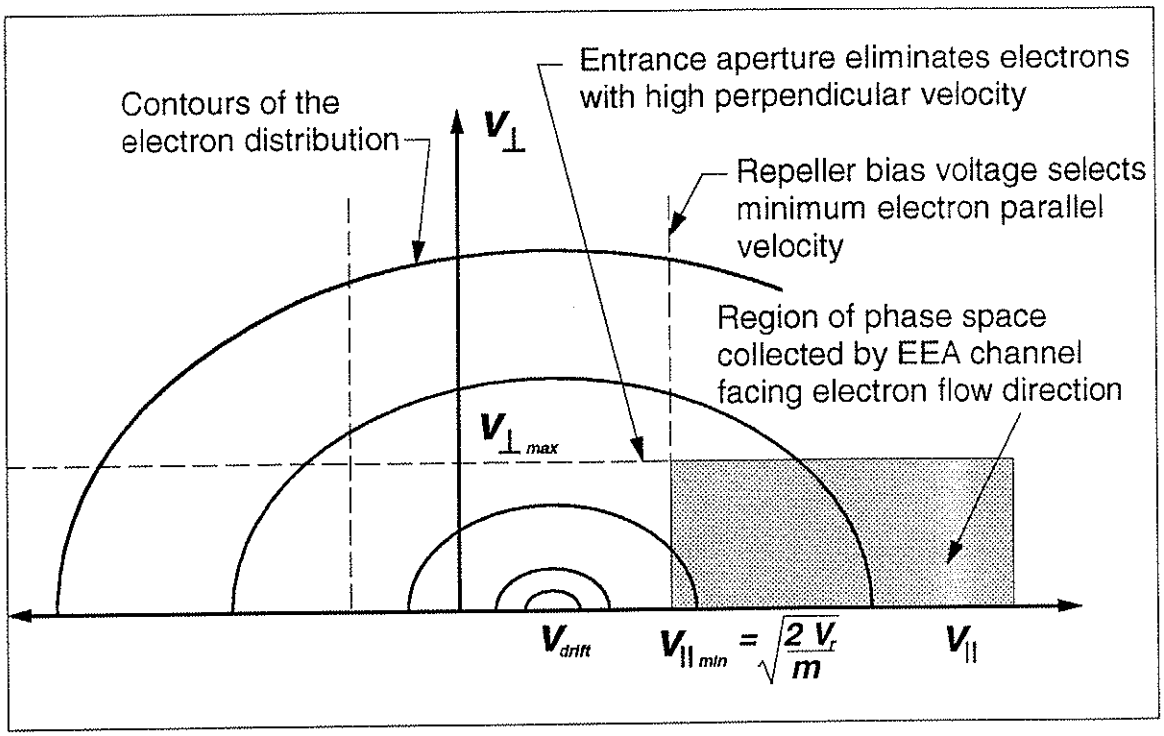


*Fig. 2.5 The region of velocity space collected by the EEA*

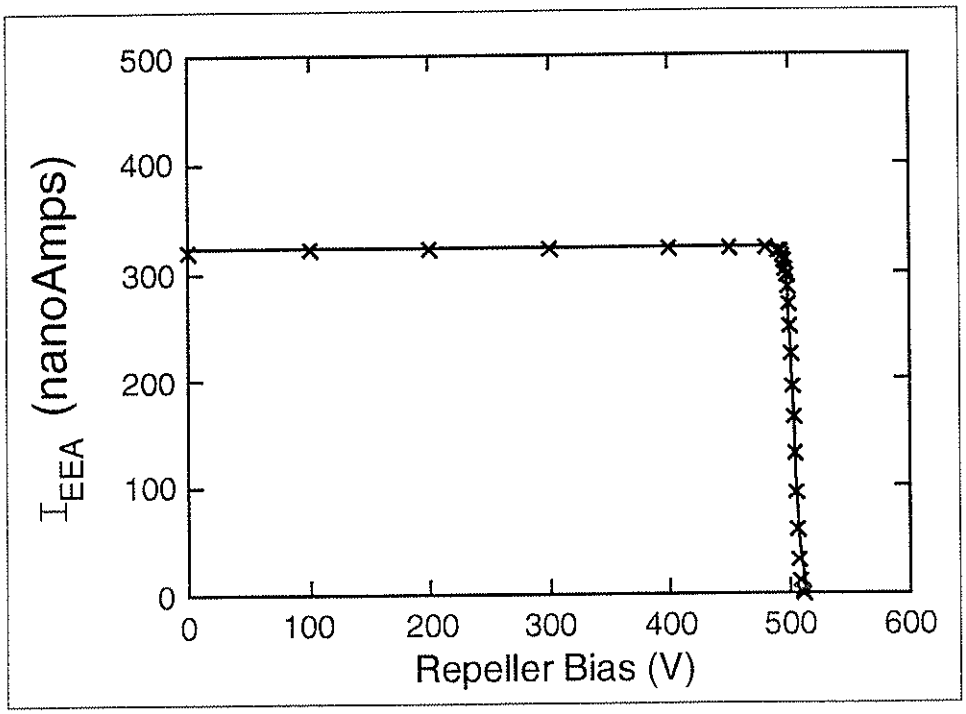


*Fig. 2.6 The EEA collecter current versus repeller bias for a 500 V electron beam. The signal is fit to the expected signal for T=0.1 eV and beam energy (i.e. drift energy) 505 eV.*

(and to a lesser extent its parallel velocity), but also the phase of its gyro-orbit and the location of its guiding center relative to the analyzer channel axis. A general description of the current collected by the collecter cup as a function of the electron distribution, the repeller voltage and the probe geometry is given by

$$I(V_r) = e\int_{v_{\parallel min}}^{\infty} v_{\parallel} dv_{\parallel} \int_0^{\infty} 2\pi v_{\perp} dv_{\perp} \int_0^{\infty} 2\pi\rho\, d\rho W\left(\rho, v_{\parallel}, v_{\perp}\right) f_e\left(v_{\parallel}, v_{\perp}\right). \qquad (2.1)$$

$V_r$ is the repeller voltage, e is the electron charge, $v_{\parallel min} = \sqrt{2V_r/m_e}$ is the minimum parallel electron velocity necessary to pass the repeller, ρ is the distance from the electron's guiding center to the axis of the analyzer channel, $W$ is a "weighting" function that contains the aperture geometry information and determines whether an electron from a region of phase space is able to pass through the aperture, and $f_e$ is the electron velocity distribution function. The electron distribution is assumed to be spatially uniform near the EEA. Ideally, the repeller voltage is referenced to the plasma potential. Practically, however, it is referenced to machine ground potential. A nonzero d.c. plasma potential adds a d.c. offset to the repeller potential, and fluctuations in the plasma potential can cause fluctuations in the collecter current which are not representative of fluctuations in the electron distribution. I will return to this point later in order to quantify its effect. For now I assume the plasma potential and machine ground potential are identical. Near to edge of MST this is a good approximation in the equilibrium sense: $\langle \phi_p \rangle \approx 0$.

Often the velocity distribution function for a plasma species can be approximated by a Maxwellian distribution. A Maxwellian distribution is

parametrized in terms of four quantities: the density $n$, the parallel temperature $T_{//}$, the perpendicular temperature $T_{\perp}$, and the parallel drift velocity $v_d$:

$$f_{maxwell} = n\frac{m}{2\pi T_{\perp}}\sqrt{\frac{m}{2\pi T_{\parallel}}}\exp\left\{-\frac{m}{2T_{\parallel}}\left(v_{\parallel}-v_d\right)^2-\frac{mv_{\perp}^{\ 2}}{2T_{\perp}}\right\}. \tag{2.2}$$

The form of Eq. 2.2 assumes the electron current is toward the EEA. If the EEA channel is facing away from the net electron drift direction, the sign of $v_d$ is reversed in Eq. 2.2. It will be verified *post facto* that the weighting function $W$, depends more strongly on the perpendicular distribution than the parallel distribution of electrons. Assume the weighting function is independent of parallel temperature. Then with the assumption of a Maxwellian distribution, the equation for the collected electron current (Eq. 2.1) separates into two multiplicative factors, one that depends on the perpendicular temperature, and one that depends on the parallel temperature and drift. The integral over the perpendicular distribution and weighting function is absorbed into a quantity $\eta$, the aperture transparency. Eq. 2.1 becomes

$$I_{\pm}(V_r) = \eta Ane\sqrt{\frac{m}{2\pi T_{\parallel}}}\int_{v_{\parallel min}}^{\infty} v_{\parallel}\exp\left\{-\frac{m}{2T_{\parallel}}\left(v_{\parallel}\mp v_d\right)^2\right\}dv_{\parallel}, \tag{2.3}$$

where A is the aperture area. The + subscript indicates that the EEA channel faces the electron drift direction and the - subscript applies when the EEA faces the "backflow" direction. The integral can be performed analytically and becomes

$$I_{\pm}(V_r) = \eta Ane\left\{\sqrt{\frac{T_{\parallel}}{2\pi m}}\exp\left\{-\frac{\left(\sqrt{V_r} \mp \sqrt{E_d}\right)^2}{T_{\parallel}}\right\} \pm \sqrt{\frac{E_d}{2m}}\,\mathrm{erfc}\left\{\frac{\sqrt{V_r} \mp \sqrt{E_d}}{\sqrt{T_{\parallel}}}\right\}\right\}, \qquad (2.4)$$

where $v_{\parallel min} = \sqrt{2V_r/m}$ has been used and the "drift energy," $E_d = \frac{1}{2}mv_d^2$ is the energy associated with an electron moving at the drift velocity. For a vanishing drift velocity, Eq. 2.4 becomes a simple exponential with argument $-V_r/T_{//}$ as expected.

The current density carried by the electron distribution is

$$J_{\parallel e} = \frac{I_+(0) - I_-(0)}{\eta A} = nev_d. \qquad (2.5)$$

As seen from Eq. 2.4, the dependence of the collected current on the repeller voltage completely determines the electron parallel temperature and drift. In practice, in order to obtain a satisfactory fit to the data it is necessary to fit Eq. 2.4 simultaneously to data from both the electron drift direction and the "backflow" direction. Such a fit requires three parameters: (1) $T_{//}$, (2) $E_d$, and (3) $\eta Ane$.

### 2.2.3 Electron Beam Test of the EEA

An electron beam was installed on a vacuum chamber in order to demonstrate that the current collected by the EEA as a function of the repeller voltage behaves as predicted by Eq. 2.4. The beam was directed into the EEA aperture in vacuum. The current collected was then measured as a function of the repeller bias voltage. The results of this test are shown in Fig. 2.6 for a 500

eV beam. The data is fit to the function predicted by Eq. 2.4 and the resulting drift energy, i.e. beam energy, is 505 eV and the temperature is 0.1 eV. This test was performed for a variety of electron beam energies and the results were similar to Fig. 2.6. The electron beam test could not be used to calibrate the EEA as such. The conditions of the e-beam test differed from the conditions in the plasma in two significant ways: (1) there is no magnetic field in the test situation and (2) the electron beam current was less than 1 μA compared to ~1 mA collecter currents in the plasma experiment. The presence of a magnetic field introduces the aperture transparency effects discussed below. The large collecter current experienced in the experiment introduces possible space charge effects. The e-beam test was successful in demonstrating the basic operation of the EEA and verifying the dependence of the collecter current on the applied repeller voltage.

### 2.2.4 Aperture Transparency

In this section, calculation of the aperture transparency is discussed. The transparency calculation was necessary to absolutely calibrate the EEA. As an approximation to the EEA aperture, consider the following idealized situation. A homogeneous Maxwellian electron distribution exists in the vicinity of a conducting wall extending in the x-y plane and maintained at the same potential as the plasma. The wall has thickness L, and a cylindrical aperture of radius $\rho_o$ penetrates it in the z-direction. The magnetic field is uniform and in the z-direction. A positive ion population exists only to preserve the charge neutrality of the plasma; the effectiveness of the aperture in excluding ions will be taken up later. There are no gradients and no sheath effects as the wall is

maintained at plasma potential. In defining the transparency it is useful to consider the limiting case of $L$=0: All electrons that are inside the aperture at the plane of the wall are passed. This is unit transparency for all moments of the distribution. The percent transparency for a moment of the distribution (particles, current or energy) is the amount of that moment transmitted divided by the amount that would have been transmitted in the $L$=0 case. For example, the transparency for current is defined as

$$\eta_{current} = \frac{I_{transmitted}}{\pi \rho_0^{\,2} J_+}, \tag{2.7}$$

where $J_+$ is the current density carried by electrons moving in the +z direction. Similar definitions can be made for particle and energy transmission coefficients. Note that the transparency is defined relative to the population of electrons moving toward the wall, i.e. the probe.

For $T_\perp = 0$ (or equivalently $B = \infty$) the gyro-radius is reduced to zero and the only effect of the aperture is to admit a beam of electrons, the density and velocity distribution of electrons in the beam being identical to those of the plasma electrons. This case is also unit transparency for all moments of the distribution. With finite perpendicular temperature, the helical trajectory of an electron in the "potential" beam may carry it into the wall, and likewise, an electron which has a guiding center outside the "potential" beam may be carried through the aperture.

Consider a final limiting case: $L \rightarrow \infty$, an infinite cylinder aperture. In this case the symmetry dictates that the transparency be independent of the parallel distribution (i.e. $T_{||}$, $v_d$) as was the case for $L$=0 and $T_\perp = 0$. An electron can

pass this aperture only if its entire gyro-orbit lies inside the projection of the aperture. An electron with its guiding center a distance ρ from the axis of the aperture must have a Larmor radius less than $\rho_o - \rho$. Also, no electron will pass with Larmor radius larger than the aperture radius. The aperture transparency to current is then from Eqs.2.1-2.3 and 2.7

$$\eta_{current}(T_\perp) = \frac{m}{A2\pi T_\perp}\int_0^{\rho_o\omega_c} 2\pi v_\perp \exp\left\{-\frac{mv_\perp^{\,2}}{2T_\perp}\right\}dv_\perp \int_0^{\rho_o - \frac{v_\perp}{\omega_c}} 2\pi\rho\, d\rho, \qquad (2.8)$$

where $A$ is the aperture area, $\pi\rho_o^2$ and $\omega_c = eB/m$ is the electron cyclotron frequency. The *particle* transparency is also given by Eq. 2.8 in the infinite cylinder case, because the aperture is insensitive to the parallel distribution and the integrals over $v_{//}$ cancel in Eq. 2.7. The integrals in Eq. 2.8 can be performed and written as

$$\eta_{current}(T_\perp) = 1 - \alpha\left(e^{-1/\alpha} - 1\right) - \sqrt{\alpha\pi}\,\mathrm{erf}\left(1/\sqrt{\alpha}\right), \qquad (2.9)$$

where the dimensionless parameter $\alpha = 2T_\perp / m(\rho_o\omega_c)^2$ and is equal to the perpendicular temperature divided by the energy associated with an electron with a Larmor radius equal to the aperture radius. Fig. 2.7 shows the infinite cylinder transparency as a function of the normalized perpendicular temperature, α. It exhibits the proper limiting behavior. The transparency is unity as $T_\perp$ goes to zero and the transparency goes to zero as $T_\perp \to \infty$. The transparency of an infinitely long aperture to ion current can be seen from Eq. 2.9. The species mass appears in the dimensionless parameter α. α is

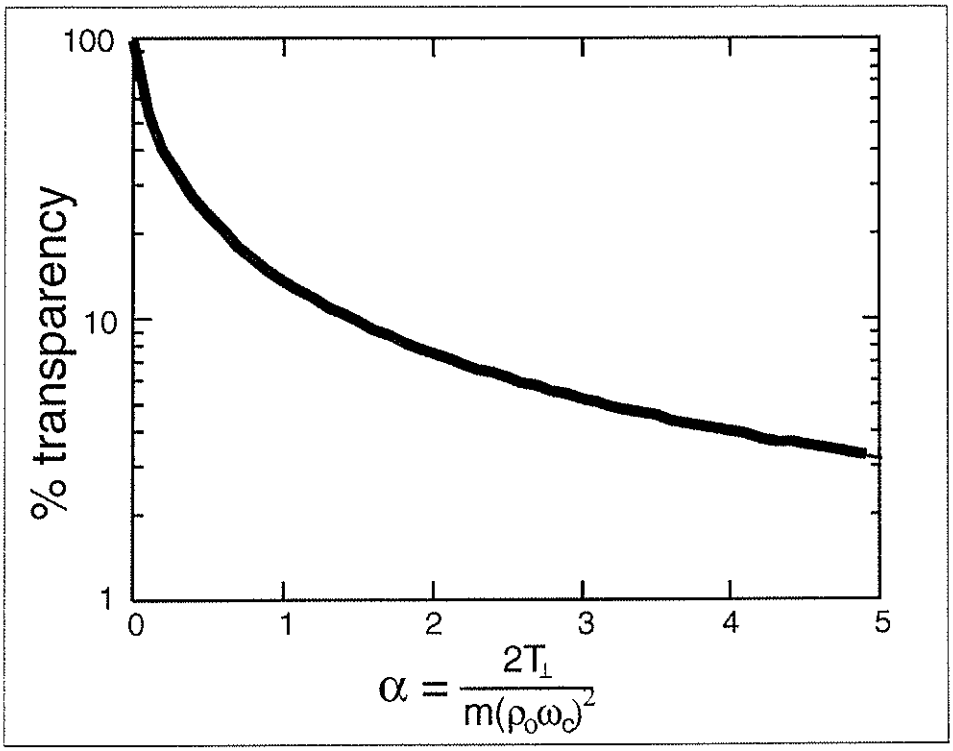


*Fig.2.7 The transparency of an infinitely long aperture to electron current as a function of perpendicular temperature*

proportional to mass since the cyclotron frequency is inversely proportional to species mass. For the same temperature, the transparency to ion current is about 1000 times smaller , i.e. the mass ratio, than for electron current. For example, an infinite cylinder with diameter .0135" in a 820 Gauss magnetic field is 12% transparent to a 20 eV electron population, but only ~.007% transparent to ions of the same temperature.

For a finite aperture length, *L*, the transparency is higher than Eq. 2.9 for all values of $T_\perp$. A closed form calculation of the transparency becomes unmanagable, because of the added dependence on the parallel distribution *and* the gyro-phase of the electron. This difficulty was surmounted by the

generation of a Monte Carlo code that calculated the transparency of an aperture to particles, current, and energy for a Maxwellian electron population in a magnetic field incident upon a particular aperture geometry.

The code randomly distributed (with uniform probability) the guiding centers of 10,000 electrons inside a 2D box at the center of which was the aperture. The box length was some multiple of the aperture radius (~7X). Fig. 2.8 shows the random distribution of guiding centers relative to the aperture for a typical Monte Carlo calculation (only 3500 are shown for aesthetic reasons). The electron velocities were distributed to approximate Maxwellian distributions with widths determined by $T_{||}$ and $T_{\perp}$, and the center of the parallel distribution was at $v_d$. Histograms of the parallel and perpendicular velocity distributions are shown in Fig. 2.9 for temperatures $T_{||}$ = 100 eV and $T_{\perp}$ = 50 eV along with the Maxwellian distribution that was being modelled. The gyro-phases of all the electrons were also randomized. Each particle was then examined to see if it successfully passed the aperture. The decision whether to pass a particle was broken down into four cases shown in Fig. 2.10: (1) the gyro-orbit lies completely outside the aperture, particle rejected, (2) the gyro-orbit lies entirely inside the aperture, particle accepted, (3) the gyro-orbit encloses the aperture, particle rejected, and (4) the gyro-orbit intersects the aperture. Case #4 requires that the particles gyro-phase and parallel velocity be analyzed to determine whether it passes through the aperture or not. The number of passed particles, as well as the current and energy they carried were added up and multiplied by the ratio of the box area to the aperture area to get the transparency for the three moments of the distribution.

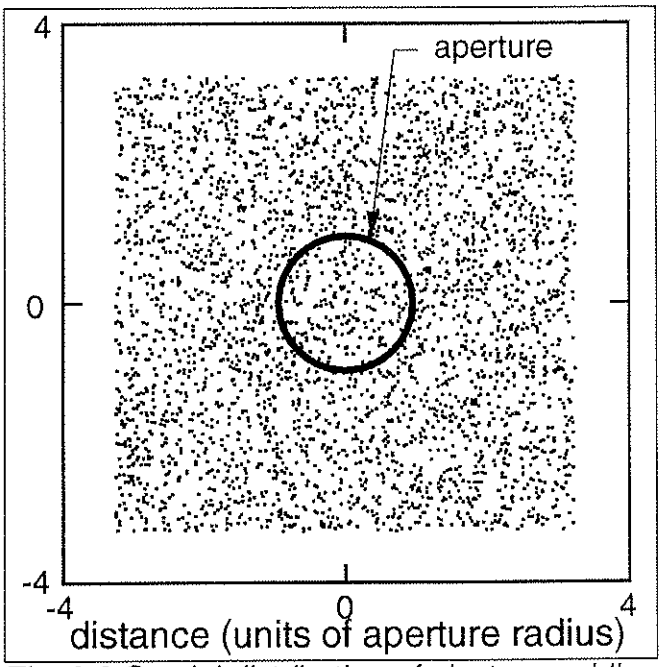


*Fig. 2.8 Spatial distribution of electron guiding centers relative to the EEA aperture for Monte Carlo calculation of aperture transparency.*

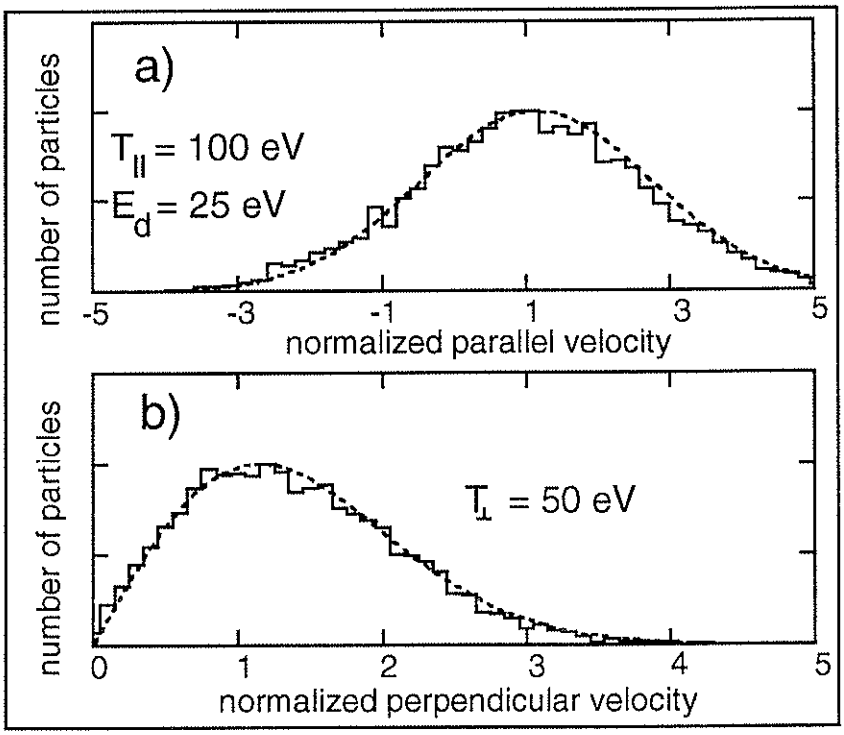


*Fig. 2.9 a) Monte Carlo parallel velocity distribution histogram for Maxwellian distribution with $T_{||}$ = 100 eV and $E_d$ = 25 eV and analytic function (dashed line). b) perpendicular distribution histogram for $T_{\perp}$ = 50 eV.*

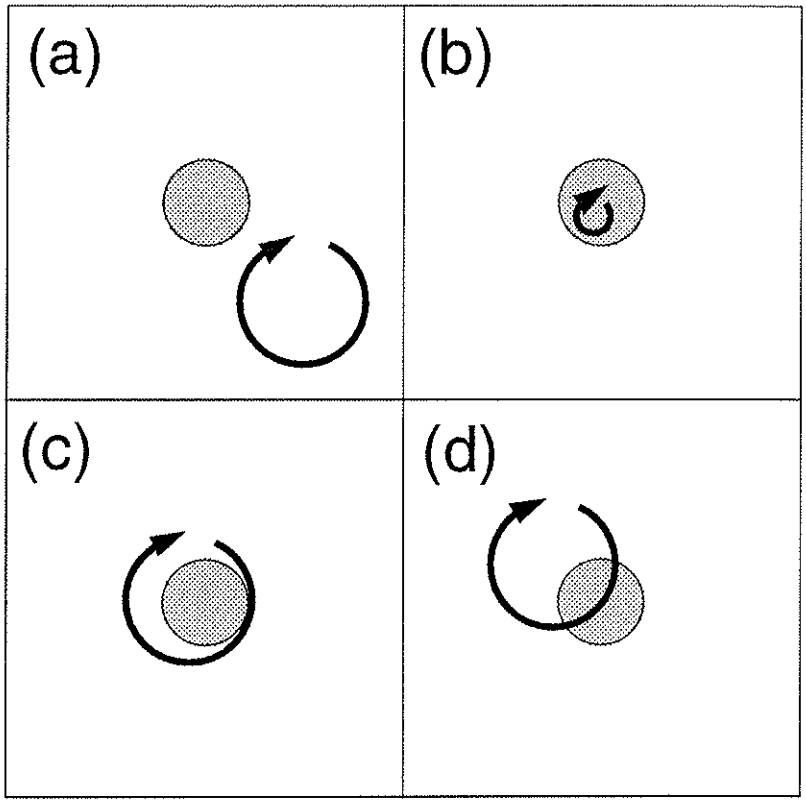


*Fig. 2.10 The four Larmor orbit geometries relative to the aperture: a) electron rejected, b) electrons accepted, c) electron rejected, and d) electron accepted or rejected depending on gyro-phase and parallel velocity.*

Fig. 2.11 shows the transparency of a .0135" diameter aperture in a 820 G magnetic field versus perpendicular temperature ($T_{||}$=100 eV) for several values of the aperture length, $L$: $L$=0, .5$\rho_o$, $\rho_o$, 2$\rho_o$, 3$\rho_o$, 5$\rho_o$, and 10$\rho_o$. The proper limiting behavior is exhibited, namely that the transparency is unity for all values of $T_\perp$ when $L$=0, and the analytic function for an infinite cylinder transparency (Eq. 2.9, the solid line in Fig. 2.11) is approached when the aperture length is many times its radius.

The dependence of the aperture transparency on the parallel temperature and the drift velocity is shown in Fig. 2.12. While the transparency

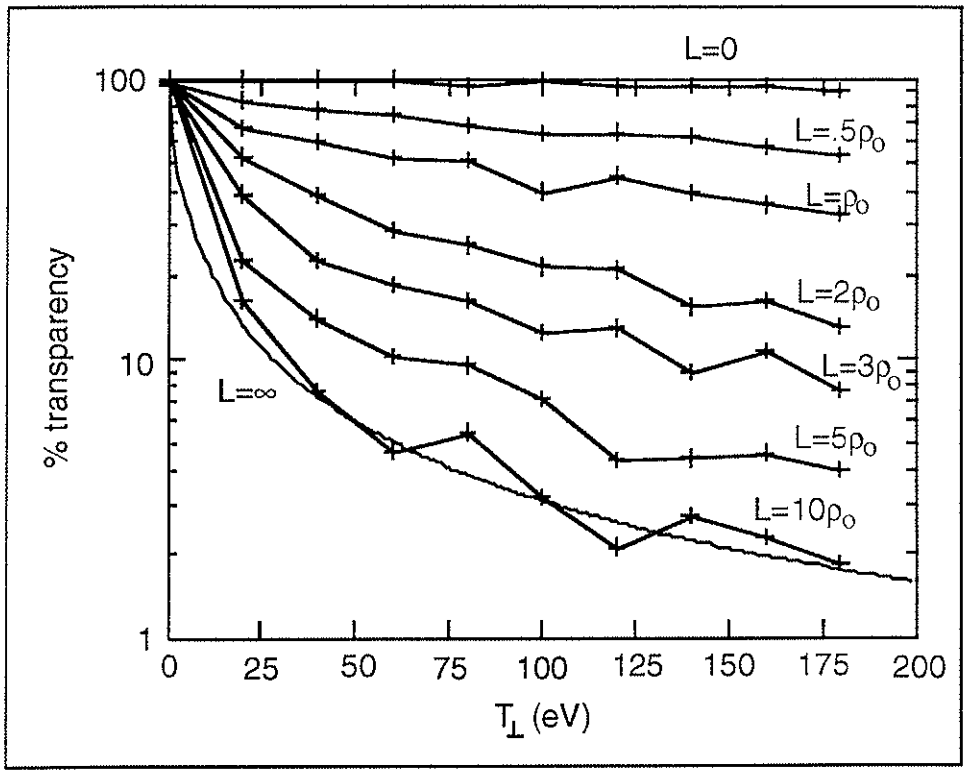


*Fig. 2.11 The results of Monte Carlo calculations of the EEA aperture transparency for a range of values for T and a range of aperture lengths. The solid line is the analytic result for an infinitely long aperture.*

depends on the parallel distribution parameters, the dependence is weaker than it is for the perpendicular temperature. This fact justifies the separation of the integral in Eqs. 2.1-2.3.

### 2.2.5 Possible Sources of Signal Contamination

There are a multitude of possible sources of signal contamination in the edge of a hot, turbulent, magnetized plasma. Fortunately the negligibility of many of them was established with a simple *in situ* test of the analyzer signal.

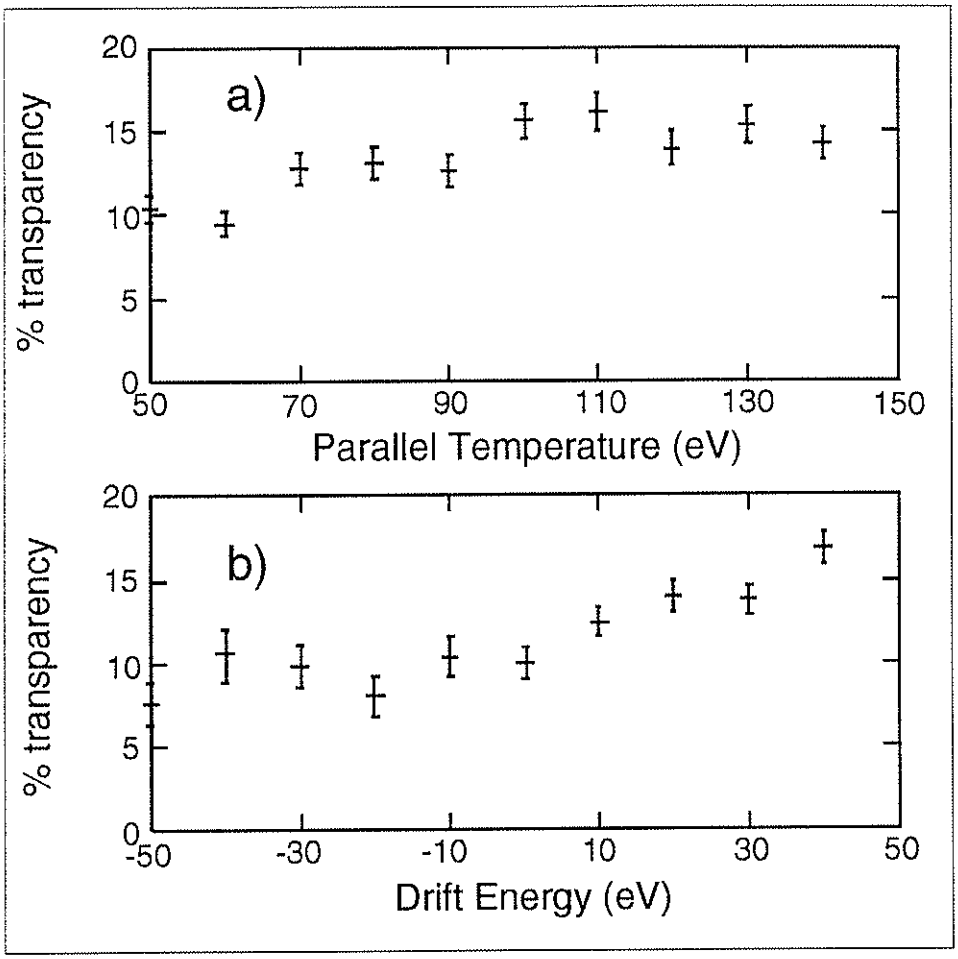


*Fig. 2.12 The EEA aperture transparency (Monte Carlo calculation) versus a) parallel temperature and b) drift energy.*

A typical raw EEA collecter current signal is shown in Fig. 2.13a, where the analyzer channel was aligned with the local magnetic field and faced the electron flow direction. The signal is unipolar and negative indicating either that the collecter cup is collecting electrons or emitting ions. The former is, of course, the case. Fig. 2.13b shows the raw signal on the same scale from the same analyzer channel where the channel was misaligned 15° relative to the local magnetic field. The unipolar and negative nature of the signal in Fig.

2.13a and the absence of signal above the small amount of noise in Fig. 2.13b established the negligibility of several possible sources of signal contamination: (1) There was no significant capacitive pickup of electrostatic fluctuations from the plasma. The signature of such an effect is an a.c. signal. In addition, rotating the probe 15° should not have eliminated such an effect. The silver paint electrostatic shield was therefore effective. (2) There was no significant photoelectric current from the collecter cup due to ultraviolet and soft x-ray radiation from the plasma. The negative collecter current demonstrates that the signal was dominated by electron collection, not emission. Also, when the probe was rotated 15° the photon flux entering the analyzer should not have changed significantly. The absence of signal in Fig. 2.13b supports the conclusion that photoelectric emission is not important. (3) The arguments against the existence of significant photoelectric emission can be applied to the issue of thermionic emission. The unipolar, negative nature of the collecter current and its absence when the probe was rotated 15° away from the field direction rule out the presence of significant thermionic emission from the collecter cup. (4) The absence of collecter current when the probe is faced misaligned with the magnetic field also quantifies the level of amplifier noise and stray pickup from the cables connecting the probe to the electronics (<50 mV).

In chapter 4 measurements of the correlation between magnetic fluctuations and electron current fluctuations are presented. A spurious electron current fluctuation could be caused by magnetic fluctuations that alter the local field direction significantly. However, the magnitude of the magnetic fluctuations in MST is about 2% of the equilibrium field. The fluctuation in the

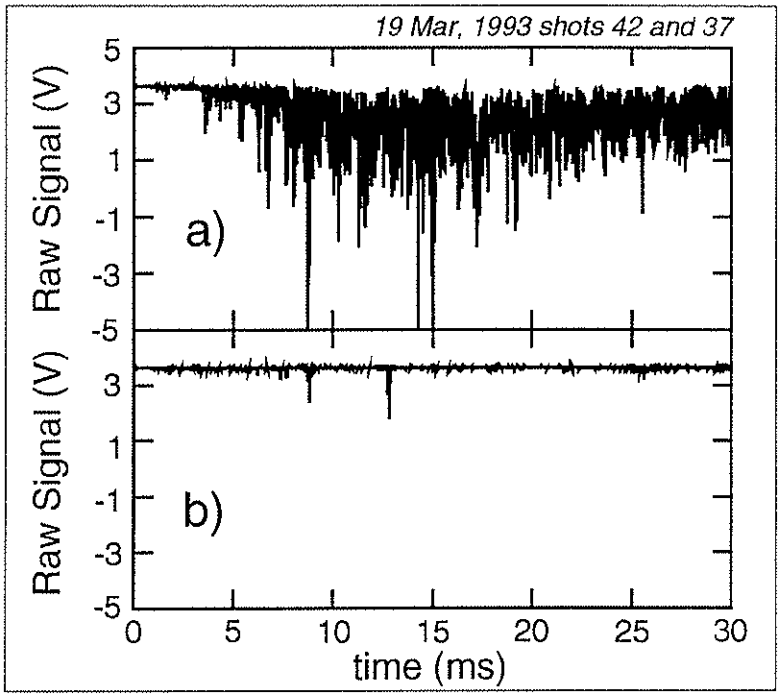


*Fig. 2.13 a) The raw EEA signal (with d.c. offset) aligned parallel to the local magnetic field. b) The raw EEA signal misaligned 15° from the magnetic field direction.*

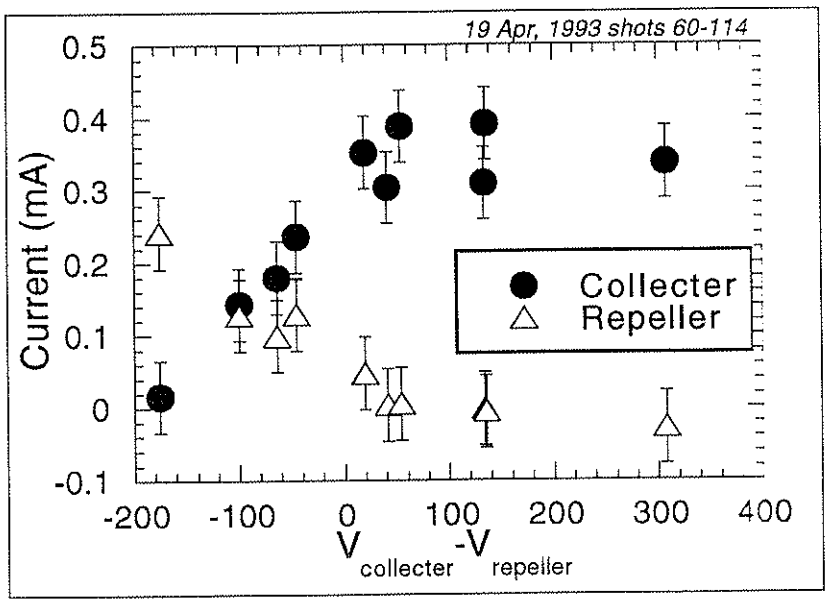


*Fig. 2.14 EEA collecter and repeller current (negative) collected for a range of voltage differences between the two electrodes. The characteristic is as expected for current dominated by incoming fast electrons.*

angle of the local field with respect to the EEA channel axis is therefore $\tilde{\theta} \approx \arctan(0.02) \approx 1.1°$. This fluctuation in the field direction is small compared to the EEA acceptance angle of 11°, so EEA signal fluctuations are not caused by changes in the local field direction moving the parallel current in and out of the instrument acceptance angle.

It is conceivable that some or all of the current collected by the EEA collecter cup was due to an internal discharge between the collecter and the repeller or aperture electrode. If there was an internal discharge it had to be initiated by ionization of neutral gas inside the analyzer channel by electron impact from plasma electrons entering through the aperture. Otherwise, there would be signal in Fig. 2.13b when the EEA was facing 15° off the local magnetic field direction.

In the two channel EEA design there was not a high conductance path for gas entering the aperture to flow up into the probe shaft. The pressure in the analyzer channel equilibrated with the neutral hydrogen pressure in the vacuum vessel on the time scale $\tau_{eq} = V/C$, where $V$ is the volume of the analyzer channel (~$4 \times 10^{-5}$ liters) and $C$ is the conductance of the gas through the aperture. In the molecular flow regime, the conductance of hydrogen gas through an aperture is (Moore, 1989) $C = 45D^3/L$ in liters per second when the diameter, $D$, and the length, $L$, are given in centimeters. The conductance for the EEA aperture is $C$= 0.02 L/s, and the pressure equilibration time is about 2 ms. Since the equilibration time is short compared to the gas puff prefill time (~20 ms), the pressure inside the two channel EEA tracks the pressure in the MST vacuum vessel. Modifications were made in the design of the three channel EEA so that gas had a high conductance path from the analyzer

channel in to the large volume of the probe shaft. The pressure equilibration time between the vacuum vessel and the (three channel EEA) probe shaft ($V$ ~ 0.2 liters) through the aperture was about 3 seconds. The probe shaft was therefore evacuated completely (to MST base pressure around $10^{-6}$ torr) between plasma discharges (MST cycle time was about 3 minutes), and served as a pump for the analyzer channel during the plasma discharge (~40 ms).

The next question was whether the neutral gas pressure inside the analyzer (~0.2 mtorr) was high enough to allow significant ionization events from electron impact. The cross-section for electron impact ionization of hydrogen peaks at about $10^{-16}$ cm$^2$ and at electron energies around 50 eV (Tate, 1932), right at the typical expected plasma electron energy. The worst case electron current generated by ionization of neutral hydrogen is

$$I_{ionization} < \sigma_{max} I_{electron} n_{H_2} L \qquad (2.10)$$

where $\sigma_{max}$ is the maximium ionization cross-section (~$10^{-16}$ cm$^2$), $I_{electron}$ is the incoming electron current (~1 mA), $n_{H2}$ is the neutral gas density (~$10^{13}$ cm$^{-3}$), and $L$ is the length of the interaction region (~1 cm). The direct current due to electron impact ionization is less than 1 μA, much smaller than the observed collecter currents.

A discharge could then be generated only if the liberated electrons subsequently ionized a number of atoms before striking an electrode. This requires a sufficient electric field strength and sufficient distance between electrodes to generate an avalanche. The mean free path for collisions with neutrals at the typical pressure of 0.2 mtorr, is $\lambda_{mfp} = 1/n\sigma \approx 10$ m, compared to

the ~1 cm electrode separation. It is very unlikely that the observed electron current collected by the EEA (Fig. 2.13a) was due to an inter-electrode discharge. The above argument can be summarized by the use of Paschen's law for breakdown of a gas (Druyvesteyn, 1940). Paschen's law is the general form of the breakdown voltage for a given gas as a function of the product of pressure and electrode gap distance. For hydrogen the breakdown voltage has a minimum of ~300 V at pd = 1 torr-cm. For the EEA conditions pd ~ $10^{-4}$ torr-cm, where the breakdown voltage is many kV, compared to the maximum electrode potential difference of 600 V.

Fig. 2.14 shows the electron current (negative current) collected by the the EEA collecter cup and the repeller electrode in the plasma for a range of potential differences between the electrodes. First note that when the collecter potential was more than 50 V more positive than the repeller the collecter current saturated and the repeller collected no current. If there were a discharge contributing significantly to the collecter current, the repeller should have detected ion current. As the collecter potential was made more negative than the repeller, electron current was diverted to the repeller electrode. The cross-over in the currents collected by the two electrodes happened when the collecter was about 100 V more negative than the repeller, consistent with the observed parallel temperature of the incoming fast electrons ($T_{||}$ = 100 eV) discussed in the next chapter.

Having established that the typically observed EEA collecter current is not due to an internal discharge, there are circumstances where inter-electrode arcing is observed. Fig. 2.15 shows an example of such a case. Such arcing was only observed in the two channel EEA (with low gas conductance into the

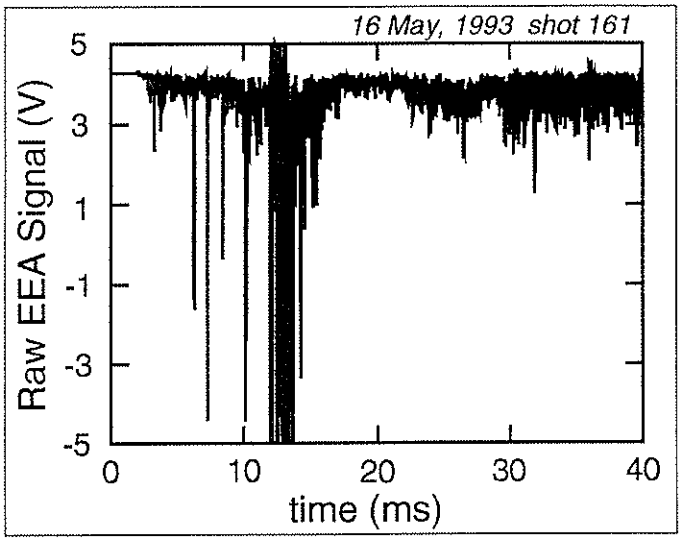


*Fig. 2.15 The raw EEA signal for a shot in which there was arcing between EEA electrodes.*

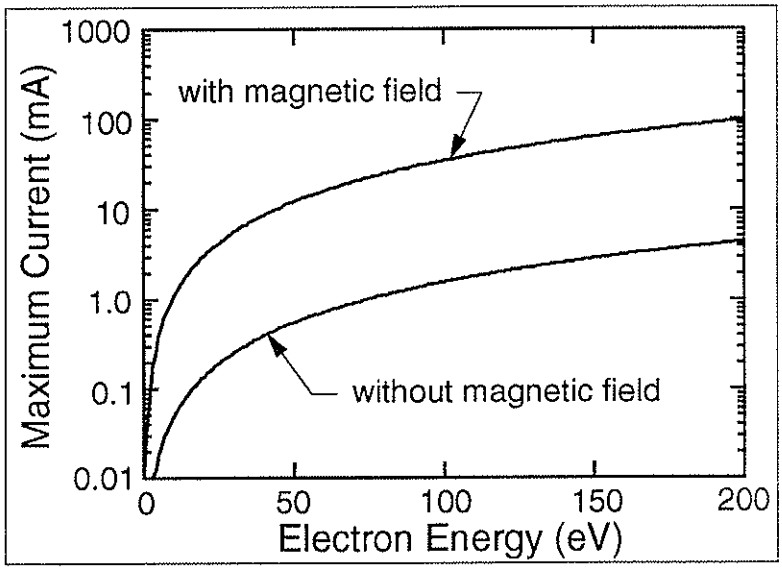


*Fig. 2.16 The space charge current limit passing through the EEA aperture with and without a magnetic field.*

probe shaft), and only during a run after the probe had recently been exposed to atmosphere. The clear explanation for the arcing is that when the probe heats up during the course of a run, the electrodes and insulaters in the analyzer channel outgas increasing the pressure inside the probe to that necessary for breakdown. The signature for such an event is the loss of repeller voltage, since the high voltage power supplies trip out when currents of ~1 mA are drawn from them.

I now take up the question of whether space charge affects the signal detected by the EEA. In the absence of a magnetic field, the maximum electron current that can be passed through a cylindrical opening, i.e. aperture, is given by (Moore, 1989)

$$I_{max} = 38.5E^{3/2}\left(D/L\right)^2 \ \mu A, \tag{2.11}$$

where $E$ is the electron energy in eV, $D$ is the aperture diameter and $L$ is the aperture length. The current is limited to the value given by eq. 2.11 because the radial electric field causes the beam to diverge. For the EEA aperture dimensions and a typical "maximum" electron current of 5 mA, electrons of energy less than 75 eV would be swept out of the beam. However, there was a strong magnetic field (800 Gauss) threading the axis of the aperture. The beam cannot diverge in the presence of a magnetic field, but the space charge still has an effect. Low energy electrons are repelled by the axial electric field generated by the electron space charge just inside the aperture. In this case, the maximum electron current that passes the aperture does not depend on the aperture geometry and is given by (Samuel, 1949)

$$I_{max} = 35E^{3/2}\ \mu A. \qquad (2.12)$$

For $I_{max}$=5 mA electrons with energy less than 30 eV are repelled at the entrance aperture. Fig. 2.16 shows the space charge current limit for the EEA aperture dimensions and no magnetic field (Eq. 2.11), and the current limit in the presence of a strong magnetic field (Eq. 2.12). The EEA is therefore a *fast* electron diagnostic, collecting electrons from the tail of the distribution only. The space charge effect explains why the electron temperature measured by the EEA does not agree with that from Langmuir probe measurements which are sensitive to the bulk of the electron population.

The space charge seen by an incoming electron as it enters the EEA aperture is just like the negative sheath potential near a floating Langmuir probe tip. The floating potential measured with a Langmuir probe under the standard interpretation (Hutchinson, 1987) depends on the local plasma potential and the electron temperature. It was already mentioned that a nonzero equilibrium plasma potential results in an offset of the effective repeller voltage (attempts to measure the equilibrium plasma potential at the edge of MST have met with difficulties resulting from the presence of the fast electron population, but the magnitude is found to be less than 40 V (Ji, 1994)). More important is the affect plasma potential fluctuations ($\tilde{\phi}_p$) and consequent sheath potential fluctuations have on the detected collecter current fluctuations ($\tilde{J}_e$). This effect was investigated by measuring the coherence between fluctuations in the EEA collecter current and the fluctuations in the floating potential, $\langle \tilde{J}_e \tilde{\phi}_f \rangle$, measured with two Langmuir probes, one situated upstream (with respect to the fast

electron flow) about 10 cm, and one downstream about 10 cm. Coherence is a spectral quantity that measures the percent correlation between two signals as a function of frequency (see section 4.5.3). The results of this experiment are shown in Fig. 2.17. The coherence between the floating potential 10 cm upstream and the EEA signal is ~20% at very low frequency but drops to the statistical noise level (~5%) above 15 kHz. The coherence with the downstream floating potential fluctuations remains above the statistical noise level at higher frequency. The asymmetry between the coherence upstream and downstream suggests a shadowing effect is responsible for the higher correlation downstream. The statistically significant correlation at very low frequency may reflect a small corruption of the electron current fluctuations signal, or may be the result of a true correlation between the potential fluctuation and the electron current fluctuations (or some combination of both). In any case, the coherence is small, indicating the fast electron current fluctuations are not dominated by parallel sheath potential fluctuations or plasma potential fluctuations. The exact level of coherence is important since it will be shown in Chapter 4 that the coherence between electron current fluctuations and magnetic fluctuations, $\langle \tilde{J}_e \tilde{B} \rangle$, which determines magnetic fluctuation induced transport is also quite small (~20%). The measurement is on safe ground however, since the measured coherence between the floating potential fluctuations and the magnetic fluctuations, $\langle \tilde{\phi}_f \tilde{B} \rangle$, is very low (~15%; Ji, 1994), meaning the maximum corruption of the coherence measurement between $\tilde{J}_e$ and $\tilde{B}$ is 4%.

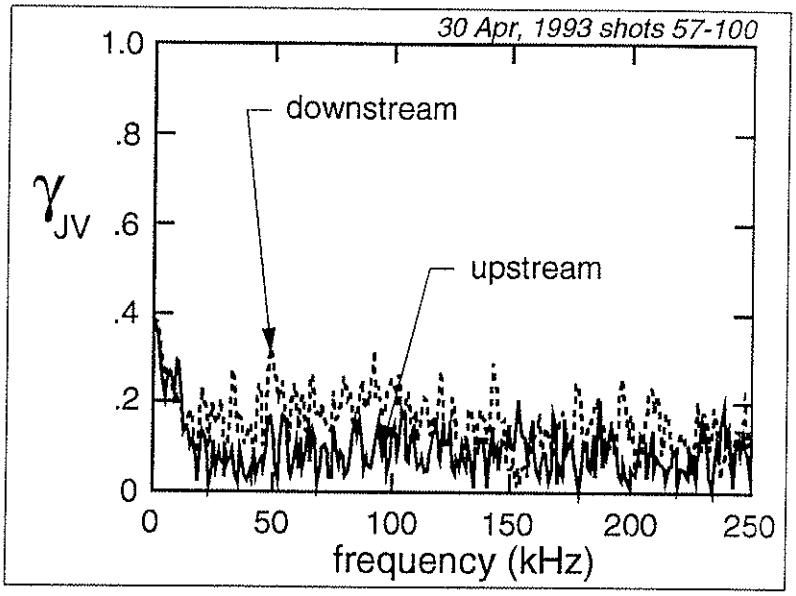


*Fig. 2.17 Coherence spectra between electron current fluctuations and floating potential fluctuations 10 cm away (solid: upstream, dashed: downstream). Floating potential data courtesy of H. Ji.*

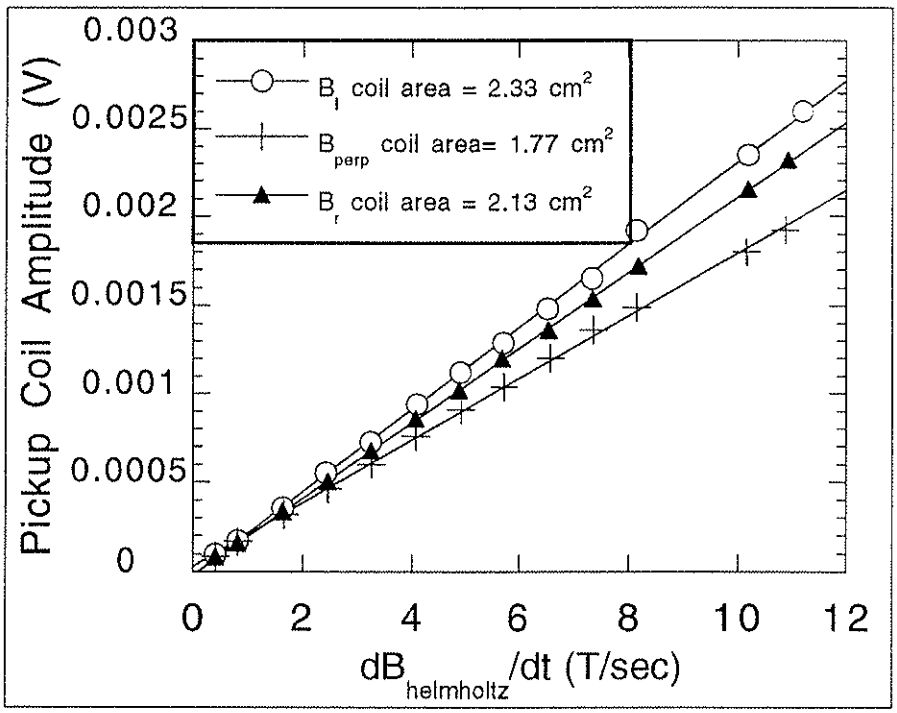


*Fig. 2.18 Pickup coil calibration curves*

2.2.6 Calibration of the Magnetic Pickup Coils

A changing magnetic flux through a coil or loop of wire induces a voltage across the ends of the wire according to Faraday's Law: $V = -d\Phi/dt$. If the magnetic field is assumed to be uniform across the area of the coil, then Faraday's Law becomes

$$V = -n_{turns} A \frac{dB}{dt} = -A_{effective} \frac{dB}{dt}, \tag{2.13}$$

where $n_{turns}$ is the number of turns in the coil, $A$ is the area enclosed by a turn of wire, and $B$ is the magnetic field strength through the coil. The pickup coils in the two channel EEA were calibrated by measuring the effective coil area, $A_{effective}$, which is the product of the area of a turn and the number of turns. A Helmholtz coil was driven with a variable frequency sinusoidal voltage. The current in the coil was measured by measuring the voltage across a 51.9 Ω resistor in series with the Helmholtz coil. Helmholtz coils provide a uniform magnetic field over a large region near their center. The Helmholtz coils were calibrated with a Hall probe at .56 Gauss per Ampere of current. Because a pickup coil detects the time derivative of the magnetic field, the amplitude of the induced voltage, $V_o$, increases linearly with frequency for a given field amplitude, $B_o$:

$$V_o = A_{effective} 2\pi f B_o. \tag{2.14}$$

The induced voltage as a function of frequency times magnetic field amplitude is shown in Fig. 2.18. The coils are identified by the component of the magnetic

field to which they were sensitive in the standard orientation in the plasma. For example, the coil sensitive to the field component parallel to the axes of the analyzer channels is identified as the $B_{||}$ coil because the analyzer channels were generally aligned parallel to the local magnetic field. The $B_r$ coil is the middle coil shown in Fig. 2.2, sensitive to radial magnetic field fluctuations in the plasma, and the coil identified as the $B_{\perp}$ coil is sensitive to the perpendicular magnetic flucutations in the flux surface. The effective area of the coils was constant within about 2% across the frequency range of interest (5-200 kHz). To within 2% the effective coil areas were: (1) 2.33 $cm^2$ for the $B_{||}$ coil, (2) 2.13 $cm^2$ for the $B_r$ coil, and (3) 1.77 $cm^2$ for the $B_{\perp}$ coil.

## *2.3 Thermocouple Calorimeter Probe*

### 2.3.1 Calorimeter Design

The EEA signal is sensitive to the perpendicular temperature of the fast electron distribution through the aperture transparency, but EEA measurements could not determine $T_{\perp}$. Absolute calibration of the EEA relied on knowing the aperture transparency which in turn relied on a measurement of $T_{\perp}$. This situation motivated the design of a wide aperture thermocouple calorimeter probe to provide measurement of another moment of the electron distribution.

Fig. 2.19 shows the design of the thermocouple calorimeter probe. It consists of a boron nitride particle shroud with a 1/8" diameter aperture. Inside the shroud is a .233 g graphite slug mounted on a quartz tube. Embedded inside the graphite is a type K thermocouple with 50 gauge wires (Omegaclad®) from Omega Inc. The thermocouple leads were fed through the

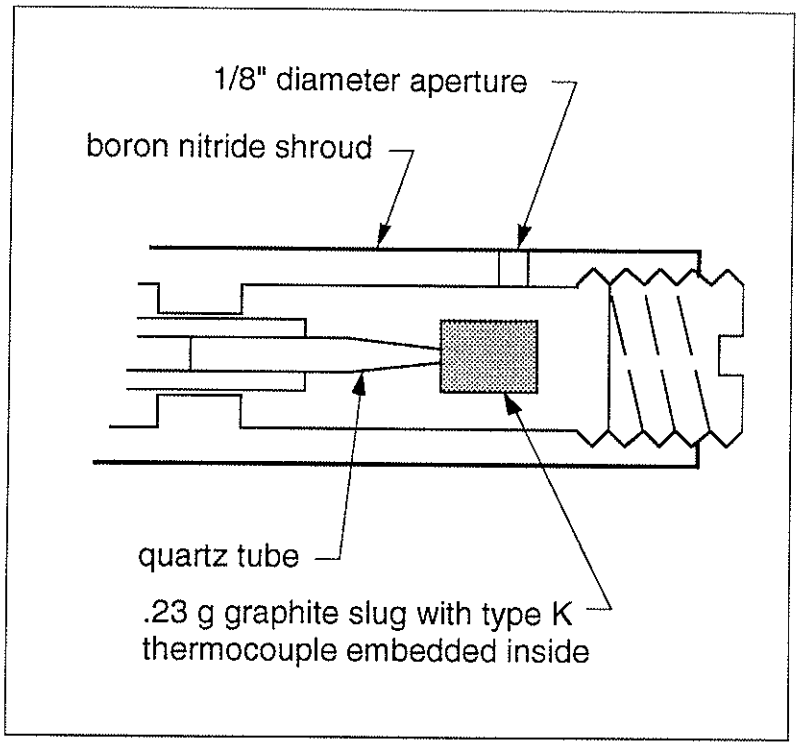


*Fig. 2.19 Schematic diagram of the thermocouple calorimeter.*

quartz tube and back through the probe shaft. 24 gauge type K thermocouple wires are fed through a bare wire vacuum seal (Conax Inc.) and spot welded to the 50 gauge wires. Outside the vacuum, the leads were connected to a cold reference junction circuit. The output from the reference junction went to a Tektronix AM502 differential amplifier, isolation amplifier, and digitizer identical to the arrangement used to measure the EEA collecter current. The graphite slug was maintained at MST machine ground by means of a 44 gauge wire connected to the probe shaft.

### 2.3.2 Calorimeter operation and signal interpretation

When the calorimeter was inserted into the edge of the plasma, the aperture was aligned to the local magnetic field direction just as for the EEA. The graphite slug absorbs energy from the plasma coming through the aperture. Because the graphite is mounted on a quartz tube and the thermocouple wires are very small, the thermal contact with the surroundings is minimal. In addition the graphite mass is large enough that its temperature did not increase to the point where radiative heat loss was important. The increase in the temperature of the graphite was detected by the voltage change across the thermocouple junction.

The measurement is inherently an integrated heat flux measurement because the heat energy is deposited in the graphite in a time (45 ms) that is short compared to the thermal equilibration time (~1 s). Once the temperature of the graphite comes to equilibrium, the total temperature rise due to heat deposition from the plasma is determined from the linear term in the known response of type K thermocouple wire, $\Delta T = 24152\Delta V$ °C. This form of the thermocouple response is accurate to much better than 1% over the temperature range of interest (see ref. Omega). The energy deposited in the graphite is found from the equation, $\Delta E = mC\Delta T$ where $m$ the mass of the graphite and $C$ is the specific heat of graphite ($C$= .715 J/g°C).

The energy deposited in the graphite has three possible contributions: (1) electron convective heat flux, (2) ion convective heat flux, and (3) radiation. The convective parallel heat flux associated with a drifted Maxwellian velocity distribution for a species is

$$q_{\parallel} = nv_{drift}\left(\frac{3}{2}T_{\parallel} + T_{\perp} + \frac{1}{2}mv_{drift}^{2}\right). \qquad (2.15)$$

The term in parentheses is comparable for two species at comparable temperatures. However, the particle flux, $nv_{drift}$, is greater for electrons by approximately the square root of the mass ratio, $\sqrt{m_i/m_e} \approx 40$. In addition, the aperture transparency to ions, while much greater than for the EEA aperture was still only 10-20% as calculated with the Monte Carlo code. The ion heat flux incident on the graphite slug was therefore negligible. The effect of the electron space charge (80-90% of the ion charge was eliminated by the aperture) inside the calorimeter aperture had the same effect as for the EEA, namely that the low energy electrons are effectively repelled at the entrance and only the fast electrons impinge on the graphite element. It remains to estimate the energy flux due to photon radiation incident on the graphite. An upper limit on the radiation flux is found by assuming 100% of the Ohmic input power to the plasma is radiated out. The energy density at the edge is then

$$Q_{rad} < \frac{I_{plasma} V_{loop}}{2\pi R 2\pi a} \approx 10 \text{ Wcm}^{-2}, \qquad (2.16)$$

where $I_{plasma}$=210 kA and $V_{loop}$=15 V. Eq. 2.16 provides an upper limit on the energy flux looking radially into the plasma, and also on the flux looking parallel (poloidally) to the local field at the edge. The upper limit is sufficient to eliminate radiation as a sustantial contributor to the heat flux measured by the calorimeter since the measured flux is two orders of magnitude larger than eq. 2.16 suggests was possible from radiation alone (see chapter 3). Fast electron heat flux is therefore the dominant contribution to the measured heat flux incident on the graphite slug in the calorimeter probe.

The energy deposited in the graphite during a discharge is the integral of the fast electron heat flux.

$$\Delta E = A\int q_{\parallel e}(t)dt, \tag{2.17}$$

where $A$ is the aperture area. There is no transparency factor since the aperture radius is large compared to the typical electron Larmor radius; the transparency to electrons is unity. An average parallel fast electron heat flux is found from

$$\left\langle q_{\parallel e}\right\rangle = \frac{\Delta E}{A\tau_{pulse}}, \tag{2.18}$$

and an estimate of the mid-discharge heat flux is found by assuming a time behavior of the heat flux that is similar to the plasma current,

$$q_{\parallel e}^{cal}(t) = \frac{\Delta E}{A}\frac{I_{plasma}(t)}{\int I_{plasma}dt}. \tag{2.19}$$

Measurement of the fast electron heat flux with the thermocouple calorimeter probe provided a means of absolutely calibrating the EEA, i.e. determining the aperture transparency or perpendicular temperature. The results of the measurement of the fast electron heat flux and determination of $T_{\perp}$ are presented in chapter 3.

## References

A. Almagri, "The effects of magnetic field errors on reversed field pinch plasma," Ph.D. thesis, University of Wisconsin-Madison, 1994.

A. Almagri, S. Assadi, S.C. Prager, J.S. Sarff, and D.W. Kerst, "Locked modes and magnetic field errors in the Madison Symmetric Torus," Phys. Fluids B **4**, 4080 (1992).

S. Assadi, "Measurement of magnetic turbulence structure and nonlinear coupling of tearing fluctuations in the Madison Symetric Torus reversed field pinch," Ph.D. thesis, University of Wisconsin-Madison, 1994.

S. Banville, "The B-dot amp as a diagnostic for magnetic field measurements," Wisconsin Plasma Physics Report PLP #1072 (1990).

S.R. Burns, W.A. Peebles, D. Holly, and T. Lovell, "Madison symmetric torus far-infrared interferometer," Rev. Sci. Instrum. **63**, 4993 (1992).

D.J. Den Hartog, "A simple, high performance Thomson scattering diagnostic for high temperature plasma research," submitted to Measurement Science and Technology (1994).

R.N. Dexter, D.W. Kerst, T.W. Lovell, S.C. Prager, and J.C. Sprott, "The Madison Symmetric Torus," Fusion Tech. **19**, 131 (1991).

M.J. Druyvesteyn and F.M. Penning, "The mechanism of electrical discharges in gases of low pressure," Rev. Mod. Phys. **12**, 87 (1940).

R.F. Ellis, J.C. Ingraham, P.G. Noonan, and H.W. Tsui, "Fast electrons in the edge region of reversed and non-reversed discharges in HBTX-1C," Maryland Report, UMLPR 90-016 (1990).

I.H. Hutchinson, *Principles of Plasma Diagnostics,* Cambridge University Press, (1987).

S. Hokin, A. Almagri, M. Cekic, B. Chapman, N. Crocker, D.J. Den Hartog, G. Fiksel, J. Henry, H. Ji, S. Prager, J. Sarff, E. Scime, W. Shen, M. Stoneking, and C. Watts, "Reversed-field pinch studies in the Madison Symmetric Torus," J. of Fusion Energy **12**, 281 (1993).

J.C. Ingraham, R.F. Ellis, J.N. Downing, C.P. Munson, P.G. Weber, and G.A. Wurden, "Energetic electron measurements in the edge of a reversed-field pinch," Phys. Fluids B **2**, 143 (1990).

H. Ji, private communication (1994).

J.H. Moore, C.C. Davis, and M.A. Coplan, *Building Scientific Apparatus,* 2nd Ed., Addison-Wesley (1989).

*Omega® Complete Temperature Measurement Handbook and Encyclopedia®*, vol. 27, p. Z-14.

W.H. Press, S.A. Teukolsky, W.T. Vettering, and B.P. Flannery, *Numerical Recipes in Fortran,* 2nd Ed., Cambridge University Press (1986).

E. Rudberg, "Inelastic scattering of electrons from solids," Phys. Rev. **50**, 138 (1936)

A.L. Samuel, Proc. IRE, **37**, 1252 (1949)

E. Scime and S. Hokin, "Design and calibration of a fast-time resolution charge exchange analyzer," Rev. Sci. Instrum. **63**, 4527 (1992).

J.T. Tate and P.T. Smith, "The efficiencies of ionization and ionization potentials of various gases under electron impact," Phys. Rev. **39**, 270 (1932).

# 3. Fast Electron Generation

## *3.1 Fast electron generation mechanisms*

### 3.1.1 Runaway electrons

The presence of electrons with energies much greater than the thermal energy has been observed in fusion plasma experiments since the 1950s. One of the principle means of detecting energetic electrons which can have energies of many MeV in a tokamak is through the hard X-ray radiation emitted from a limiter exposed to the electron flux. A simple explanation for why such high energy electrons exist comes from considering the forces on a test electron in a plasma with a d.c. applied electric field. The accelerating force of the electric field is opposed by the friction or drag on the electron due to Coulomb collisions with other plasma particles: $m\,dv/dt = qE - mvv$, where $v$ is the classical Coulomb collision frequency. Since the collision frequency is proportional to $1/v^3$, the collisional friction is a strongly decreasing function of velocity. Above a critical velocity there is no steady state solution to the equation of motion and the electron is accelerated until it strikes a solid target; the electron is said to "runaway." The details of the kinetic theory of runaway electrons were worked out in the 1960s (Dreicer, 1959; Gurevich, 1961; Kruskal, 1964) and a review of runaway electron physics was given by Knoepfel and Spong (Knoepfel, 1979). Since the entire distribution function is distorted by the presence of an electric field the test particle description is only useful as a heuristic picture. A sophisticated treatment requires dividing velocity space into as many as five regions, solving some approximation to the full kinetic problem in each region and matching the solutions across the

boundaries. The rate at which runaway electrons are produced (per $cm^{-3}$) was calculated from such a treatment (Kruskal, 1964) and is given by,

$$S = 0.35 n \nu_{th} \left( \frac{E_c}{E_\parallel} \right)^{3/8} \exp\left( -\frac{E_c}{4E_\parallel} - \left( \frac{2E_c}{E_\parallel} \right)^{1/2} \right), \tag{3.1}$$

where $\nu_{th}$ is the electron collision frequency for a thermal electron and $E_\parallel$ is the component of the applied electric field parallel to the magnetic field. $E_c$ is called the critical electric field; it is the electric field magnitude that causes thermal electrons to run away. An expression for the critical electric field is given by (Knoepfel, 1979)

$$E_c = \frac{4\pi n e^3}{T_e} \left( \ln \Lambda + \ln\left( \frac{4\pi n e^3 \ln \Lambda}{T_e E_\parallel} \right) \right). \tag{3.2}$$

Runaway electron generation is an extremely strong function of the ratio of the applied electric field to the critical electric field (Fig. 3.1). The onset of runaway production occurs at values of $E_\parallel/E_c$ around 3%. For typical MST plasma parameters of interest in this work ($n$=$10^{13}$ $cm^{-3}$, $T$=100 eV), the critical electric field is about 40 V/m. The applied electric field on axis is typically 1.5 V/m, making $E_\parallel/E_c$~4%. The conditions for runaway production exist in MST.

Runaway electrons are collisionless and so "free-fall" in the applied electric field. If particle confinement is good enough, runaway electrons reach relativistic energies. The relativistic equation of motion for the electron is

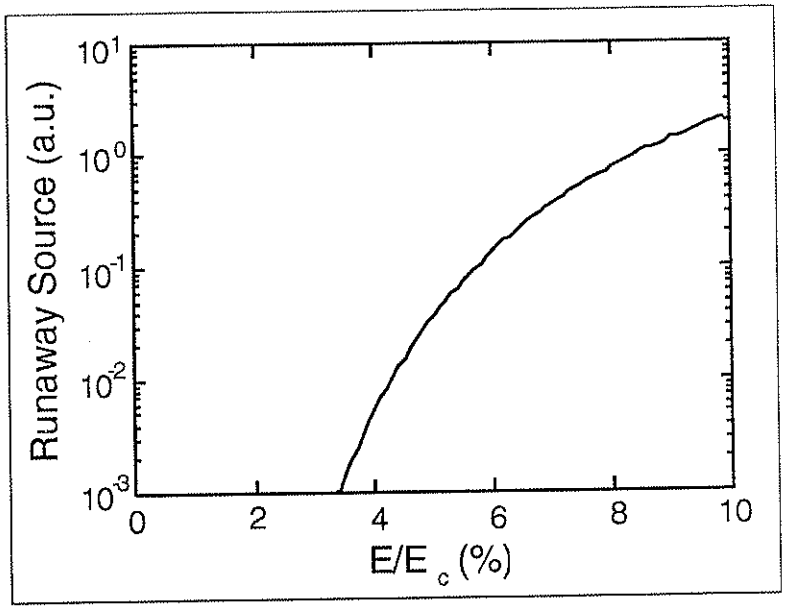


*Fig. 3.1 The runaway electron source function increases strongly with the applied electric field.*

$d/dt(\gamma mv) = qE_{\parallel}$. Integrating the equation of motion to time $\tau$ and solving for the kinetic energy of the electron gives

$$W_K = (\gamma - 1)mc^2 = mc^2\left(\sqrt{1+\left(\frac{eE_{\parallel}\tau}{mc}\right)^2} - 1\right). \tag{3.3}$$

In tokamaks, although the applied electric fields are small, around 0.1 V/m, confinement times are long, around 1 s, generating runaway electron energies up to tens of MeV. If the runaway confinement time in MST is comparable to the global confinement times (~1 ms), runaway energies should reach 100 keV ($E_{\parallel} \approx 1.5$ V/m).

Although fast electrons are observed in MST both in the core (Hokin, 1992) and at the edge (below) with energies up to several times the thermal

energy, evidence for significant runaway electron flux in MST is non-existent. The X-ray spectrum in MST exhibits a 1 keV fall-off at energies above 1 keV (Hokin, 1992). One factor affecting runaway electron production in the RFP is magnetic field shear. The applied electric field is in the toroidal direction, but the field is mostly poloidal at the edge of the RFP. Since the applied electric field can cause electron runaway only parallel to the magnetic field, runaway production is confined to the core region of the RFP. While magnetic shear acts to localize runaway production to the core of the RFP, the effect on the runaway energy is not qualitatively significant, altering the acceleration time by at most a factor of two.

No definite conclusions on true runaway electrons in the RFP are attempted in this work, and no systematic effort has been made in MST to date to quantify the maximum energy of hard X-ray radiation in the MST plasma. However, qualitatively the nonexistence of 100 keV runaway electrons is evidence that runaway electrons are more poorly confined than thermal electrons. Such a conclusion supports the measurements reported in Chapter 4 of this work, namely that magnetic fluctuation induced transport through a stochastic magnetic field dominates the transport in the core of the RFP. Diffusion through a stochastic magnetic field is faster for particles with higher velocity, therefore, runaway electrons escape the plasma faster in the presence of a stochastic field. The diffusion coefficent for a very fast (i.e. test) electron in a stochastic field is given by $D = \left(\tilde{B}_r/B_o\right)^2 L_{ac} v_{\|}$ (Rechester, 1978), where $L_{ac}$ is the parallel autocorrelation length for the magnetic fluctuations (stochastic transport is discussed below in connection with the kinetic dynamo theory, and at greater length in Chapter 4). The confinement time (or acceleration time) for a runaway

electron in a stochastic magnetic field can be estimated as $\tau_{runaway} \approx a^2/(2D_{runaway})$. In the nonrelativistic limit, the solution for the runaway electron kinetic energy when it reaches the limiter is $W_K \approx qE_{\|}a^2/D_M$ where $D_M = (\tilde{B}_r/B_o)^2 L_{ac}$ is the magnetic diffusivity. For the known fluctuation level (~2%), correlation length (~1 m), and electric field (~1.5 V/m) in MST, the runaway energy is of order 1 keV, comparable to the energy spread of the observed the X-ray spectrum.

### 3.1.2 The kinetic dynamo model

The relevance of the discussion of runaway electrons in the RFP lies not so much in the production of true runaway electrons, but in the production of fast electrons. The runaway mechanism, or "slide-away" mechanism as it is sometimes called when discussing the production of fast rather than runaway electrons, has been invoked in order to explain the presence of the poloidal or dynamo current in the RFP. This theory is called the kinetic dynamo theory (KDT) (Jacobson, 1984a; Jacobson, 1984b; Schoenberg, 1991). Before describing the KDT, a brief description of the MHD dynamo is given.

The equilibrium RFP magnetic configuration is qualitatively described by a force-free state, $\boldsymbol{J}\times\boldsymbol{B}=0$ or equivalently $\nabla\times\boldsymbol{B}=\mu\boldsymbol{B}$, where $\mu$ is a constant (Taylor, 1974). The current is everywhere parallel to the magnetic field and magnetic field profiles are given by Bessel functions (the Bessel function model or BFM). A model with similar magnetic field profiles, but which forces the current to zero at r/a=1 and is consistent with existing profile measurements in the RFP is the modified polynomial function model or MPFM (Shen, 1991). MPFM magnetic field and current profiles for discharge plasma parameters of

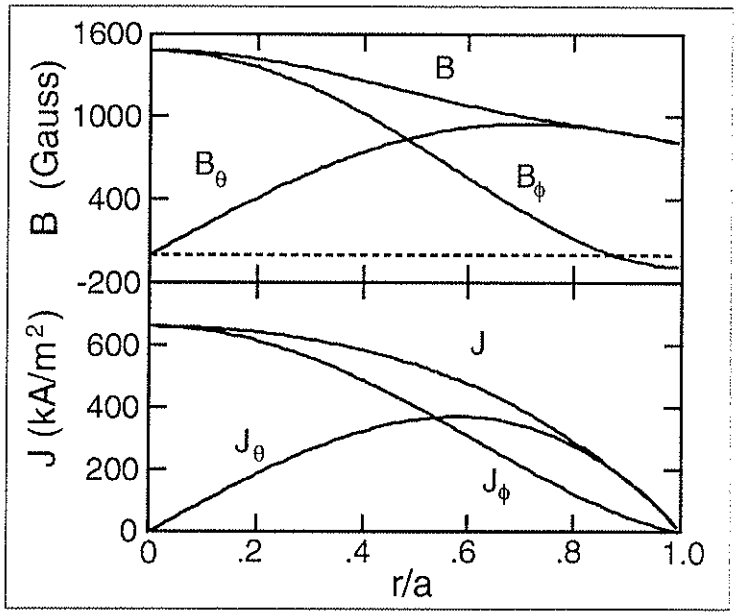


*Fig. 3.2 Modified polynomial function model field and current profiles for $I_p$=210 kA, F=-0.2, and $\Theta$=1.85.*

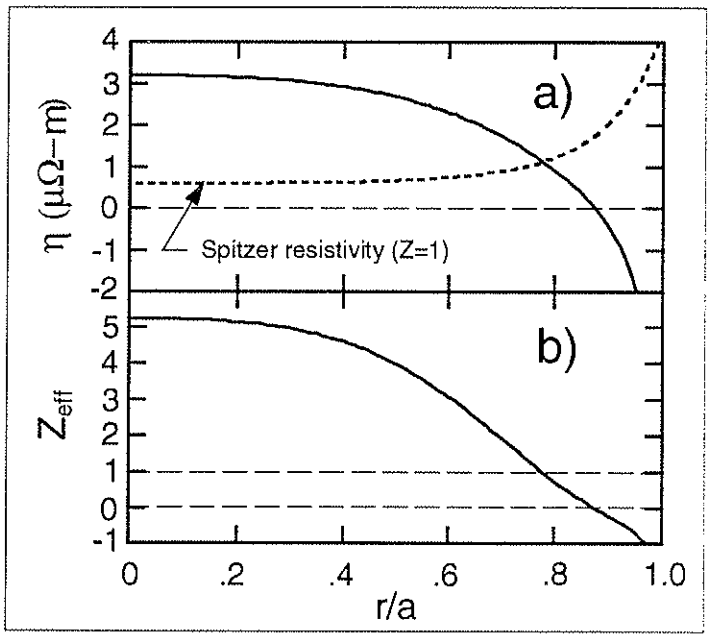


*Fig. 3.3 a) The parallel applied toroidal electric field divided by the parallel current from the MPFM (solid) compared with a Spitzer resistivity profile for Z=1 (dashed), b) the Zeff profile required to produce the observed current profile without a dynamo.*

interest in this work are shown in Fig. 3.2. The applied electric field is in the toroidal direction and has a typical (on-axis) value of 1.5 V/m in MST. Fig. 3.3a shows the effective resistivity profile required to satisfy the most naive version of Ohm's law: $\eta = E_{\|}/J_{\|}$. Also shown in Fig. 3.3a is the Spitzer resistivity profile for $Z_{eff}$=1 and a broad temperature profile ($T = T_o\left(1-(r/a)^4\right)$ with a central value of 100 eV. Spitzer resistivity is proportional to $Z_{eff}/T^{3/2}$ and is likely to be peaked at the edge for any reasonable $Z_{eff}$ profile both due to lower temperature at the edge and larger impurity content. In order to satisfy the naive version of Ohm's law, the $Z_{eff}$ profile ($Z_{eff} = E_{\|}\Big/\left(J_{\|}\,\eta_{spitzer}\Big|_{Z=1}\right)$) would have to be centrally peaked, fall below unity at r/a=0.75 and go negative outside r/a=0.9 (Fig. 3.3b). While a centrally peaked $Z_{eff}$ profile is not beyond the bounds of reasonability, it is impossible for it to fall below unity (not to mention becoming negative). In order to reproduce the observed RFP field profiles a poloidal current drive mechanism must be invoked. Such a mechanism in the absence of an externally applied poloidal electric field is called a dynamo.

The MHD or fluid dynamo theory provides poloidal current drive through the more complete version of Ohm's law: $E_{\|} + (\boldsymbol{v}\times\boldsymbol{B})_{\|} = \eta J_{\|}$. Near the edge of the RFP where the magnetic field is mostly poloidal there is no externally applied parallel electric field, so Ohm's law becomes $(\boldsymbol{v}\times\boldsymbol{B})_{\theta} = v_r B_\phi - v_\phi B_r = \eta J_\theta$. There is no equilibrium radial flow or equilibrium radial magnetic field (spatially averaged), so the poloidal current drive must result from correlated turbulent fluctuations. The MHD dynamo is summarized by the equation

$$\eta J_\theta = \left\langle \tilde{v}_r \tilde{B}_\phi \right\rangle - \left\langle \tilde{v}_\phi \tilde{B}_r \right\rangle. \qquad (3.4)$$

3D computer simulations of the tearing mode activity in the RFP predict that the fluid dynamo exists and can maintain the equilibrium field configuration (Schnack, 1985).

The authors of the KDT took issue with the validity of the Ohm's law which has a locally defined resistivity in light of the low collisionality of the RFP plasma and the rapid radial diffusion that likely results from a stochastic magnetic field. Observations that the poloidal current is carried by fast, collisionless electrons (Ingraham, 1990) in the ZT-40M RFP lended credence to the arguments of the KDT authors. The presence of large amplitude magnetic fluctuations due to tearing instabilities is believed to destroy the magnetic flux surface topology of the RFP; field lines wander across the minor radius of the plasma (see Ch.4, section 4.3). In such a stochastic magnetic field, a fast (i.e. collisionless) electron can be transported from the core to the edge by flowing quickly along the field. The stochastic diffusion coefficient for the fast, test particle population is given by (Rechester, 1978) $D_{st} = \left\langle \tilde{B}_r / B_o \right\rangle^2 L_{ac} v_{\|}$. $L_{ac}$ is the parallel autocorrelation length for the magnetic fluctuations. Jacobson and Moses solved a kinetic equation for the steady state fast electron distribution that took stochastic diffusion into account:

$$\frac{-eE_{\|}}{m}\frac{\partial f}{\partial v_{\|}} = \left.\frac{\partial f}{\partial t}\right|_{coll} + |v_{\|}|\frac{\partial}{\partial x}\left(D_M \frac{\partial f}{\partial x}\right), \qquad (3.5)$$

where $D_M = \left\langle \tilde{B}_r / B_o \right\rangle^2 L_{ac}$ is the magnetic diffusivity. The solutions indicated that electrons accelerated in the core region (slideaway electrons) could carr

parallel momentum by streaming along the stochastic field to the edge region where they would provide the poloidal dynamo current. The KDT is a test particle model and assumes a preexisting stochastic magnetic field with the RFP field configuration. The solutions then show the configuration is sustainable by the collisionless electron current transported from the core. As a test particle model, the KDT is not self-consistent; it does not consider the effect the magnetic fluctuation induced momentum transport has on the equilibrium, and does not require that Ampere's law be satisfied by the turbulent fluctuations responsible for the transport. Terry and Diamond (Terry, 1990) provided a self-consistent treatment of the turbulent transport of electron momentum by magnetic fluctuations, the mechanism implied by the KDT. They concluded that net momentum transport was not possible, except in a very limited parameter regime. Despite the theoretical argument against the KDT, until now the experimental evidence from the RFP tended to support its general predictions. That experimental evidence can be summarized in one statement: the edge poloidal current in the RFP is carried mostly or completely by a population of electrons with an energy distribution (i.e. temperature) greater than the central electron temperature.

An attempt is made in this work to test the predictions of the KDT by measuring the characteristics of the edge fast electron population in MST.

### 3.1.3 Other fast electron generation mechanisms

While the central thrust of this chapter is to test the KDT mechanism for fast electron generation and poloidal current drive, a brief review of other fast electron generation mechanisms is given here.

Yoshida, Hasegawa, and Wakatani (YHW) proposed that a fast electron population is generated at the edge of the RFP by Landau damping of kinetic Alfvén waves (KAW) on the tail of the electron distribution (Yoshida, 1993). The theory makes a clear prediction that a beam-like distribution of electrons is generated at the Alfvén velocity ($v_A = B/\sqrt{\mu_o m_i n}$) and the conditions required for this mechanism to be active is that the edge Alfvén velocity be greater than the edge (bulk) thermal velocity. It is unlikely that this mechanism is important in the generation of fast electron in MST because the Alfvén velocity is less than the thermal electron velocity out to the extreme edge of the plasma and the edge fast electron thermal velocity is significantly greater than the edge Alfvén velocity as will be shown below. Fig. 3.4 shows a model profile (MPFM) of the Alfvén velocity and the electron thermal velocity (here, $v_{th} = \sqrt{T/m}$) that is consistent with global and edge measurements in MST ($I_p$=210 kA, $\bar{n}$=$10^{13}$ cm$^{-3}$, $n(a)$=$10^{12}$ cm$^{-3}$, $T_{eo}$=100 eV, $T_e$(a)=20 eV). Edge measurements will be presented below and compared with the predictions of the YHW model.

Another interesting issue brought by the YHW paper is the possible connection between fast electrons in the RFP and the high frequency turbulence. In the core of the RFP, thermal (and fast) electrons are super-Alfvénic. YHW predict that ion cyclotron waves should be Cerenkov emitted by the Alfvénic and super-Alfvénic electrons. Turbulent fluctuations out to the ion cyclotron frequency are observed in MST (Scime, 1992). A first order test of this conjecture is made here by comparing the high frequency magnetic fluctuations (though still well below the ion cyclotron frequency of ~1 MHz) for high and low density discharges (see section 3.2.7 for discharge conditions) in MST at a plasma current 210 kA (Fig. 3.5). The density difference in the two discharge

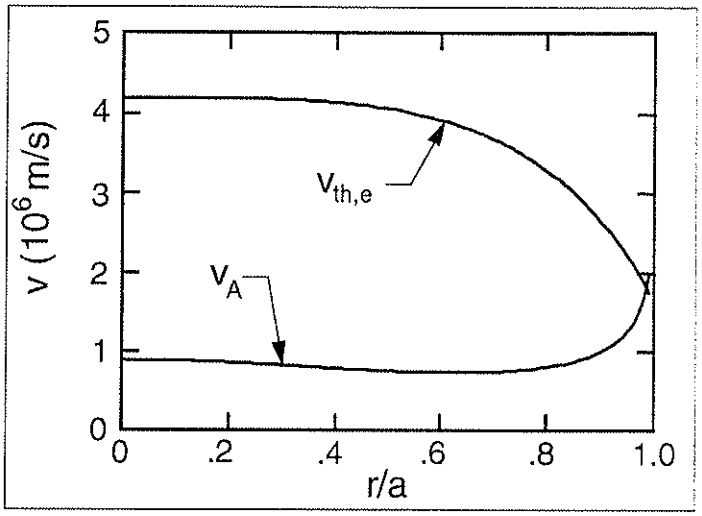


*Fig. 3.4 A comparison of model profiles for the electron thermal velocity and the Alfven velocity in a typical (high density) MST discharge.*

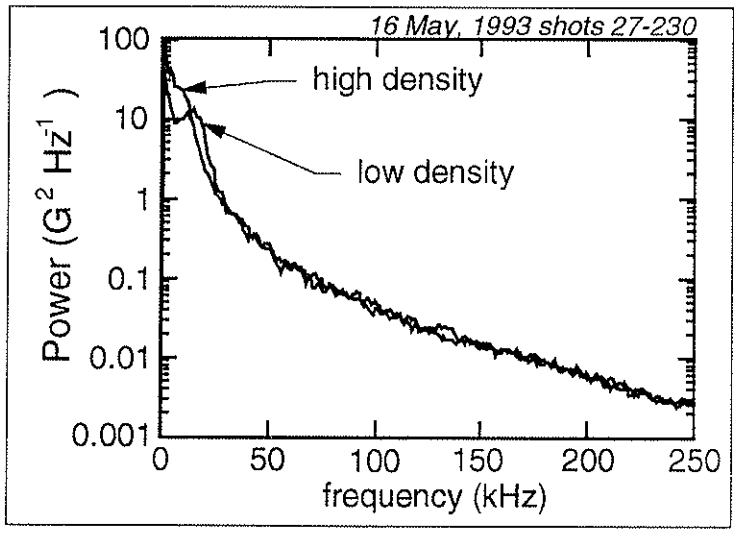


*Flg. 3.5 The frequency spectrum of toroidal magnetic fluctuations is shown for a high density and low density case both at 210 kA.*

conditions results in a difference in the Alfvén velocity. The high frequency magnetic fluctuation spectrum is not seen to change significantly with plasma density. Further experiments along this line are warranted to more completely test the YHW conjecture.

Erba *et. al.,* proposed that fast electrons in the RFP are generated in the region of magnetic reconnection associated with the resistive tearing instabilities in the RFP (Erba, 1993). In the presence if finite resistivity magnetic field lines can tear and reconnect at points where a component of the field goes to zero (i.e. X-points of magnetic islands). Using a dimensional analysis argument for a Sweet-Parker-like reconnection event (Parker, 1967), Erba, *et. al.,* derive a equation for the average velocity of the electrons carrying the current in the reconnection layer,

$$v_{fast} \approx v_d S^{1/2} \varepsilon^{3/2}, \tag{3.6}$$

where $v_d = J/ne$ is the drift velocity associated with the mean current, $S = \mu_o \pi a v_{Alf}/\eta$ is the Lundquist number (using the form of Erba *et. al.,*), and $\varepsilon \approx 0.1$ is the fraction of the local magnetic flux participating in the reconnection. For typical experimental values of interest in this work, Eq. 3.6 predicts fast electron velocities about 25 times the mean drift velocity, about $7 \times 10^6$ m/s in the outer region of MST ($S=6 \times 10^5$, using Spitzer resistivity with $Z_{eff}=3$ and $v_d=3 \times 10^5$ m/s). The reconnection model predicts a time averaged fast electron current density of about 10% of the mean current. These predictions will be compared with the data in MST.

Measurements of the MHD dynamo electric field in MST (Ji, 1994a) confirm the existence of an equilibrium poloidal electric field at the edge. Using Langmuir probes and magnetic pickup coils, the poloidal electric field induced by ExB flow fluctuations correlated with magnetic fluctuations,

$$E_{dynamo} = \left\langle \tilde{\boldsymbol{v}} \times \tilde{\boldsymbol{B}} \right\rangle_{\theta} = \frac{\left\langle \tilde{\boldsymbol{E}}_{\perp} \cdot \tilde{\boldsymbol{B}}_{\perp} \right\rangle}{B_o}, \tag{3.7}$$

was found to be 3-5 V/m between discrete dynamo events (see section 3.2.3) and rising to 10-20 V/m during a dynamo event. The MHD dynamo electric field is greater than the applied toroidal electric field on the magnetic axis (~1.5 V/m) and represents a significant parallel force on the (fast) electron population at the edge.

## *3.2 Measurement of the equilibrium fast electron distribution*

### 3.2.1 Field-aligned electron current

The electron energy analyzer (EEA) probes described in the previous chapter were employed to measure the fast electron distribution in RFP discharges in the Madison Symmetric Torus operated at low plasma current ($I_p$<250 kA). The directions of the toroidal plasma current and average toroidal magnetic field are determined by the polarity of the connections of the poloidal and toroidal transformers respectively. In the configuration used for experiments in this work, the toroidal plasma current was in the clockwise direction (viewed from above) and the average toroidal magnetic field was

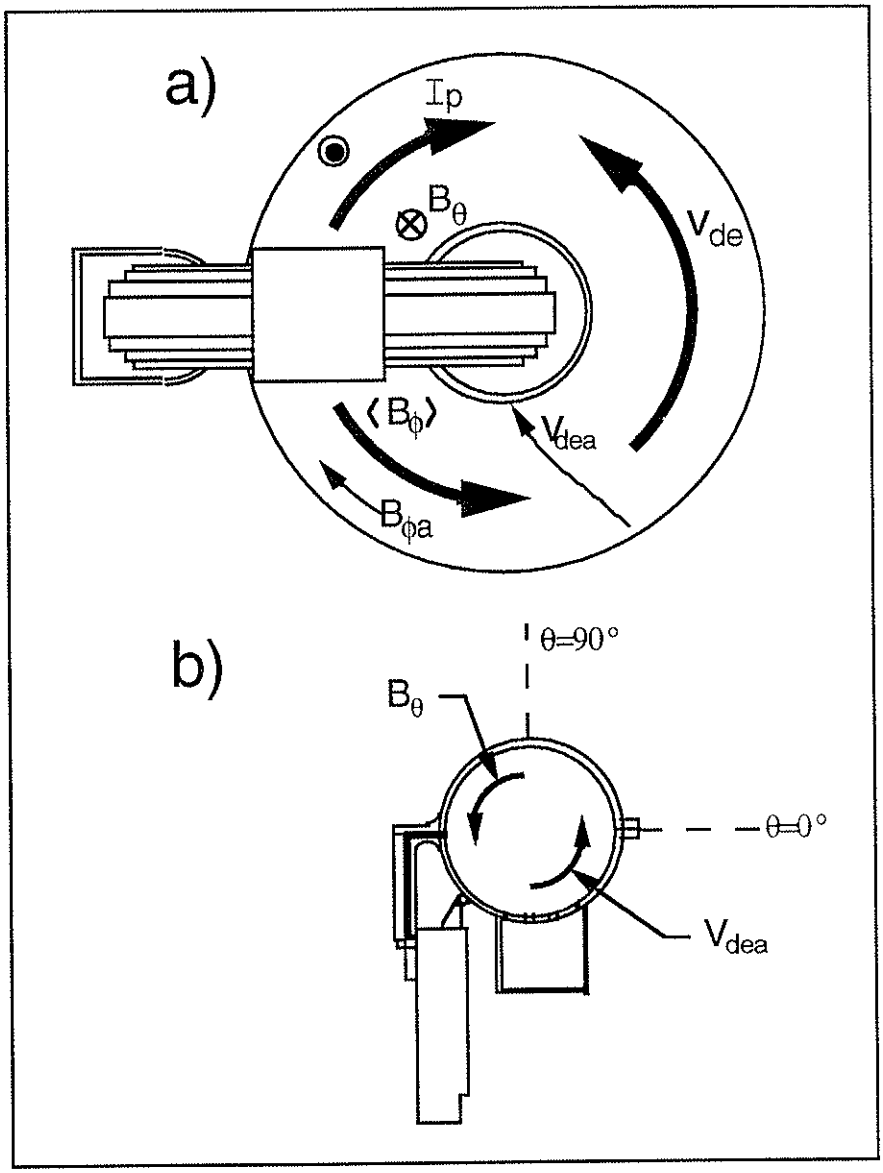


*Fig. 3.6 a) Top view of the MST showing the relative directions for the current, magnetic field components and electron drift. b) A poloidal cross-section of the MST showing the directions of electron drift and poloidal magnetic field at the edge.*

counter-clockwise (Fig. 3.6a). Current carrying electrons drift counter-clockwise in the core and from lower to higher poloidal angle at the edge. Outside the reversal surface, current-carrying electrons flowing along the magnetic field have a toroidal velocity component that is against the applied toroidal electric field.

The EEA probe was inserted radially and was rotated about its axis in a shot to shot manner to map out the directionality of the electron flux relative to the equilibrium magnetic field. The results of the rotation scan for a typical series of 240 kA discharges is shown in Fig. 3.7. The detected electron current was averaged over a 5 ms segment of the discharge during and just after the current peak and plotted versus the facing angle of the EEA (channel #1). 0° corresponds to the EEA facing the poloidal direction (+/- 3°) in such a way as to collect electrons flowing from lower to higher poloidal angle. Two peaks are evident in Fig. 3.5 separated by 180° and offset from the poloidal facing angle by less than 10°. The direction of the offset from poloidal is consistent with the direction of the local field lines. Discussion of the asymmetry in the current detected from opposite directions along the field is delayed to section 3.2.2, but note that the asymmetry has the correct sign to give net electron current flowing along the field consistent with the directions indicated in Fig. 3.7, i.e. net electron flow is against the applied electric field at the edge.

A similar facing angle scan is shown in Fig. 3.8 for two discharge conditions in which the pitch of the field lines at the wall was different ($I_p$=210 kA). The angle that the field line makes with the poloidal is given by $\vartheta = \arctan\left(B_{\phi a}/B_{\theta a}\right) = \arctan(F/\Theta)$ near the wall, where $F = B_{\phi a}/\langle B_\phi \rangle$ and $\Theta = B_{\vartheta a}/\langle B_\phi \rangle$. For the discharge conditions indicated by open circles in Fig. 3.8

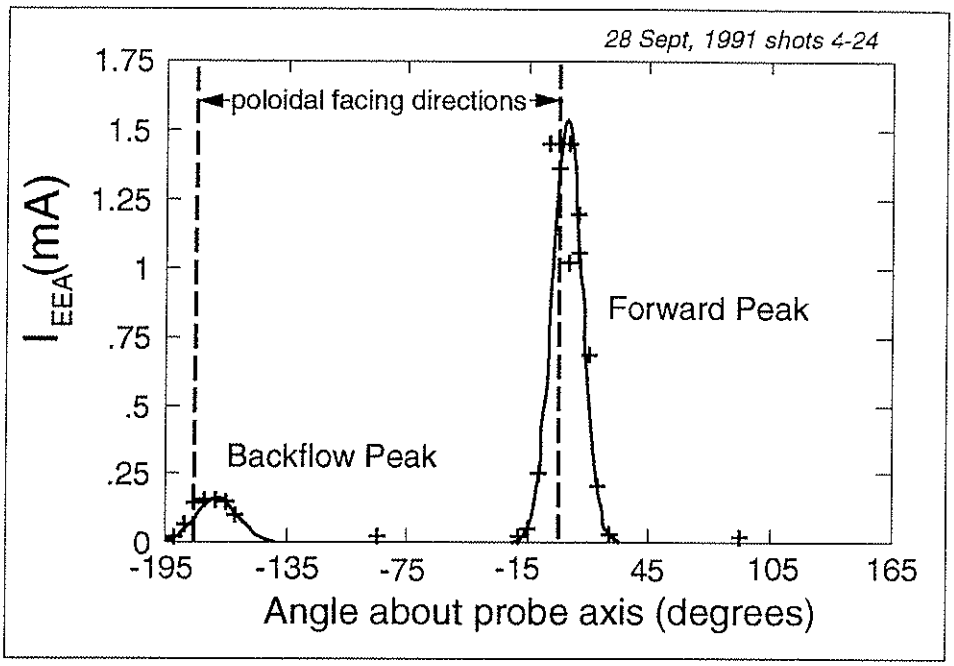


*Fig. 3.7 The EEA facing angle scan shows a large "forward" flowing peak and a small "backflowing" peak aligned with the local edge magnetic field direction.*

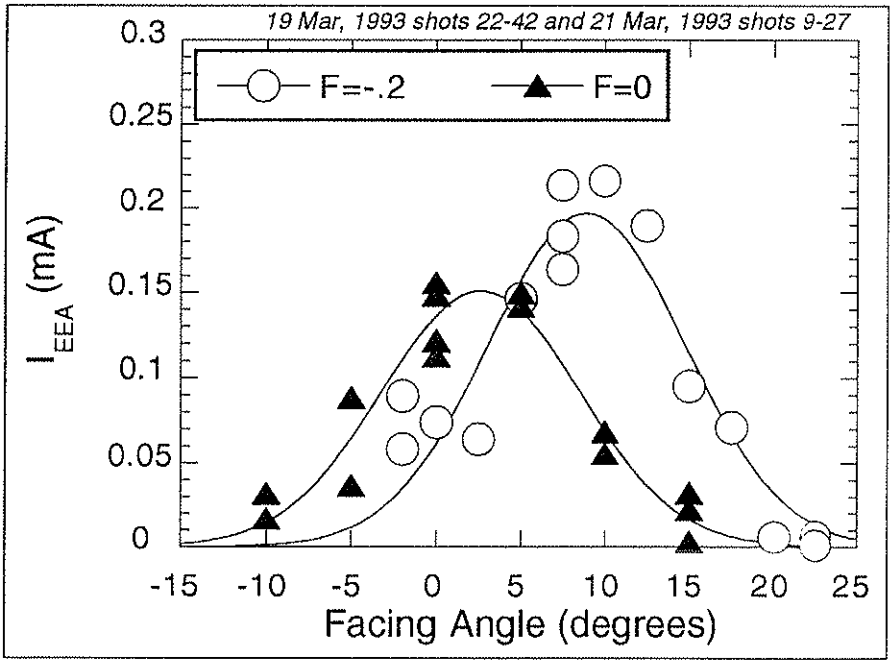


*Fig. 3.8 Facing angle scans for EEA inserted 3 cm from the wall with F=-.2 and 2 cm from the wall with F=0.*

the reversal parameter was $F$=-.20, and the pinch parameter was $\Theta$=1.9, making the field pitch angle $\vartheta = 6°$, consistent with the location of the centroid of the peak (9°) within the uncertainty in the position calibration of the probe (~3°). When the reversal parameter, $F$, was forced to zero (by opening the toroidal field circuit and preventing current from flowing in the TF coil/VCV) the EEA signal versus facing angle peak shifted to the poloidal direction as it must if the electrons are flowing along the equilibrium field. Note that while the uncertainty in aligning the EEA relative to the poloidal direction is about 3 degrees, the shift of the peak in Fig. 3.8 (6.3°+/- 1°) corresponds very accurately to the change in magnetic field pitch between the two cases. The full-width at half maximum (FWHM) of the peaks in Fig. 3.8 is 14°+/-1° roughly consistent with the full-width angular acceptance of the EEA (11°) as discussed in section 2.2.1.

The conclusion of the angle scan experiment is that the EEA detects electron flux flowing along the direction of the equilibrium magnetic field (within 3°), and detects net electron current flowing in the direction necessary to carry the edge poloidal current (with toroidal velocity component against the applied toroidal electric field).

The EEA cannot resolve misalignment of the electron flow direction relative to the magnetic field that is smaller than about 3°. It will be shown below that the detected electrons have parallel velocities greater than $10^6$ m/s, and given the edge plasma density and temperature have parallel mean free paths of several meters. The largest possible cross-field drift would come from a (radial) electric field of magnitude about 500 V/m (see section 4.7.3). The cross-field drift velocity resulting from this magnitude electric field is

$E_r/B_\theta < 10^4$ m/s making the misalignment of the electron flow and the magnetic field less than 1°, not resolvable with the EEA. It should be noted that the EEA is insensitive to the diamagnetic current which "flows" perpendicular to the magnetic field and provides an inward $\boldsymbol{J}\times\boldsymbol{B}$ force to balance the outward pressure gradient force. The diamagnetic current is a real current, but does not result from a real particle drift. As such, the EEA which detects ballistic electron flow cannot be used to measure the diamagnetic current.

3.2.2 Fast electron parallel distribution

Knowing now that $\vec{J}_e$ is parallel to $\vec{B}$, the EEA was aligned to the edge magnetic field (by performing the facing angle scan described above). The repeller bias voltage was changed in a shot-to-shot manner to explore the parallel velocity distribution of the fast electrons. Three raw signals are displayed in Fig.3.9 for three different bias cases. The average signal level falls at higher repeller bias as it should if the distribution has a relatively small drift velocity and a broad velocity distribution (high temperature). The distribution is to be contrasted with the electron beam case shown in Fig. 2.6 where the drift velocity was much higher than the velocity spread, and the EEA signal was flat until the repeller bias approached the beam energy (drift energy) and then fell very quickly.

The averaged signal (5 ms average) for many repeller bias cases is plotted versus repeller voltage in Fig. 3.10 for a series of nominally identical discharges at 220 kA. Current detected from both directions along the field is shown. The signal detected from the direction indicated by the larger of the two peaks in the facing angle scan (Fig. 3.7) will referred to as the "forward" electron

signal. The lesser peak signal will be referred to as the "backflow" electron signal. The forward and backflow electron populations may be treated as distinct populations each with an effective (undrifted) Maxwellian parallel velocity distribution, or more properly a half-Maxwellian distribution since each population consists of electrons flowing in one direction only. The dependence of the EEA signal on repeller bias for an undrifted Maxwellian is a simple exponential e-folding when the repeller bias increases by the effective temperature: $I_{EEA} \propto \exp(-V_r/T_{eff})$, (see section 2.2.2 for details). It is apparent from the difference in the slopes of the semi-log plot current vs. repeller voltage, that the backflow electrons have a significantly lower effective temperature. Fitting to exponentials gives $T_{forward}$=148 +/- 12 eV and $T_{back}$= 87 +/- 8 eV.

Treating the forward and backflow electron populations as distinct requires four parameters to describe the parallel distribution, two (effective) temperatures and two densities (or currents). Three parameters are required if the forward and backflowing populations are treated as positive and negative sides of a single drifted Maxwellian distribution: a temperature, a drift velocity, and a density. The fit to the data shown in Fig. 3.10 is a fit the expected EEA signal for a drifted Maxwellian (Eq. 2.4). The difference in slopes of the forward and backflowing distributions is a natural result of assuming a single drifted distribution, and there is *not* an independent parameter to adjust the ratio of the forward to backflow signals. The fit gives $T_{fast}$= 114 +/- 10 eV, $v_{drift}$= 2.1 +/- 0.1 x$10^6$ m/s. Recall that determination of the absolute fast electron density requires knowledge of the perpendicular temperature, so the third parameter is not meaningful at this point (see below). The superiority of the drifted fit over the half-Maxwellian (times 2) fits is partly an aesthetic one since both the

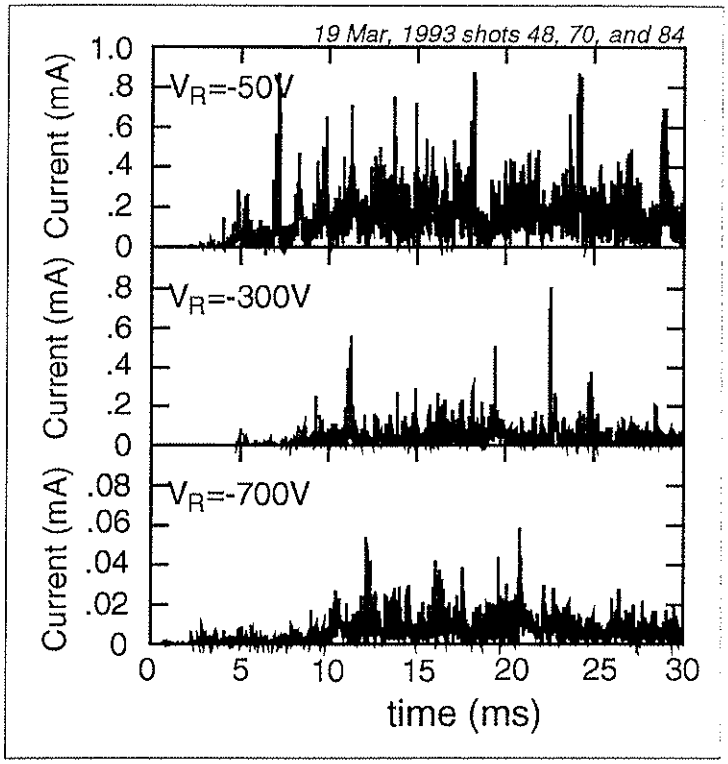


*Fig. 3.9 Typical EEA signals for three repeller bias cases. Note the change of scale in the bottom plot.*

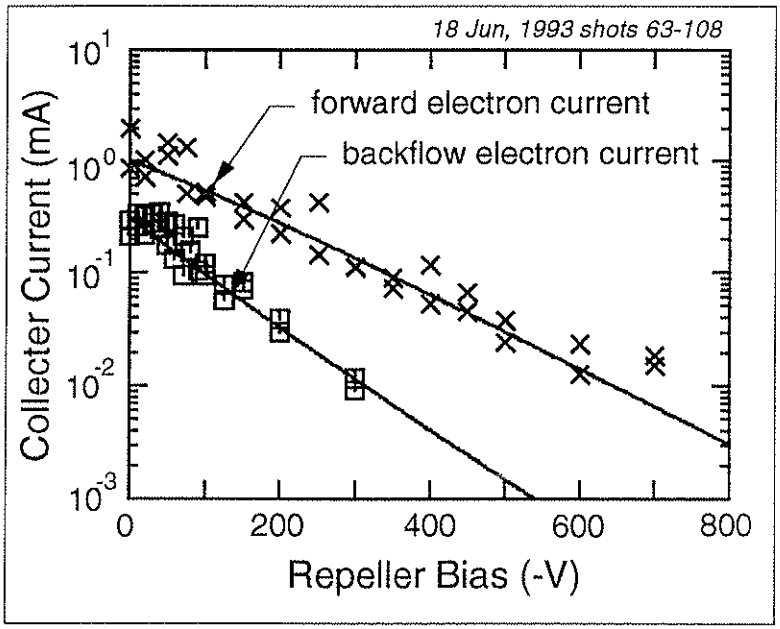


*Fig. 3.10 EEA repeller bias scan fit to a drifted Maxwellian distribution with T=114 eV and $E_{drift}$ =12 eV.*

forward and backflow signals represent the tails of a more populous distribution of electrons with a 20 eV temperature, i.e. the "bulk" distribution. However, the fast electron population is collisionally isolated from the bulk population, and as such can be treated independently. In addition, the fact that the distribution fits a drifted Maxwellian is not automatic. Whereas fitting to two half-Maxwellian distributions allows independent adjustment of the asymmetry and the effective temperature ratio, with a drifted-Maxwellian fit, the asymmetry and the difference in slope for the forward and backflowing signals are not independent. The fast electron population in MST fits a drifted-Maxwellian distribution for all parameter regimes tested.

The contours of $\chi^2 = \sum (I_{EEA} - I_{fit})^2 / \sigma^2$ for the drifted Maxwellian are plotted in Fig. 3.11 for three 2D slices through the 3D parameter space ($T_{fast}$, $E_{drift} = mv_{drift}^2/2$, and $n_{fast}$). The minima are well-defined. The fast electron temperature measurement is comparable to the central electron temperature measured by Thomson scattering of laser light off free electrons for these discharge conditions: $T_{eo} \approx 120$ eV.

### 3.2.3 Time resolved fast electron temperature

Given the high frequency or "spiky" nature of the fast electron current, the "instantaneous" identification of the time-averaged energy spectra to the fast electron distribution must be viewed with a grain of salt. The three channel EEA was employed with different bias potentials on each of the three repeller electrodes in order to resolve in time some measure of the fast electron distribution. Since the three channel EEA accepts electrons from one direction only, the measurement gives a time resolved estimate of $T_{forward}$. The spatial

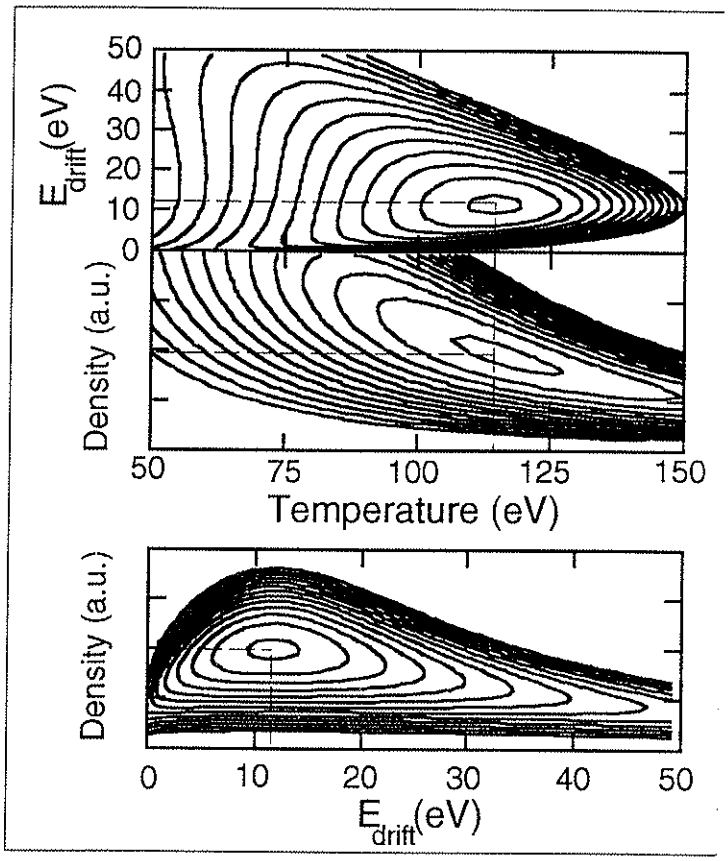


*Fig. 3.11 Contours of chi squared in three slices through the 3D parameter space corresponding to the fit of the EEA spectrum to a drifted Maxwellian distribution. The minima are well-defined for all three fit parameters.*

separation of the three measurements causes moderate decorrelation of the high frequency fluctuations (see section 4.6.3). The individual signals were smoothed (or lowpass filtered at ~20 kHz), and then averaged over 20 μs. The signals were then fit to an exponential $I_{EEA}(t) \propto \exp(-V_t/T_{forward}(t))$. A typical time evolution for the effective fast electron temperature is shown in Fig. 3.12. The fast electron temperature exhibits significant fluctuations (~20%), but on average agrees with fits to time averaged signals. An exponential fit to the data for the same shot after averaging from 14-19 ms gives a temperature $T_{forward}$=118 eV consistent with the average of the time resolved measurement. Two other features of the time resolved fast electron temperature are apparent from Fig. 3.12. First, the fast electron temperature exhibits a correlation with the discrete dynamo events or "sawteeth." Such a correlation is a robust characteristic of the time resolved fast electron temperature: the temperature drops significantly (~30-50%) at the crash time of the dynamo event. The second feature of interest in Fig. 3.12 is the absence of a correlation between the fast electron current or temperature with the ratio of the applied toroidal electric field to the critical electric field for runaway electrons. $E/E_c$ drops more than a factor of two in the time from 10 to 20 milliseconds, the time bracketing the time of peak plasma current. Each of the features pointed out in Fig. 3.12 is discussed now for a series of discharges averaged together.

Dynamo events are ubiquitous in MST and are identified by a sudden increase in the toroidal flux and an increase in the toroidal field reversal at the edge (Hokin, 1991; Beckstead, 1990). The influence of dynamo events on local plasma properties is evident in nearly all measurements. The toroidal flux increase is accompanied by a spike in the toroidal gap voltage ($V_{tg} = -d\Phi_t/dt$),

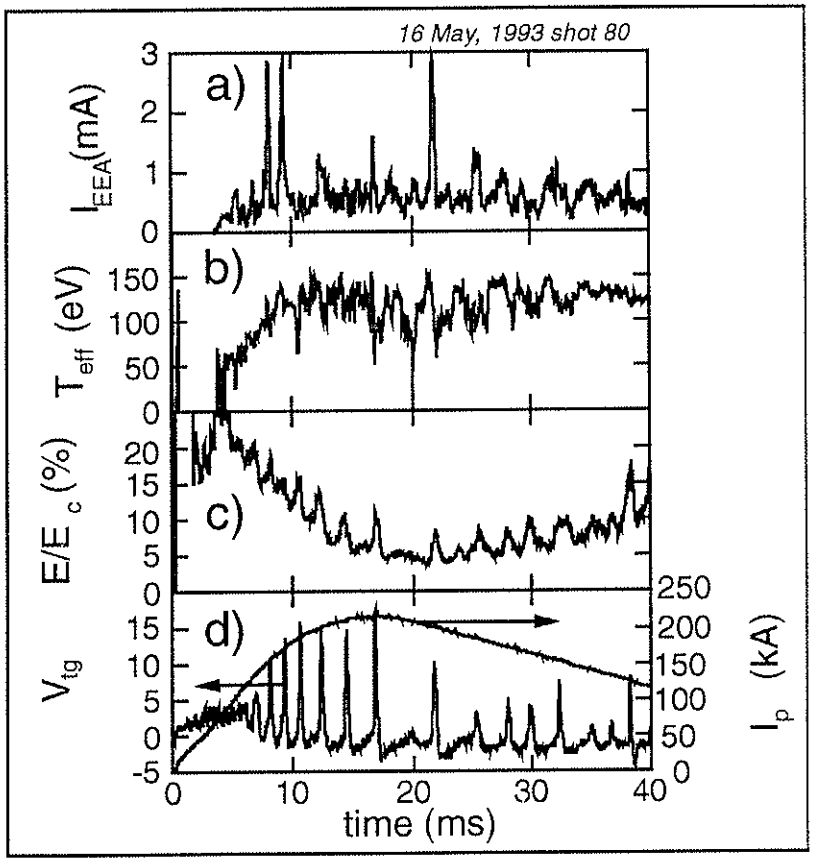


*Fig. 3.12 a) smoothed EEA signal, b) time resolved fast electron (effective, forward) temperature, c) the ratio of the applied toroidal electric field to the critical field for electorn runaway, and d) plasma current and toroidal gap voltage.*

and this spike serves as a good time reference for the dynamo event. The three channel EEA was employed with each repeller at a different bias level (-50 V, -170 V, and -300 V) for a series of 130 discharges. The signals were averaged at times relative to the peak time of the toroidal gap voltage (for dynamo events occuring between 10 and 20 ms). The results of that averaging over dynamo events is shown in Fig. 3.13. The qualitative impression that the fast electron temperature drops at a dynamo crash suggested by the time resolved temperature trace (Fig. 3.12) is shown to be reproducible. Prior to a dynamo event the fast electron temperature is rising for these discharge conditions from about 50 eV to about 100 eV ("heating phase"). The fast electron distribution begins cooling promptly with the crash and decays back towards the inter-crash level with a decay time of 0.25 +/- 0.05 ms. The dashed line in Fig. 3.13 indicates the fast electron temperature determined from only the two higher energy channels of the EEA. The small deviation of the two temperature measurements may indicate a deviation from the Maxwellian character of the distribution at higher energies. However, the onset of the cooling of the distribution is the same for both calculations indicating that the cooling is not simply due to a large increase in the cold electron density, but is a narrowing of the entire distribution out to energies greater than 300 eV. A possible interpretation of the fast electron temperature decay is that the fast electron heat source is momentarily "turned off" at the time of the dynamo event. If that is the case across the entire minor radius, then the decay time shown in Fig. 3.13 is a measure of the fast electron energy confinement time: $\tau_{E,fast} = 250 \pm 50\ \mu s$. This is an interesting result in light of the results reported in Chapter 4 on the magnetic fluctuation induced transport of electrons. An estimate of the global

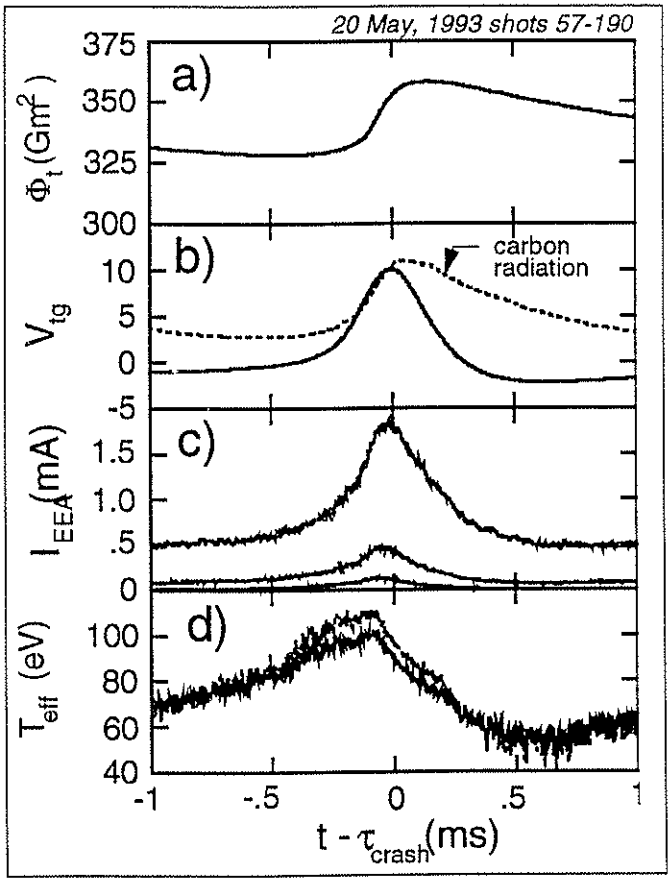


*Fig. 3.13 Signals averaged around the time of a discrete dynamo event: a) the toroidal flux, b) toroidal gap volts (solid) and carbon impurity radiation (dashed), c) EEA current in three with repeller bias at -50 V, -170 V, and -300 V, d) effective (forward) fast electron temperature.*

heat diffusivity for the fast electrons is found from $\chi_{e,fast} \approx a^2/(2\tau_{E,fast}) \approx 500\ m^2/s$. In Chapter 4 the fast electron particle diffusion coefficient is determined from the transport measurements and found to be about 500 $m^2s^{-1}$ also. In addition it will be shown that the magnetic fluctuation induced energy transport is convective, consistent with the statement that the particle diffusion and the heat diffusion are the same. The peaking of the electron current at or just after the dynamo crash is consistent with the observation of the peaking of the parallel current measured with a Rogowski probe at the crash time (Ji, 1994a).

The value of $E/E_c$ falls during the discharge as shown in Fig. 3.12. The same series of discharges used in the previous paragraph to resolve the average fast electron current and temperature during a dynamo event was also used to determine the dependence on $E/E_c$, by averaging not with respect to the dynamo crash but with respect to the discharge initiation. Since the dynamo events do not occur at the same time in each discharge (although they do occur in every discharge) the behavior exhibited in Fig. 3.13 and discussed above is averaged over in this analysis. The results of the averaging are shown in Fig. 3.14 for the times from 10 to 20 ms after the start of the discharge. The detected electron current shows a measurable drop of about 40% over this time period, but the fast electron temperature is extremely flat at 80 eV. The drop in the $E/E_c$ is more than 50% over the same time period. Also plotted in Fig. 3.14 is the time behavior of the calculated runaway electron source function (Eq. 3.1). Since the runaway source function is such a strong function of $E/E_c$, the calculated source dries up completely by about 17 ms into the discharge. The fact that the fast electron temperature is not correlated with the value of $E/E_c$,

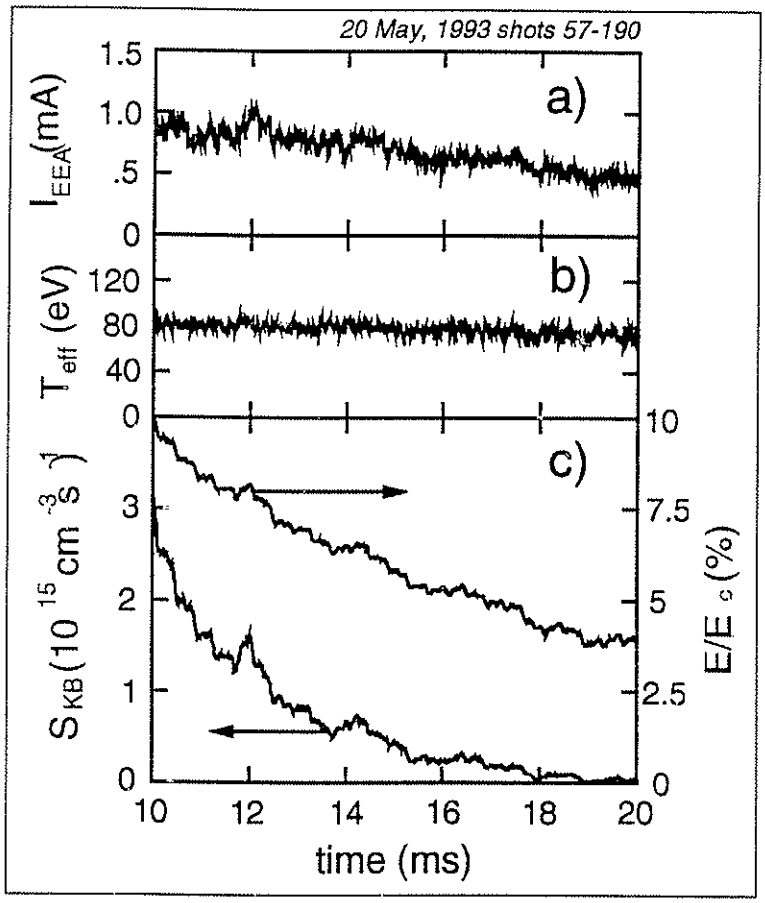


*Fig. 3.14 Shot averaged quantities during time around peak plasma current: a) EEA collecter current, b) Fast electron temperature, c) the ratio of the applied toroidal electric field to the ciritical electric field for runaways, and the Kruskal-Bernstein runaway electron source function.*

and that the fast electron current is relatively uncorrelated (compared to the predicted source rate change over the same time period), suggests that the applied toroidal electric field is not the critical parameter in fast electron generation.

### 3.2.4 Fast electron parallel heat flux

The thermocouple calorimeter probe was inserted to the same minor radius as the EEA above in similar discharge conditions. The rise in the temperature of the graphite slug after absorbing the fast electron heat flux for a single discharge is shown in Fig. 3.15a. The temperature rise $\Delta T_{graphite} = 26.5 \pm 0.5°C$ translates into an energy deposition of $\Delta E = 4.4 \pm 0.1\,J$. Time resolved measurements of the fast electron heat flux with a pyrobolometer probe indicate that the time behavior of the equilibrium heat flux roughly follows the time behavior of the toroidal plasma current (Fiksel, 1994b). Use of Eq. 2.19 is therefore justified to estimate the fast electron heat flux near the time of peak plasma current. Fig. 3.15b shows the equilibrium fast electron heat flux during the discharge that is consistent with the integrated energy deposition measured with the calorimeter. The peak value is about 1.7 kW/cm$^2$.

A modest variation of the toroidal plasma current (from 148 kA to 210 kA) and coincident variation of the line averaged plasma density (from $1.2 \times 10^{13}$ cm$^{-3}$ to $.82 \times 10^{13}$ cm$^{-3}$) allowed limited investigation of the dependence of the parallel electron heat flux on $I_\phi/N$, where $N = \int n 2\pi r dr \approx \bar{n}\pi a^2$ is the line density. The fast electron heat flux shows a clear increasing trend with $I_\phi/N$ (Fig. 3.16). The two shots at $1.5 \times 10^{-14}$ A-m are beyond the usual MST radiation

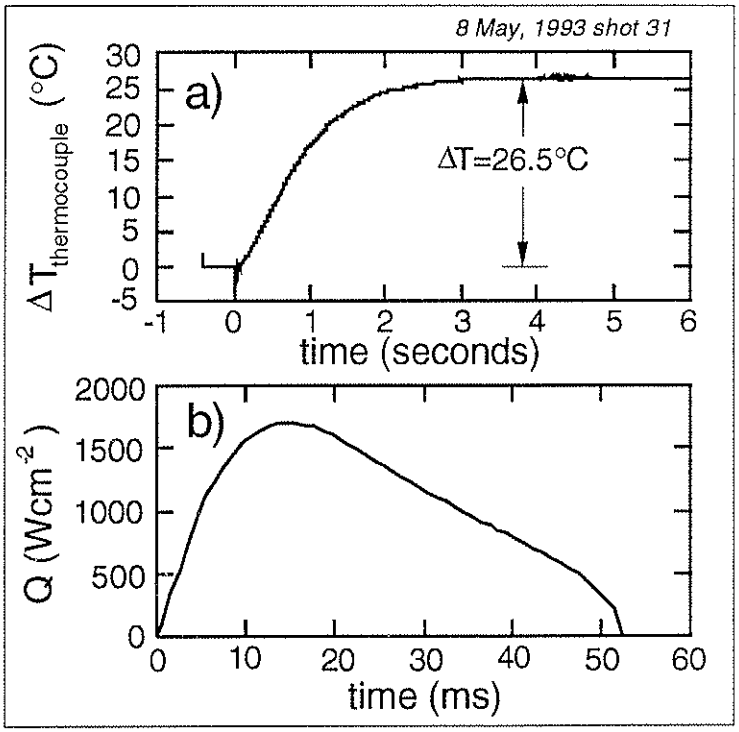


*Fig. 3.15 a) Temperature rise detected by the thermocouple in the calorimeter after a typical discharge. b) The fast electron heat flux calculated by assuming the time behavior of the plasma current.*

dominated density limit and are likely to have significantly different profiles than the other shots. $I_\phi/N$ is proportional to the average toroidal drift velocity of the core current carrying electrons. It is therefore not surprising that the thermal properties of the plasma exhibit a dependence on $I_\phi/N$ (Hokin, 1993).

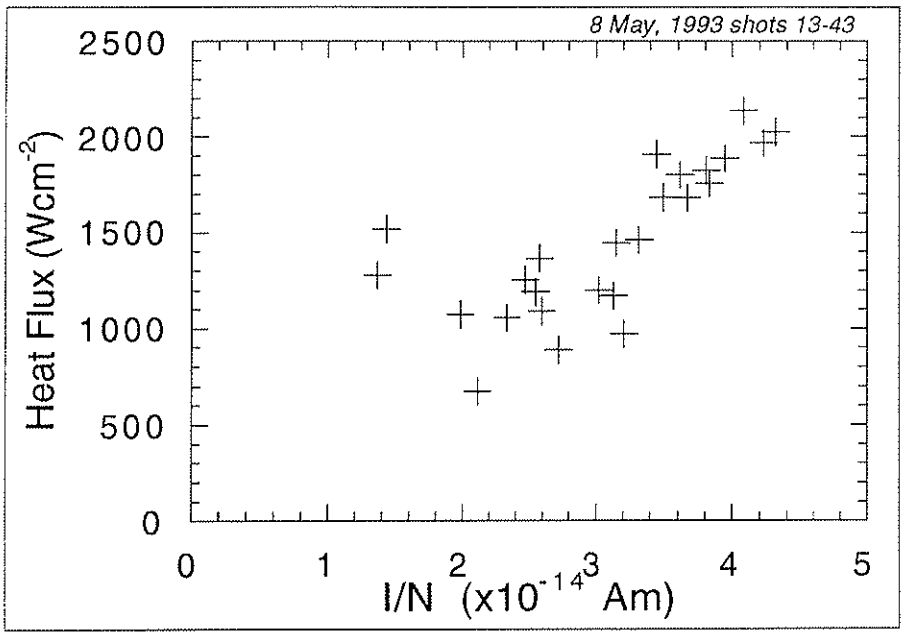


*Fig. 3.16 The fast electron heat flux measured with the thermocouple calorimeter as a function of I/N*

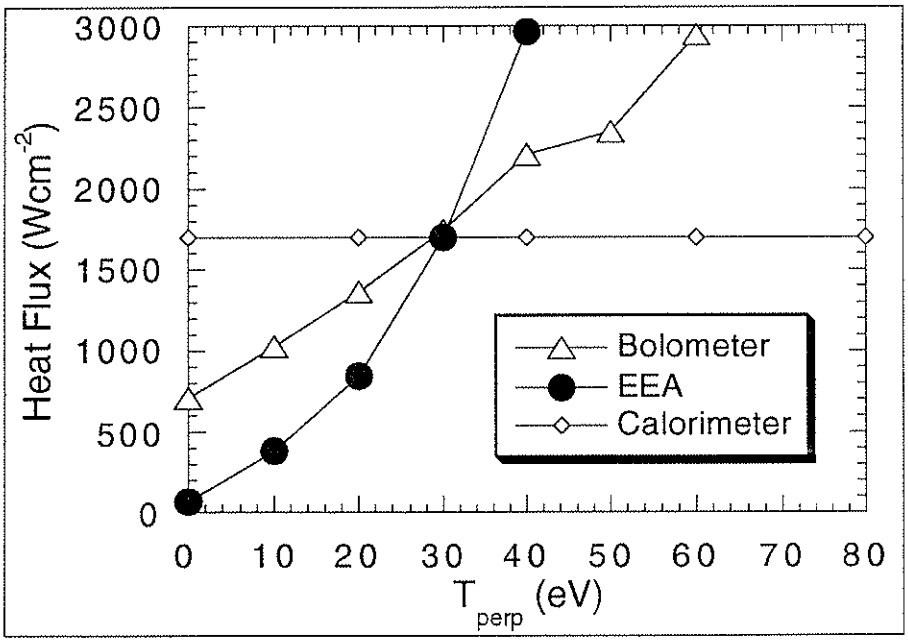


*Fig. 3.17 The fast electron heat flux measured with three diagnostics corrected for aperture transparency as a function of $T_{perp}$: 3.5 cm from the wall, $I_p$=210 kA.*

3.2.5 Cross-calibration of fast electron diagnostics and determination of the perpendicular temperature and current density

The heat flux carried by a drifted Maxwellian distribution is given by Eq. 2.15, rewritten here in terms of the current density carried by the distribution.

$$q_{\parallel} = \frac{J}{e}\left(\frac{3T_{\parallel}}{2} + T_{\perp} + \frac{mv_{drift}^2}{2}\right) \tag{3.8}$$

The calorimeter measurement allows determination of the transparency of the EEA aperture and hence the perpendicular temperature of the fast electron distribution. The calorimeter measurements were made for the forward flowing electrons only. If the forward fast electron distribution is approximated by a half-Maxwellian, the equation analogous to Eq. 3.8 is

$$q_{\parallel forward} = \frac{J_{+}^{EEA}}{\eta_{current}(T_{\perp})e}\left(T_{\parallel forward} + T_{\perp}\right) \tag{3.9}$$

where $J_{+}^{EEA}$ is the raw forward electron current density measured with the EEA ($I_{+}^{EEA}/\pi\delta^2$, $\delta$ is the aperture radius) and $\eta_{current}(T_{\perp})$ is the EEA aperture transparency calculated with the Monte Carlo code described in section 2.2.4. The forward fast electron heat flux calculated from Eq. 3.9 as a function of the possible perpendicular temperature values is plotted in Fig. 3.17 (solid circles), along with the forward heat flux measured with the calorimeter (open diamonds). Recall the calorimeter has a wide aperture (.3 cm diameter) and therefore has unit transparency. Also plotted in Fig. 3.17 is the forward heat flux

measured with the fast pyrobolometer (data courtesy of G. Fiksel) and corrected for its transparency (open triangles): $q_{\|forward} = q_{+}^{bolo}/\eta_{heat}(T_{\perp})$. There is excellent agreement among the three fast electron diagnostics at a value of $T_{\perp}$=30 +/- 5 eV. This is a surprising result since it is three times smaller than the parallel temperature. The implications of such a low fast electron perpendicular temperature are discussed below.

3.2.6 Fast electron current density

The transparency of the EEA aperture at $T_{\perp}$=30 eV is 6%. The absolute fast electron current density is determined from $J_{fast} = \left(J_{+}^{EEA} - J_{-}^{EEA}\right)/\eta(T_{\perp}) = 120 \pm 20$ kA/m$^2$. The fast electron current density matches the total parallel current density measured with magnetic probes (fork probe:Shen, 1992; Rogowski probe: Almagri, 1994). The fast electron density is $n_{fast} = J_{fast}/ev_{drift} = 4 \pm 1 \times 10^{11}$ cm$^{-3}$which is 10-20% of the bulk electron density measured with Langmuir probes (Ji, 1994b).

The results reported here are compared with results obtained on the ZT40-M RFP at Los Alamos National Laboratory (Ingraham, 1990). EEA measurements of the fast electron population in ZT-40M were modelled with a half-Maxwellian distribution that had an effective temperature greater than the central electron temperature. Results on MST indicate the fast electron distribution can be fit to a drifted Maxwellian distribution with a temperature comparable to $T_{eo}$. No discussion is given by Ingraham, *et al.*, about the nature of the backflowing fast electron popluation in ZT-40M, however Fig. 7 of their paper and an APS poster relating to the same work (Ingraham, 1989) indicate that the asymmetry in the electron current is about ten. Eq. 2.4 indicates that a

drift energy of about 80-100 eV is required to obtain an asymmetry factor of ten at the measured effective forward temperature of 360 eV reported from ZT40-M. If a drifted-Maxwellian fit had been made to that data, a fast electron temperature of about 250-300 eV would have been measured, closer to the central electron temperature of 200 eV. Calorimeter measurements of the fast electron heat flux were also obtained on ZT-40M. Agreement between the two measurements was found to correspond to a perpendicular fast electron temperature comparable to the parallel temperature. The method of calculating the EEA aperture transparency was not discussed by the authors, although in the concluding discussion, they mention that the finite length of the aperture was not taken into account and could affect the results for determining $T_\perp$. Careful calculation of the EEA transparency for the geometry used in MST and comparison with two other fast electron diagnostics makes the determination of $T_\perp$ more convincing. $T_\perp$ is much less than $T_\parallel$ for the fast electrons in MST. However, conclusions regarding the current carried by fast electrons in the two devices are similar. In MST, as was inferred for ZT-40M, the current carried by fast electrons is consistent with measurements of the total parallel current density measured with magnetic probes. The density fraction of fast electrons in MST is higher by a factor of two to five than in ZT-40M.

### 3.2.7 Density scan and dependence on $E/E_c$

The determination of the EEA transparency through cross-calibration with the two heat flux measurements allowed a complete characterization of the edge fast electron distribution, parameterized by the values of $T_\parallel, T_\perp, v_{drift}$, and $n$. The total current is related to the density and the drift velocity

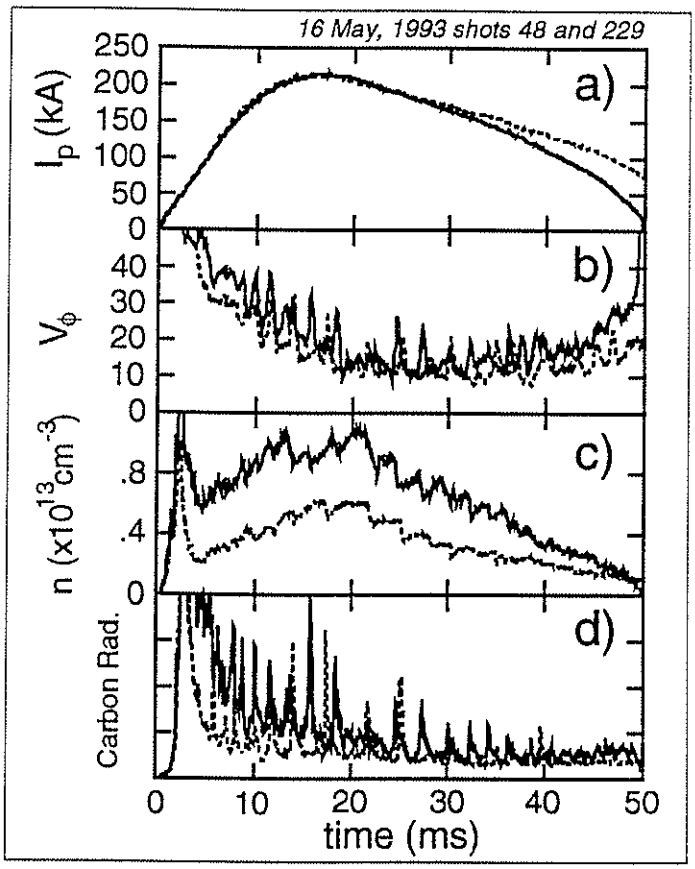


*Fig. 3.18 Typical signals from high (solid) and low (dashed) density discharges at constant plasma current. a) plasma current, b) toroidal voltage, c) line-averaged density, d) C III impurity radiation.*

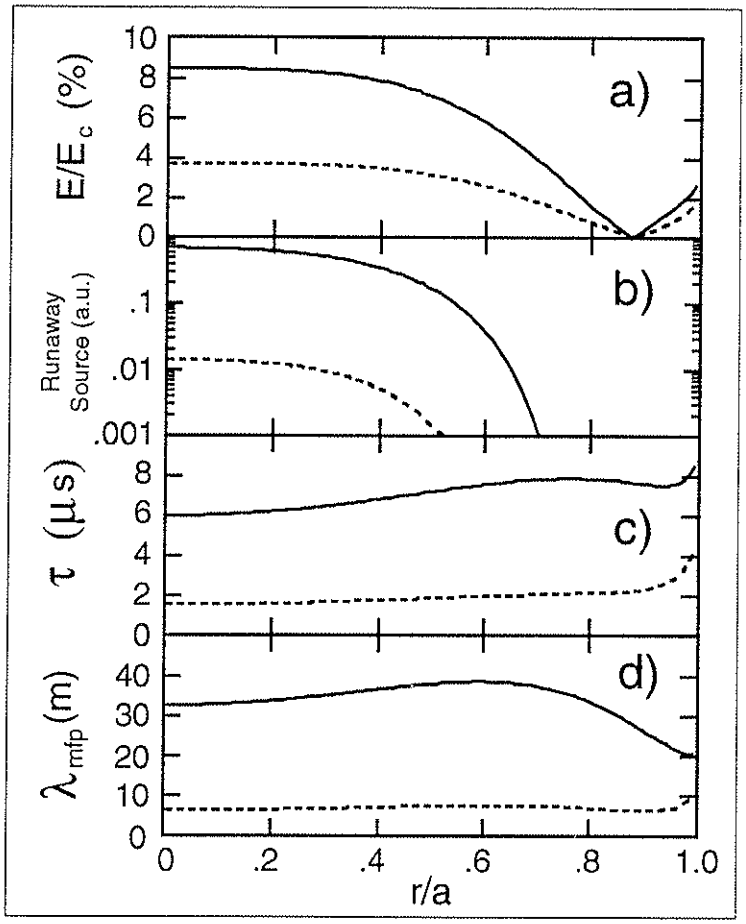


*Fig. 3.19 Model profiles of collisionality parameters for the low (solid) and high (dashed) density discharge conditions: a) the ratio of the applied toroidal electric field to the critical electric field for runaways, b) the runaway electron source function, c) the (thermal) electron collision time and d) mean free path length.*

through $J = nev_{drift}$. Measurements of the edge profiles of the fast electron distribution parameters were obtained in two plasma density conditions at the same plasma current: $I_p = 210$ kA. The "low" density case had a central chord averaged value of $0.58 \times 10^{13}$ cm$^{-3}$, and the "high" density case had a central chord averaged density of $1.0 \times 10^{13}$ cm$^{-3}$. The density was measured with the FIR laser interferometer; two typical traces for the central chord are shown in Fig. 3.18c, one for each discharge condition.

A density "scan" was chosen as a way to invesitgate the dependence of the fast electron distribution on the ratio $E/E_c$. The source of slide-away electrons depends sensitively on that ratio and changing the plasma density provides a controlled way of changing $E/E_c$. Fig. 3.18b shows typical toroidal voltage traces for the two discharge conditions used to calculate the applied electric field. The central electron temperature was measured by Thomson scattering (data courtesy of M. Cekic); the laser was fired at 18.5 ms. Discharge parameters were averaged from 14-19 ms and the results are tabulated in Table 3.1. The two discharge conditions should have significantly different *runaway* electron production rates, or in the presence of sufficient confinement degradation (i.e. stochastic magnetic field), significantly differently *fast electron* production rates.

The high and low density discharge conditions span a large range of collisionality. This is seen in Fig. 3.19, the profiles of several collisionality parameters are plotted using MPFM field profiles, a parabolic density profile and a flatter than parabolic temperature profile ( $T_e/T_{eo} = 1-(r/a)^4$). Of particular interest is the difference in the runaway electron source function magnitude for the two discharge conditions. The low density case is predicted

to produce about 50 times the number of runaway (or slideaway) electrons produced in the high density case.

| *16 May, 1993 shots 27-230* | High Density Case | Low Density Case |
|---|---|---|
| $I_{plasma}$ (kA) | 206 +/- 7 | 212 +/- 4 |
| n ($x10^{13}$ $cm^{-3}$) | 1.04 +/- 0.08 | 0.58 +/- 0.07 |
| $V_\phi$ (V) | 24 +/- 2 | 17 +/- 1 |
| $T_{eo}$ (eV) | 96 +/- 3 | 167 +/- 13 |
| I/N ($x10^{-14}$ A-m) | 3.5 +/- 0.5 | 7 +/- 1 |

***Table 3.1*** *Shot averages of discharge parameters for the density scan (14-19 ms).*

The measured fast electron profiles for the two density cases are shown in Figs. 3.20-3.24. The asymmetry between forward and backflow electrons exhibits a density dependence, increasing with lower density (Fig. 3.20). The fast electron temperature shows a significant dependence on density (or $E/E_c$) increasing almost 50% when the density decreases (Fig. 3.21). The local bulk electron temperature is shown for comparison. A similar increase in fast electron temperature versus $E/E_c$ was observed in ZT-40M, and taken as evidence for the KDT mechanism being operative. However, using absolute calibration of the EEA the fast electron density was measured for the two discharge conditions, and found to be relatively independent of plasma density or equivalently $E/E_c$ (Fig. 3.22), in fact, exhibiting perhaps a slightly higher fast electron density at higher plasma density (lower $E/E_c$). This is a significant result since the change in $E/E_c$ should result in a large change in the fast

electron production rate (Fig. 3.19). The global confinement properties of plasma are not believed to have changed significantly so a change in the fast electron production rate should result in a fast electron density change. Also shown in Fig. 3.22 is the bulk electron density measured with Langmuir probes for the high density case. At high density, the fast electron fraction is close to 20% across the region of the edge covered by this experiment. The fast electron current density profile at the edge also exhibits a relative independence of plasma density and is consistent with measurements of the total parallel current density at the edge using an insertable Rogowski probe (Fig. 3.23). The fast electron drift velocity profile is shown in Fig. 3.24.

*3.3 Conclusions regarding the fast electron generation mechanism*

EEA measurements in the ZT40-M reversed field pinch provided evidence that fast electrons carry the poloidal or dynamo current. The fast electrons were found to have an effective temperature greater than the central electron temperature. The high fast electron (parallel) temperature and scaling with the central electron temperature was taken as evidence for their acceleration in the core region, and thus as evidence for the kinetic dynamo mechanism. Measurements presented in this work show that the fast electron distribution in MST has a parallel temperature (~100 eV) comparable to the central electron temperature but not measurably greater. In addition the fast electron perpendicular temperature is much colder than the parallel temperature and is comparable to the edge bulk electron temperature of 20-30 eV. This single measurement creates serious difficulties for the kinetic dynamo

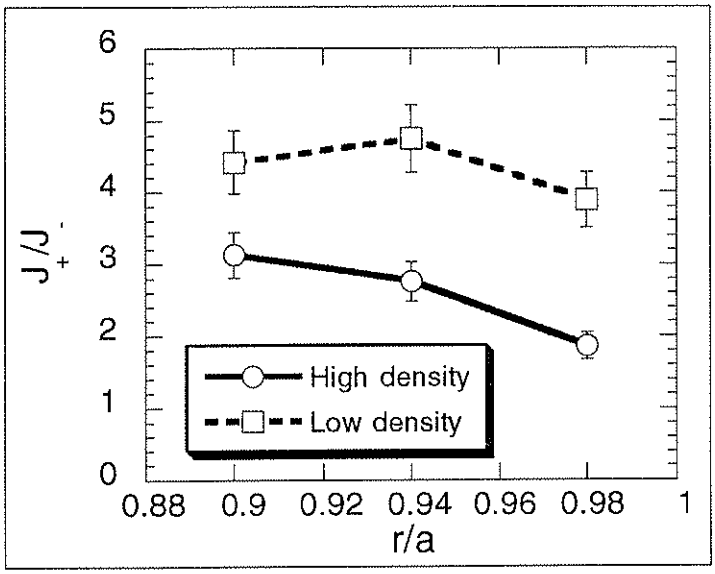


*Fig. 3.20 The asymmetry in the electron current for high and low density cases: $I_p$=210 kA*

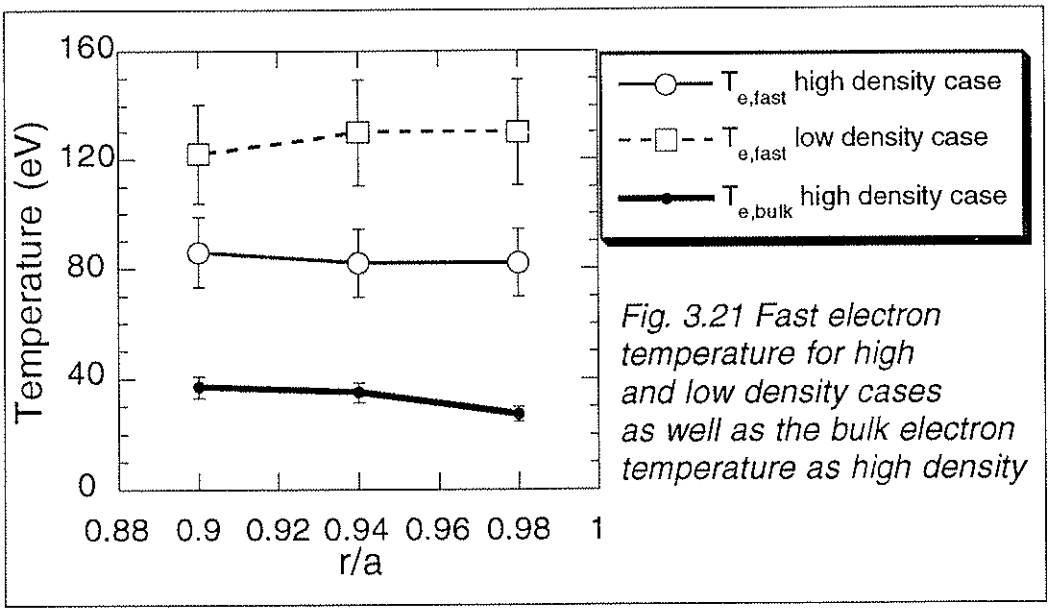


*Fig. 3.21 Fast electron temperature for high and low density cases as well as the bulk electron temperature as high density*

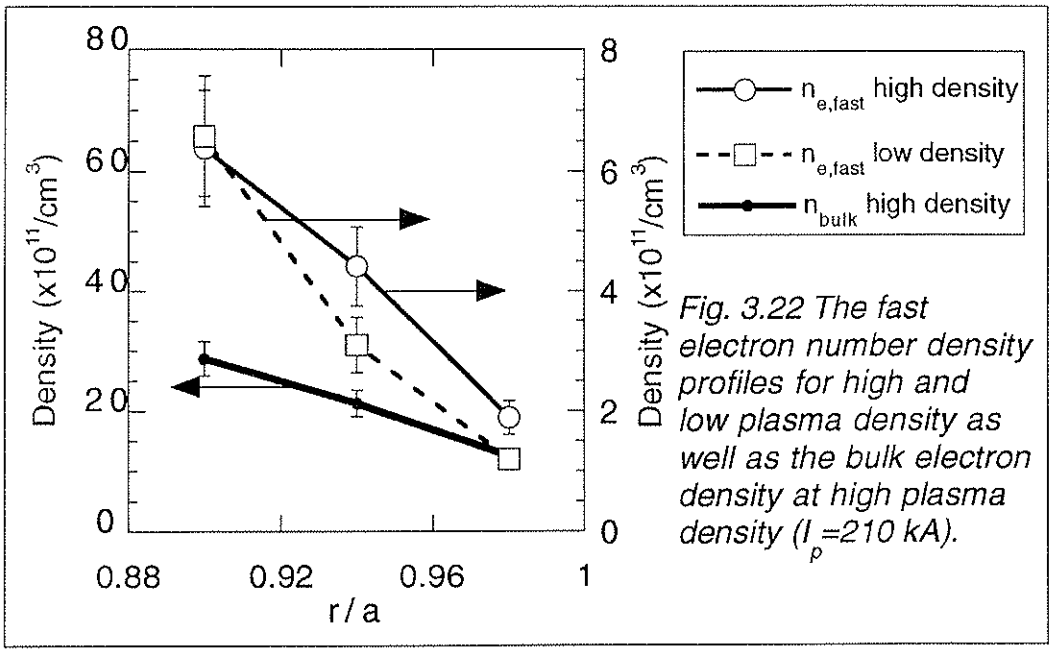


*Fig. 3.22 The fast electron number density profiles for high and low plasma density as well as the bulk electron density at high plasma density ($I_p$=210 kA).*

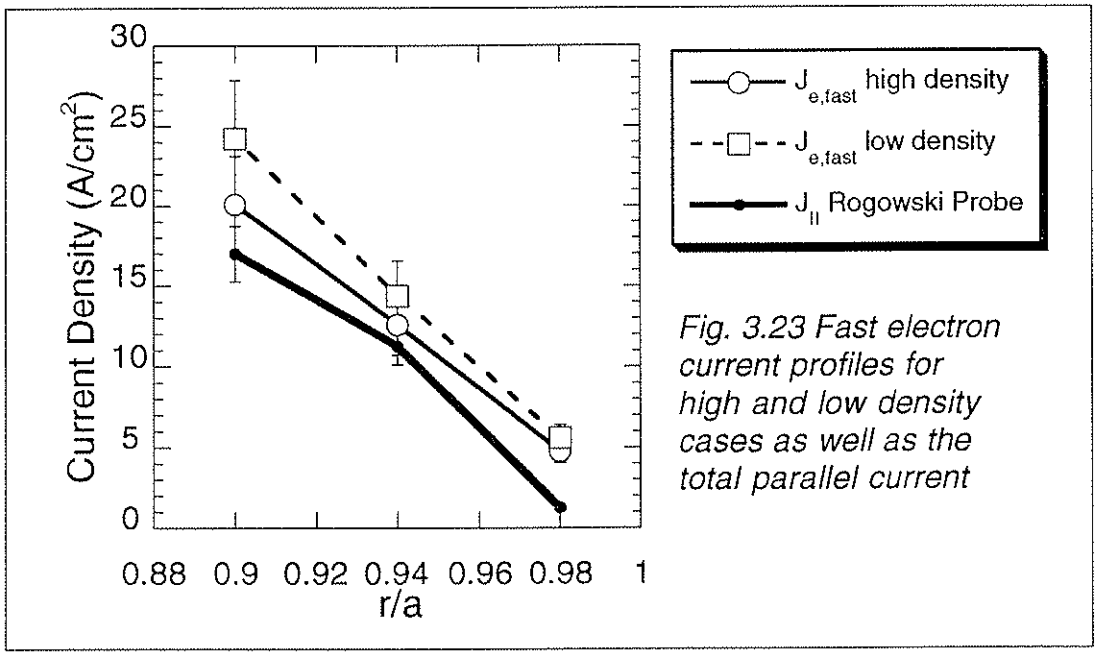


*Fig. 3.23 Fast electron current profiles for high and low density cases as well as the total parallel current*

mechanism in its original form. The consequences are discussed in this section.

The kinetic dynamo mechanism relies on the collisionless transport of core slide-away electrons through a pre-existing stochastic magnetic field. The energy distribution of edge fast electrons must therefore reflect the core distribution passed through the filter of the stochastic transport mechanism. The stochastic transport mechanism is discussed in significant detail in the next chapter (section 4.4). The stochastic diffusion mechanism is velocity dependent, but only depends on the component of velocity parallel to the magnetic field. There is no plausible, collisionless transport model that predicts the selective transport of low perpendicular velocity electrons. However, the magnetic moment of a collisionless electron is an adiabatic invariant of the motion: $\mu = mv_\perp^2/(2B)$. The magnetic field strength in the RFP falls about 50% between the center and the edge, meaning a collisionless fast electron born on the magnetic axis of the machine would lose half its perpendicular kinetic energy by the time it reached the edge. The edge fast electron distribution if produced by a kinetic dynamo mechanism would have a perpendicular temperature $T_\perp > T_{eo}/2 \approx 60$ eV, twice the measured perpendicular temperature.

The comparable magnitude of the local edge bulk electron temperature and the perpendicular temperature of the fast electrons suggests that the edge fast electrons are accelerated out of the edge bulk electron population by a local parallel (~poloidal) electric field, not transported from the core region., and this possibility is bolstered by the measurement of the fast electron diffusion coefficient and collisionality discussed below.

Further evidence that the kinetic dynamo mechanism is not operative in MST is provided by the comparison of low and high density fast electron distributions. Fast electrons are found to carry the total edge equilibrium parallel current density in MST at both high and low density (i.e. independent of $E/E_c$). This measurement implies that the mechanism that generates the edge fast electrons in MST is the dynamo mechanism. While the fast electron temperature is found to depend on plasma density and therefore on $E/E_c$, the fast electron density profile at the edge shows little dependence on density or $E/E_c$. The runaway electron source function for the parameters of the high and low density discharges in MST would indicate a large difference in the number of fast (slide-away) electrons produced in the two cases. There is no evidence that the global confinement properties of the plasma change significantly between the two cases. The density scan data therefore suggests that the kinetic dynamo mechanism is not operative in MST also.

The observation that the fast electron (average) temperature is constant and the fast electron current relatively constant during the discharge despite more than a 50% drop in $E/E_c$ between 10 and 20 ms adds to the mounting evidence that the KDT mechanism is not operative in MST.

A final piece of evidence against the kinetic dynamo in MST is provided by the results of the measurements of magnetic fluctuation induced fast electron transport. These measurements are the subject of Chapter 4 of this work, but the results will be revealed prematurely in order to support the current argument. The kinetic dynamo theory makes use of the heuristic theory of test particle (electron) transport in a stochastic field, the Rechester-Rosenbluth theory (Rechester, 1978). The transport of fast electrons in MST is found to

1990). The results reported here provide experimental evidence that the kinetic dynamo is not dominantly operative in MST.

A first order test of the fast electron generation mechanism proposed by Yoshida *et. al.,* (YHW, Yoshida, 1993) can be made for the high density discharge case reported above. In high density discharges, the bulk electron density and temperature profile at the edge of MST can be reliably measured with Langmuir probes. A comparison of the various velocities of interest at the edge is plotted in Fig. 3.25 (Langmuir probe measurements provided courtesy of H. Ji). While, the fast electron thermal velocity is significantly higher than the Alfvén velocity, the fast electron drift velocity and the bulk electron thermal velocity at the extreme edge of MST roughly match the Alfvén speed. At low density, the line averaged density is 56% of the high density case (Table 3.1). If the edge density drops by the same fraction, the edge Alfvén velocity would rise about 34%, qualitatively consistent with observed increase in the fast electron drift velocity at lower density. Moreover, the observed bulk density fluctuation level at the edge is 30-50% (Ji, 1994b) meaning the fluctuations in the Alfvén velocity are 60-100% because of the square root dependence on density. It is conceivable that the fluctuations in the Alfvén velocity could "thermalize" the fast electron distribution at the edge. The correlation is intriguing, but more detailed theoretical predictions are needed regarding the expected fast electron density and current driven by the Landau damping mechanism, as well as the asymmetry in the electron flux generated by such a mechanism. An additional difficulty arises for this mechanism further inside the plasma where the Alfvén velocity is significantly lower than all the characteristic velocities of the electron populations.

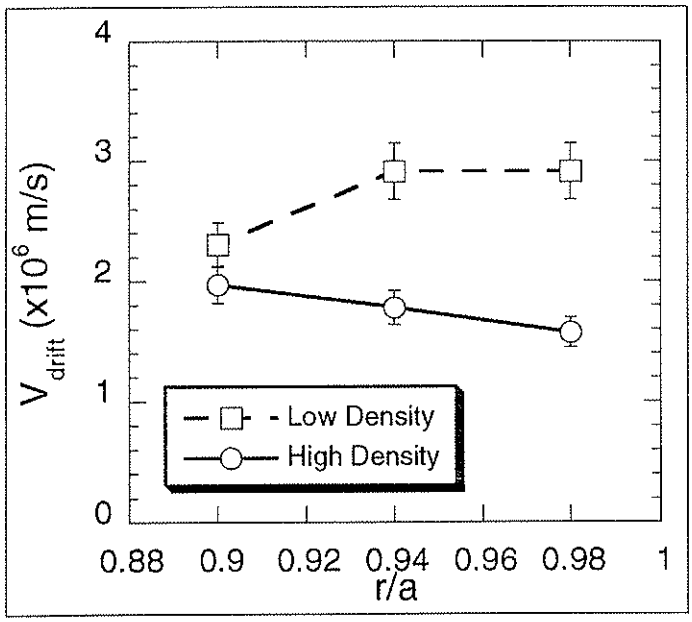


*Fig. 3.24 Drift velocity profiles for the fast electron distribution at high and low density: $I_p$=210 kA*

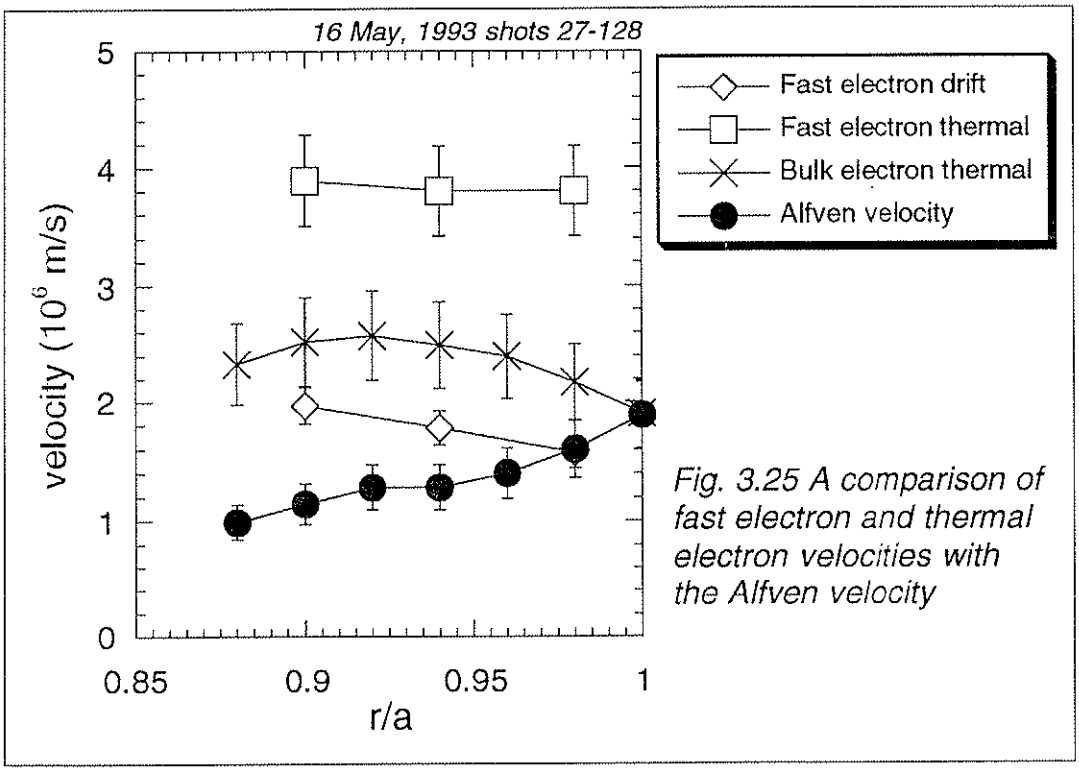


*Fig. 3.25 A comparison of fast electron and thermal electron velocities with the Alfven velocity*

The observation that all the parallel current in MST can be carried by the fast electron population presents difficulties for the heuristic reconnection model (Erba. 1993). The reconnection model predicts only ~10% of the mean current is carried by fast electrons, and that they have a ("thermal") velocity about 25 times the mean drift velocity. Th experiment shows a fast electron population carrying 100% of the current with a thermal velocity only 10-15 times the mean drift velocity. However the model is heuristic and its predictions are not quantitatively accurate.

A promising program of continued research into the fast electron generation mechanism in the RFP must include the effects of the dynamo electric field, the existence of which has been verified in MST (Ji, 1994a). Since, the electric field magnitude measured at the edge is greater than the applied toroidal electric field on axis, the effect on the edge electron population is not negligible.

## References

A. Almagri, private communication (1994).

J.A. Beckstead, "Sawteeth in the MST reversed field pinch," Ph. D. thesis, University of Wisconsin-Madison (1990).

H. Dreicer, "Electron and ion runaway in a fully ionized gas," Phys. Rev. **115**, 283 (1959).

M. Erba, P. Martin, S. Ortolani, and A. Rossi, "Magnetic reconnection as a mechanism for the generation of fast electrons," Nucl. Fusion **33**, 1577 (1993).

G. Fiksel, private communication (1994a).

G. Fiksel, S.C. Prager, W. Shen, and M. Stoneking, "Measurement of magnetic fluctuation induced energy transport," Phys. Rev. Lett. **72**, 1028 (1994b).

A.V. Gurevich, "On the theory of runaway electrons," Sov. Physics JETP, **12**, 904 (1961).

S. Hokin, A. Almagri, M. Cekic, B. Chapman, N. Crocker, D.J. Den Hartog, G. Fiksel, J. Henry, H. Ji, S. Prager, J. Sarff, E. Scime, W. Shen, M. Stoneking, and C. Watts, "Reversed-field pinch studies in the Madison Symmetric Torus," J. of Fusion Energy **12**, 281 (1993).

S.A. Hokin, A. Almagri, S. Assadi, M. Cekic, B. Chapman, G. Chartas, N. Crocker, M. Cudzinovic, D.J. Den Hartog, R. Dexter, G. Fiksel, R. Fonck, J. Henry, D. Holly, S. Prager, T. Rempel, J. Sarff, E. Scime, W. Shen, J. Sprott, M. Stoneking, and C. Watts, "Anomalous ion heating and superthermal electrons in the MST reversed-field pinch," in *Proceedings of the 14th Int. Conf. on Plasma Physics and Controlled Nuclear Fusion*, Wurzburg (1992) page 539.

S. Hokin, A. Almagri, J. Beckstead, G. Chartas, N. Crocker, M. Cudzinovic, D.J. Den Hartog, R. Dexter, D. Holly, S. Prager, T. Rempel, J. Sarff, E. Scime, W. Shen, C. Spragins, C. Sprott, G. Starr, M. Stoneking, C. Watts, and R. Nebel, "Global confinement and discrete dynamo activity in the MST reversed-field pinch," Phys. Fluids B **3**, 2241 (1991).

J.C. Ingraham, R.F. Ellis, J.N. Downing, C.P. Munson, P.G. Weber, and G.A. Wurden, "Energetic electron measurements in the edge of a reversed-field pinch," Phys. Fluids B **2**, 143 (1990).

J.C. Ingraham, R.F. Ellis, J.N. Downing, G. Miller, C.P. Munson, M.M. Pickrell, K.F. Schoenberg, P.G. Weber, and G.A. Wurden, "Further fast electron studies in the ZT-40M reversed field pinch edge plasma," Bull. Am. Phys. Soc. **34**, 2105 (1989).

A.R. Jacobson and R.W. Moses, "Sustainment dynamo reexamined: nonlocal electrical conductivity of a plasma in a stochastic magnetic field," Phys. Rev. Lett. **52**, 2041 (1984a).

A.R. Jacobson and R.W. Moses, "Nonlocal dc electrical conductivity of a Lorentz plasma in a stochastic magnetic field," Phys. Rev. A **29**, 3335 (1984b).

H. Ji, A.F. Almagri, S.C. Prager, and J.S. Sarff, "Time-resolved observation of discrete and continuous MHD dynamo in the reversed-field pinch edge," submitted to Phys. Rev. Lett. (1994a).

H. Ji, private communication (1994b).

H. Knoepfel and D.A. Spong, "Runaway electrons in toroidal devices," Nucl. Fusion **19**, 785 (1979).

M.D. Kruskal and I.B. Bernstein, "Runaway electrons in an ideal Lorentz plasma," Phys. Fluids **7**, 407 (1964).

E.N. Parker, Astrophys. J. Suppl. Ser. **8**, 177 (1967).

A.B. Rechester and M.N. Rosenbluth, "Electron heat transport in a tokamak with destroyed magnetic surfaces," Phys. Rev. Lett. **40**, 38 (1978).

D.D. Schnack, E.J. Caramana, and R.A. Nebel, "Three-dimensional magnetohydrodynamic studies of the reversed-field pinch," Phys. Fluids **28**, 321 (1985).

K.F. Schoenberg and R.W. Moses, "Magnetic turbulent electron transport in the reversed-field pinch," Phys. Fluids B **3** (1991).

W. Shen, R.N. Dexter, and S.C. Prager, "Current-density fluctuations and ambipolarity of transport," Phys. Rev. Lett. **68**, 1319 (1992).

W. Shen and J.C. Sprott, "Modified polynomial function model for reversed-field pinches," Phys. Fluids B **3**, 1225 (1991).

J.B. Taylor, "Relaxation of toroidal plasma and generation of reverse magnetic fields," Phys. Rev. Lett. **33**, 1139 (1974).

P.W. Terry and P.H. Diamond, "A self-consistent theory of radial transport of field-aligned current by microturbulence," Phys. Fluids B **2**, 1128 (1990).

Z. Yoshida, A. Hasegawa, and M. Wakatani, "Production of superthermal electrons and ion cyclotron waves in a reversed-field-pinch plasma," Phys. Fluids B **5**, 3261 (1993).

# 4. Electron Transport Due to Turbulent Magnetic Fluctuations

## *4.1 Evidence for anomalous transport in the RFP*

### 4.1.1 Classical particle diffusion

It is observed that plasma particles and energy diffuse across a confining magnetic field despite the fact that a single charged particle would gyrate about such a field indefinitely. Even a collection of identical charged particles is in principle perfectly confined, because like particle collisions merely result in the exchange of guiding center positions. This effect is used in nonneutral plasma confinement devices and particle traps (e.g. Penning traps) to hold a large number of charged particles for very long times. The story is different in a neutral plasma consisting of electrons and positive ions. Coulomb collisions between particles of different species cause net particle transport across the confining field. Transport resulting from Coulomb collisions is referred to as "classical." Unlike neutral atom collisions which are essentially "billiard ball" type collisions, collisions between charged plasma particles are dominated by small angle deflections under the influence of the long range Coulomb force. An effective collision frequency is defined by calculating the time for an average particle to be deflected by 90°:

$$\nu_e = 2.91x10^{-6} n \ln\Lambda / T_e^{3/2} \text{ sec}^{-1}. \qquad (4.1)$$

Eq. 4.1 is the electron collision frequency for density $n$ in $cm^{-3}$ and electron temperature $T_e$ in eV. The particle flux perpendicular to the magnetic field due

to Coulomb collisions is proportional to the particle density gradient, i.e. it obeys Fick's Law,

$$\Gamma = -D\nabla n. \tag{4.2}$$

$\Gamma$ is the particle flux, $D$ is the diffusion coefficient, and $n$ is the particle density. Classical diffusion is ambipolar, electrons and ions are transported at the same rate, and is given by

$$D_{Classical} \approx {\nu_e \nu_{th,e}^{\,2}} \Big/ {\omega_{c,e}^{\,2}}, \tag{4.3}$$

where the thermal speed is $v_{th} = \sqrt{2kT/m}$ and the cyclotron frequency is $\omega_c = qB/m$. For typical MST plasma conditions ($T$=100 eV and $B$=900 G) the classical diffusion coefficient is $D$ ~ 0.03 $m^2/s$. An experimentally determined value for the diffusion coefficient is found by measuring the plasma density profile and the ionization source profile (from the $H_\alpha$ radiation profile) and solving the steady state particle transport equation for $D$ assuming it is constant over the minor radius

$$\nabla \cdot \left( D\nabla n - n v_p \right) = S_{ion}, \tag{4.4}$$

where $v_p = E_\varphi B_\theta / B^2$ is the pinch velocity and $E_\phi$ is the applied toroidal electric field. This analysis has been performed for a variety of MST discharge conditions (Hokin, 1989) and the resulting diffusion coefficient is generally

about 50 $m^2/s$. Because the measured transport rate is three orders of magnitude larger than the classical rate, the transport is called "anomalous."

4.1.2 Classical heat diffusion

The thermal diffusivity, $\chi$, is defined in terms of the total heat flux $Q$, the particle diffusion coefficient and the density and temperature gradients as follows:

$$Q = n\chi\nabla T + \frac{3}{2}TD\nabla n. \tag{4.5}$$

The first term in eq. 4.5 is the *conductive* heat flux and the second term is the *convective* heat flux. Whereas like particle collisions cannot cause plasma particle transport, like particle collisions can cause (classical) energy or heat transport. Ion-ion collisions therefore dominate the heat transport due to their large gyro-radii, and the heat flux is dominated by the conductive term with the classical thermal diffusivity given by

$$\chi_{Classical} \approx \nu_i v_{th,i}^2 / \omega_{c,i}^2 \approx \sqrt{\frac{m_i}{m_e}} D_{Classical}. \tag{4.6}$$

For MST plasma conditions $\chi_{Classical} \sim 1\ m^2/s$. Classical energy confinement is much worse than classical particle confinement. The heat is conducted out rather than being carried out by particle transport. Experimentally, the heat diffusivity is found by measuring the density and

temperature profiles, solving the particle transport equation to get $D$ and then solving the steady state energy transport equation

$$\nabla \cdot \left( n\chi \nabla T + \frac{3}{2} TD\nabla n \right) = \eta j^2 - \mathcal{P}_{rad} - \mathcal{P}_{cx}. \tag{4.7}$$

The right side of eq. 4.7 is the Ohmic heating power density minus the radiated and charge exchange power densities, $\eta$ is the plasma resistivity and $j$ is the current density. In practice, only the central value of the electron temperature is measured, so a global effective diffusivity is estimated by assuming parabolic profiles in density and temperature. While the convective term in eq. 4.7 is experimentally found to be large enough to account for the observed energy transport, it is customary to define a global effective heat diffusivity as $\chi_{eff} = a^2/2\tau_E$ where the (transport) energy confinement time is estimated from

$$\tau_E \approx \frac{3/2\, \bar{n}(T_{eo} + T_{io})(2\pi^2 a^2 R)}{P_{ohmic} - P_{rad}}, \tag{4.8}$$

whether or not the transport is conductive. $P_{Ohmic} = I_p V_{loop}$ is the Ohmic input power and $P_{rad}$ is the total power radiated from the plasma. The energy confinement time in MST is generally about 1 ms, and the effective heat diffusivity is about 100 $m^2/s$. It is therefore apparent that the energy transport in MST is anomalous also, though by only two orders of magnitude compared with three for the particle transport. In addition, the effective diffusivity is comparable to the global particle diffusion coefficient indicating that the energy transport is

probably dominated by convective energy transport, energy carried out by the transported particles.

It should be noted that comparing classical and anomalous transport for the same plasma conditions is a bit misleading. If MST had classical transport coefficients, the equilibrium density and more importantly the temperature would be higher and the classical transport coefficients would be even smaller than the numbers quoted above.

There is a great deal of physics buried in the global transport quantities $D$ and $\chi_{eff}$ (or equivalently the particle and energy confinement times, $\tau_p$ and $\tau_E$). In particular the electron and ion species may have vastly different transport properties due to their great difference in mass. Classically, the Ohmic heating goes directly to the high mobility electrons. Energy is then transferred collisionally to the ions on the equilibration time scale $\tau_{eq} \approx m_i/(m_e \nu_e)$. Classically, ion conductive heat transport dominates all other energy loss channels. In MST (as in other RFP devices) the ion temperature is comparable to and sometimes greater than the electron temperature (Scime, 1992) which is not explained by Coulomb processes. This observation has been labelled "anomalous ion heating." In fact, in MST the ion-electron equilibration time is about 5 ms, longer than the measured energy confinement time (~1 ms), so care must be taken to understand the energy flow and transport in terms of the individual species in the RFP.

*4.2 Turbulent plasma transport*

It is not surprising that the transport in MST is much worse than classical since every other magnetic confinement device in the world also observes anomalous transport. The clear suspect for the cause of anomalous transport in all devices is the presence of turbulent fluctuations. Turbulent transport has been reviewed by P.C. Liewer (Liewer, 1985) and A.J. Wootton, *et al.* (Wootton, 1990). Radial particle transport occurs in the presence of turbulent fluctuations if the fluctuations in the local particle number density are correlated with a radial velocity fluctuation and if the correlation has a statistically significant phase relation over a magnetic flux surface. More correctly, the flux is found from

$$\Gamma_r = \left\langle \int \tilde{f}(\mathrm{v})\tilde{v}_r(\mathrm{v})d\mathrm{v} \right\rangle, \tag{4.9}$$

where the brackets indicate that the product is averaged over a flux surface. There are two likely candidates for the fluctuating radial velocity responsible for particle transport: 1) $\tilde{v}_r = \tilde{E}_\perp / B_o$ is the fluctuating ExB drift where $\tilde{E}_\perp$ is the fluctuating electric field perpendicular (in the flux surface) to the local equilibrium magnetic field $B_O$, and 2) $\tilde{v}_r = v_\parallel \tilde{B}_r / B_o$ is a fluctuating radial velocity due to parallel streaming along a radially fluctuating magnetic field. Assuming these are the dominant turbulent transport mechanisms, eq. 4.9 can be rewritten as

$$\Gamma_{r,\alpha} = \frac{\left\langle \tilde{n}_\alpha \tilde{E}_\perp \right\rangle}{B_o} + \frac{\left\langle \tilde{J}_{\parallel,\alpha} \tilde{B}_r \right\rangle}{q_\alpha B_o}. \tag{4.10}$$

The first term in eq. 4.10 is referred to as the electrostatic particle transport term (because electrostatic $E$-field fluctuations ($\tilde{E}_{ES} = -ik_\perp \tilde{\phi}$) dominate the electromagnetic $E$-field fluctuations ($\tilde{E}_{EM} = -\partial \tilde{A}_\perp / \partial t$) in most experiments), and the second term is called the magnetic transport term. Since the ExB drift is the same for ions and electrons, the electrostatic transport term is ambipolar (for turbulence wavelengths long compared to the ion gyro-radius). It is not clear *a priori* that the magnetic particle transport term need be ambipolar, although steady state particle transport must be ambipolar to prevent continuous charging of the plasma. The issue of the ambipolarity of magnetic transport will be taken up in section 4.4.2.

The energy transport associated with the electrostatic and magnetic fluctuations is

$$Q_{r,\alpha} = \frac{3}{2}\frac{\left\langle \tilde{p}_\alpha \tilde{E}_\perp \right\rangle}{B_o} + \frac{\left\langle \tilde{q}_{\parallel,\alpha} \tilde{B}_r \right\rangle}{B_o}, \tag{4.11}$$

where $\tilde{p}$ is the fluctuating pressure and $\tilde{q}_\parallel$ is the fluctuating parallel heat flux. Both terms in eq. 4.11 can be broken up into conductive and convective parts respectively,

$$Q_{r,\alpha} = \frac{3}{2} n_\alpha \frac{\left\langle \tilde{T}_\alpha \tilde{E}_\perp \right\rangle}{B_o} + \frac{3}{2} T_\alpha \frac{\left\langle \tilde{n}_\alpha \tilde{E}_\perp \right\rangle}{B_o} + \frac{3}{2} J_{\parallel,\alpha} \frac{\left\langle \tilde{T}_\alpha \tilde{B}_r \right\rangle}{q_\alpha B_o} + \frac{3}{2} T_\alpha \frac{\left\langle \tilde{J}_{\parallel,\alpha} \tilde{B}_r \right\rangle}{q_\alpha B_o}. \tag{4.12}$$

Electrostatic particle and energy transport has been measured at the edge of the octupole (Schmidt, 1970), stellarator (Uckan, 1990), tokamak

(Rowan, 1987) as well as the RFP (Rempel, 1991; Ji, 1991). The electrostatic particle transport at the edge of MST (r/a>.85) was found to be large enough to account for all of the expected particle losses, while the electrostatic energy transport was not large enough to account for the total energy losses at the edge (Rempel, 1991). The mechanism responsible for the electrostatic fluctuations in the edge of the MST plasma and in other devices is an as yet unidentified micro-instability, perhaps the resistive interchange (or g-) mode. The wavenumber spectra of electrostatic fluctuations is broader than magnetic fluctuation spectra indicating the localized (short wavelength) nature of the turbulence.

Previous to this work, the magnetic transport of particles and energy had been investigated in three ways:

1) Runaway electrons provide an excellent probe of magnetic fluctuations because their high velocities (v~c) isolate them from collisional transport mechanisms and make them susceptible to the imperfections in the magnetic field structure (i.e. stochasticity). Barnes and Strachan (Barnes, 1982; Barnes, 1983) measured the hard x-ray radiation emitted from the limiter of the PLT tokamak at Princeton University. Such high energy radiation can only come from the *Bremsstrahlung* emitted by MeV runaway electrons as they decelerate through the hard target of the limiter material. The fluctuations in the x-ray flux correlate with PLT sawtooth activity as well as vertical field controlled plasma position shifts, and the transport properties of the runaway electrons were inferred from the delay in the x-ray flux changes. Catto *et al.*, (Catto, 1991) employed a similar technique at the University of Texas on the TEXT tokamak to measure the runaway electron diffusion coefficient.

2) Zurro *et al.* (Zurro, 1993), measured radial ion velocity fluctuations by spectroscopic means in the TJ-1 tokamak of Madrid. By invoking theoretical predictions of energy equipartition between flow fluctuations ($E_k = \rho\tilde{v}^2/2$) and magnetic fluctuations ($E_M = \tilde{B}^2/2\mu_o$) the core magnetic fluctuation level was inferred. The inferred magnetic fluctuation level was large enough to make the field stochastic throughout much of the core of the tokamak and to therefore account for the observed anomalous electron heat transport (by the Rechester-Rosenbluth mechanism detailed below).

3) Previous investigation of magnetic particle transport in MST was made by Shen *et al.* (Shen, 1992). Shen measured the correlation of the total current fluctuations (by means of a multi-coil insertable probe) with the radial magnetic field fluctuations. The measurement yielded the non-ambipolar particle flux due to magnetic fluctuations

$$\Gamma_{q,mag} = \frac{\left\langle \tilde{J}_{\parallel,total}\tilde{B}_r \right\rangle}{eB_o} = \frac{\left\langle \tilde{J}_{\parallel,i}\tilde{B}_r \right\rangle}{eB_o} + \frac{\left\langle \tilde{J}_{\parallel,e}\tilde{B}_r \right\rangle}{eB_o}. \qquad (4.13)$$

The magnetic fluctuation induced particle transport was found to be ambipolar; the non-ambipolar particle flux being less than 5% of the total particle flux at the edge.

### *4.3 Magnetic fluctuations in MST*

The reversed field pinch configuration, while it has many attractive features from a plasma confinement and eventual fusion reactor point of view

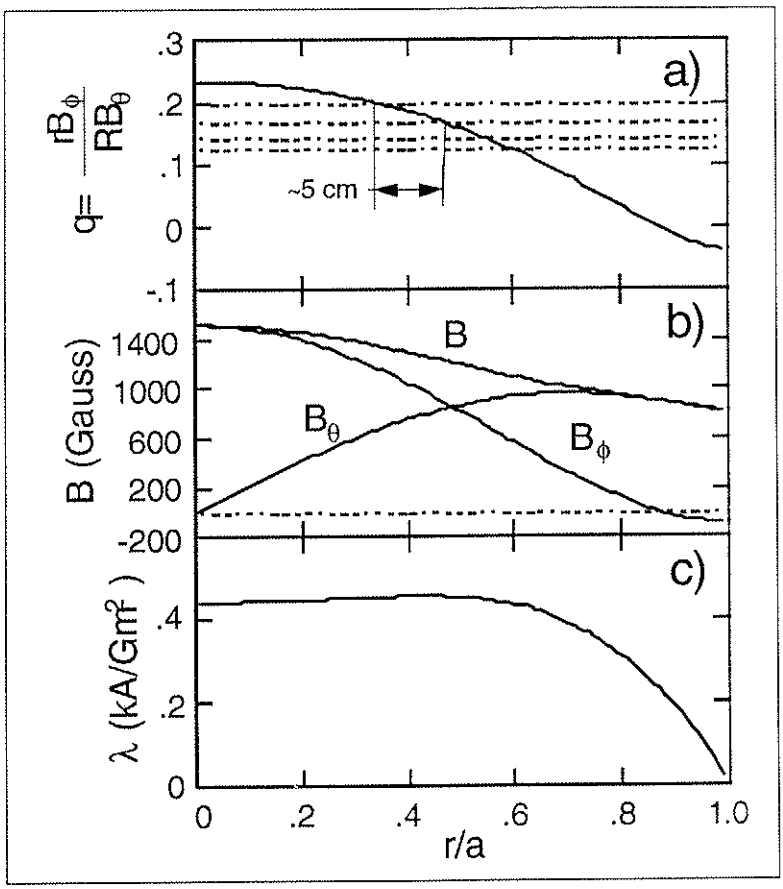


*Fig. 4.1 Modified polynomial function model profiles of a) safety factor (dashed lines indicate low order rational surfaces), b) magnetic field components, and c) the normalized parallel current density.*

such as high magnetic shear to stabilize pressure driven instabilities, low magnetic field strength at the coils, and high Ohmic heating efficiency, also introduces a series of rational $q$-surfaces ($q = rB_\phi/RB_\theta$) by virtue of its high shear. Fig. 4.1 shows a model (MPFM: Shen, 1991) equilibrium $q$ profile for a RFP with aspect ratio R/a=3 such as MST. The lowest order rational surfaces are the $q$=1/5,1/6, 1/7, and 1/8, with an accumulating series of higher order surfaces out to the reversal surface ($q = 1/\infty$) with a high order descending

series of negative $q$ surfaces outside the reversal surface. The model magnetic and normalized parallel current density ($\lambda = \vec{J} \cdot \vec{B}/B^2$) profiles are shown in Fig. 4.1, and have been experimentally verified in the outer region (r/a>.7, Shen, 1991) of the MST plasma. The gradient in the normalized parallel current in the presence of the rational $q$-surfaces provides an unstable condition for resistive tearing instabilities (Furth, 1963). Such instabilities are observed experimentally in the ubiquitous presence of nonlinearly saturated magnetic fluctuations with spatial Fourier mode numbers coresponding to the lowest order rational surfaces in MST ($q_r = m/n = 1/5, 1/6, 1/7,$ and $1/8$).

Fig. 4.2 shows typical frequency (power) spectra for magnetic fluctuations measured at the edge (r/a=.97) of MST with coils incorporated into the two-channel EEA probe. The dominant low frequency (10-30 kHz) feature especially prominent in the toroidal ($B_\phi$) component and to a lesser extent in the poloidal ($B_\theta$) component has been identified (Assadi, 1992) as being due to the tearing instability. Tearing mode theory predicts a purely imaginary (unstable) frequency in the plasma frame. The ~15 kHz frequency observed in the experiment is interpreted as a Doppler shift frequency ($\omega = \vec{k} \cdot \vec{v}_{plasma}$) due to plasma rotation in the lab frame. The rms amplitude of the magnetic fluctuations (dominated by the tearing modes m=1,n=5,6,7,8) is generally 1-2% of the edge poloidal equilibrium field, but exhibits a weak dependence on Lundquist number ($S = \tau_R/\tau_A = aB/\eta \cdot \sqrt{\mu_o/\rho}$), decreasing at higher S (Assadi, 1994).

Both the toroidal and poloidal magnetic fluctuation spectra exhibit a power law decay across the high frequency bandwidth (20-250 kHz). For the case shown in Fig. 4.2 the toroidal field fluctuation spectrum follows a $\omega^{-2.6}$

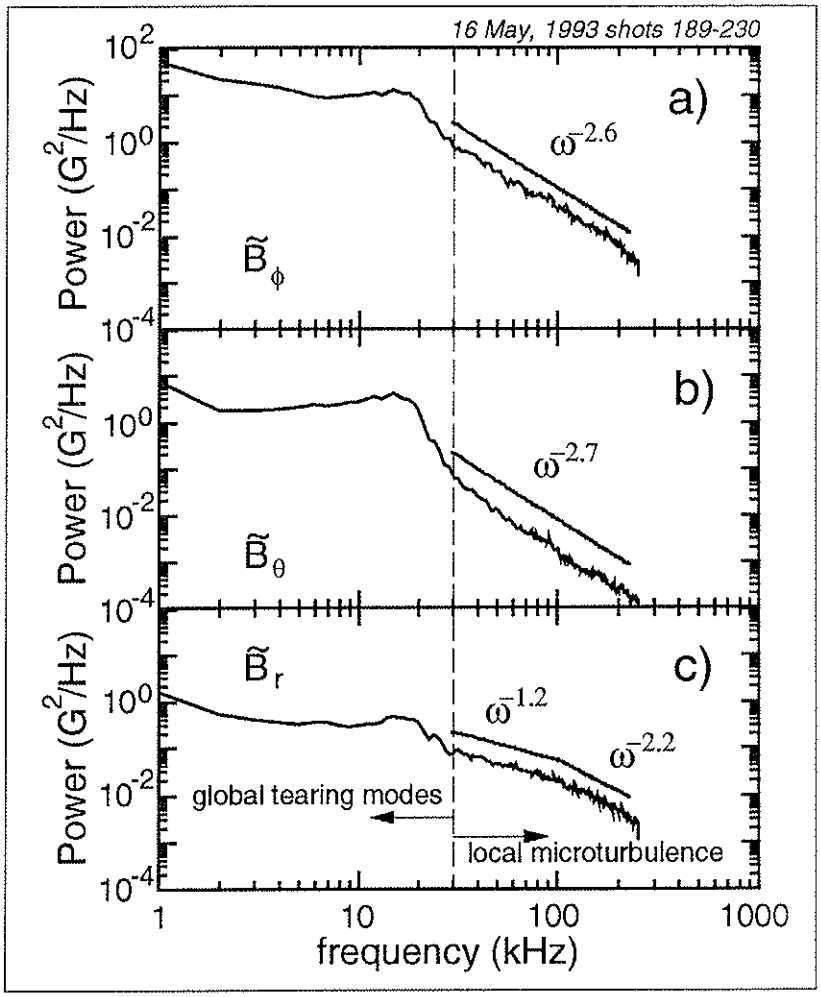


*Fig. 4.2 Frequency power spectra for components of the magnetic fluctuations and power law fits at high frequency 2.5 cm from the wall: a) perpendicular (toroidal) component, b) parallel (poloidal) component, and c) radial component*

power law and the poloidal component follows a $\omega^{-2.7}$ power law (but more than an order of magnitude down in power). The radial magnetic fluctuation spectrum follows a power law with exponent -1.2 below about 100 kHz, but falls more rapidly at higher frequency ($\omega^{-2.2}$). If the dispersion relation for the high frequency fluctuations is linear (e.g. $\omega = kv_{Alfven}$) then the wavenumber power spectrum also exhibits a power law decay. The observation that the power in the magnetic fluctuations follows a power law is evidence for the presence of a nonlinear (energy-conserving) self-similar cascade. The region of the spectrum following a power law is called the "inertial range." The prototype of the inertial range spectrum is the Kolmogorov spectrum of flow fluctuations for 3D Navier-Stokes turbulence which has a power law dependence $k^{-5/3}$. It was shown by Kraichnan (Kraichnan, 1965) that (2D or 3D) MHD turbulence should exhibit an inertial range spectrum that goes like $k^{-3/2}$. Only the radial magnetic fluctuations in MST come close to following the prediction of Kraichnan and only below 100 kHz. The dispersion relation for the high frequency fluctuations is not well known; two-point estimates of the wavenumber spectrum show a very broad distribution of power at each frequency. However, the general features of the power spectra shown in Fig. 4.2 are robust across a range of plasma parameters, radial positions, and measuring instruments; the toroidal and poloidal spectra fall at roughly $\omega^{-5/2}$ and the radial field spectrum decays at $\omega^{-3/2}$ below 100 kHz and more steeply above 100 kHz. The presence of a nonlinear cascade that carries energy from the equilibrium field and large scale ($\lambda \sim a = 51$ cm) tearing modes to the microscopic scale ($\lambda \sim \rho_i \sim 1$ cm) was proposed as a mechanism for anomalous heating of ions observed in the RFP (Mattor, 1992). Correlation between high frequency magnetic fluctuations and ion

heating are observed during discrete dynamo events in MST and is interpreted as evidence for the presence of such a cascade (Scime, 1992). This line of research is ripe for further investigation and promises to provide insights into the nature of the high frequency magnetic fluctuations in MST with implications for both transport and ion heating in the RFP. Further measurements of the characteristics of the high frequency magnetic fluctuations in MST are provided in the references (Shen, 1992; Assadi, 1994; Stoneking, 1992).

The amplitude ($\left\langle \tilde{B}^2 \right\rangle^{1/2} / B_o$) of the magnetic fluctuations in the RFP (~2%) is considerably higher than in the tokamak (~$10^{-4}$). This fact combined with the presence of several low order rational $q$ surfaces leads to the prediction that the magnetic field in the RFP should be stochastic: Magnetic islands form on the rational $q$ surfaces in the presence of finite resistivity and available free energy in the form of current or pressure gradients (tearing or interchange modes respectively). The magnetic field topology is altered by field line reconnection at the X-points of the magnetic islands. The radial width of a magnetic island with a given magnetic fluctuation amplitude can be expressed as

$$W = 4\sqrt{\frac{L_s}{k_\perp}\frac{\left\langle \tilde{B}_r^{\,2} \right\rangle^{1/2}}{B_o}}, \tag{4.14}$$

where the magnetic shear length is

$$L_s \equiv \left| \frac{r}{Rq^2}\frac{dq}{dr} \right|^{-1} \approx a/2, \tag{4.15}$$

and the perpendicular wavenumber is $k_\perp \approx 1/a$ for the global tearing modes in MST. For a total magnetic fluctuation amplitude of 2% due to ~4 dominant modes (m=1,n=5,6,7 &8 in MST), each mode has an amplitude (relative to the equilibrium field) of about 1%. Eq. 4.14 then predicts island widths at each rational surface of about 10 cm. Since the low order rational surfaces are separated by 5 cm or less, the islands due to adjacent rational $q$ surfaces should overlap. Such island overlap over a large portion of the minor radius causes the field lines to become "braided" or stochastic (Rosenbluth, 1966). 3D MHD numerical simulations of the RFP also predict field stochasticity due to the magnetic fluctuations associated with the tearing instability in the RFP (Schnack, 1985).

## *4.4 Review of stochastic transport theory*

### 4.4.1 Stochastic heat transport

The subject of plasma transport in a stochastic magnetic field has been of interest for more than fifteen years. Early on it was recognized that stochastic magnetic fields could greatly degrade energy confinement in the tokamak (Callen, 1977; Rechester, 1978). A stochastic or braided magnetic field connects regions of the plasma that are separated radially. Since plasma particle and energy transport parallel to the magnetic field is much faster than transport perpendicular to the field, particles and energy can flow along the stochastic field and reach the edge region faster than classical transport processes allow. It is immediately apparent that electron (particle and heat)

transport is favored in a stochastic field due the higher parallel mobility of the electron. In steady state it is necessary to have ambipolar particle transport in order to prevent continuous charging of the plasma. Because of the complication of considering ambipolar electric fields, the first treatments of stochastic transport dealt with electron *heat* transport only, assuming a small number of high energy electrons carried the heat out but represented a small charge loss. There are two limiting regimes in which the stochastic electron heat diffusivity can be expressed. In the collisional or fluid regime, Callen (Callen, 1977) expressed the effective radial heat diffusivity augmented by the presence of a stochastic field as

$$\chi_{eff} \approx \chi_{\perp} + \left(\tilde{B}_r / B_o\right)^2 \chi_{\parallel}, \tag{4.16}$$

where $\chi_{\perp} \approx \rho^2 \upsilon$ and $\chi_{\parallel} \approx \lambda^2 \upsilon$ are the classical perpendicular and parallel thermal diffusivities respectively ($\rho$ is the gyro-radius, $\lambda$ is the parallel mean free path, and $\nu$ is the collision frequency). The second term in eq. 4.16 represents classical parallel heat conduction carrying energy out of the plasma because of the radial wander of the field lines. For the amplitude of the magnetic fluctuations in MST the stochastic diffusivity term will dominate the classical perpendicular term, $\chi_{\perp}$, so it will be dropped from here on. In the collisionless limit, Rechester and Rosenbluth (Rechester, 1978) express the stochastic diffusivity as

$$\chi_{st} = \left(\tilde{B}_r / B_o\right)^2 L_{ac} \left\langle v_{\parallel} \right\rangle, \tag{4.17}$$

where $L_{ac} = \left(\int \tilde{B}_r(0)\tilde{B}_r(z)dz\right)/B_o^2$ is the parallel autocorrelation length of the magnetic fluctuations. The regime of interest is thus decided by the parallel collisional mean free path relative to the parallel autcorrelation length of the magnetic turbulence. Harvey *et al.* (Harvey, 1981) connected the two regimes by defining a hybrid length scale by $L_{eff}^{-1} = L_{ac}^{-1} + \lambda^{-1}$. The stochastic diffusivity is then

$$\chi_{st} = \left(\tilde{B}_r/B_o\right)^2 L_{eff}\left\langle v_{\parallel}\right\rangle, \tag{4.18}$$

Eqs. 4.17 and 4.18 show explicitly the dependence on velocity that makes stochastic transport favor electrons.

The parallel autocorrelation length $L_{ac}$ can be expressed as $L_{ac} \approx \pi/\Delta k_{\parallel}$ (Krommes, 1983). The parallel spectral width of the magnetic turbulence expressed in terms of the toroidal and poloidal mode number widths is

$$\Delta k_{\parallel} = \frac{\Delta m}{a}\left(\frac{B_\theta}{B}\right) + \frac{\Delta n}{R}\left(\frac{B_\phi}{B}\right). \tag{4.19}$$

The magnetic turbulence in the RFP is dominated by low frequency global modes with radial widths comparable to the minor radius (Ho, 1991). The toroidal and poloidal mode spectra are therefore expected to be relatively independent of radius. The radial profile of $\Delta k_{\parallel}$ is then determined by the magnetic shear. In MST, the width of the toroidal mode number spectrum at low frequency is about $\Delta n \approx 4$; the poloidal mode spectrum is dominated by $m$=1, with a very narrow spread, $\Delta m = 0-1$. Since the magnetic field is mostly

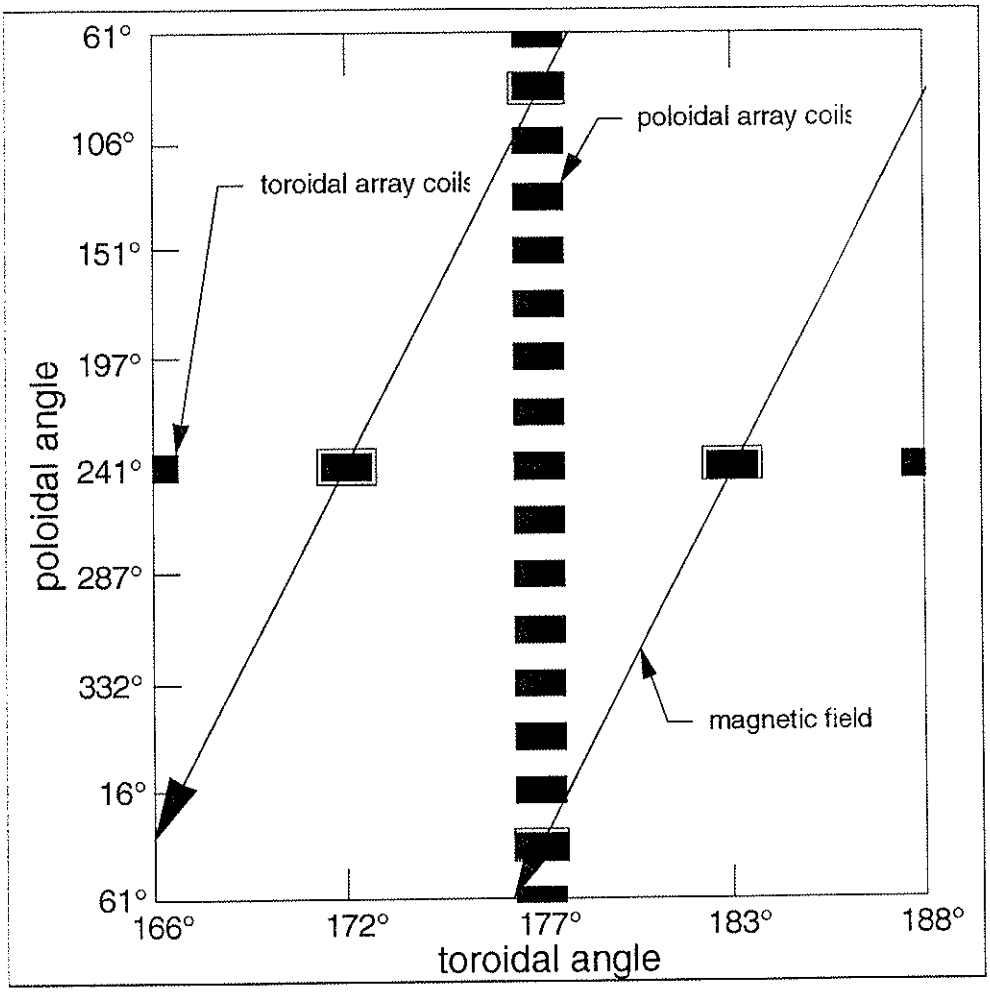


*Fig. 4.3 Fixed array coils and the edge magnetic field direction. The highlighted coils indicate those used to measure the parallel coherence length of the magnetic fluctuations.*

poloidal at the edge of the RFP, a small poloidal spectral width makes for a long correlation length of the fluctuations. Measurements were made outside the plasma with fixed coils mounted on the MST vacuum vessel to determine the parallel correlation length for the magnetic tubulence. There are two (1D) arrays of these coils, a toroidal array at 241° poloidal, and a poloidal array at 180° toroidal (directly opposite the poloidal gap); see Fig. 3.4 for poloidal angle

reference. Fig. 4.3 shows the region where the two arrays intersect unwrapped into a rectangle. Also shown is the field line direction determined from the operations signals $F$ and $\Theta$. The coherence was measured between two pairs of coils that laid on the same field line, separated by 5.6° toroidally, 157.5° poloidally, and 1.38 m measured along the field line. The parallel coherence length (or correlation length) was determined by assuming the coherence drop along the field direction falls off exponentially as discussed below in section 4.6.3. The results of that calculation are shown in Fig. 4.4 for the two coil pairs. At low frequency the two measurements agree and give a correlation length for the dominant magnetic turbulence of 3.5 - 4 m. At high frequency the correlation length is about 1 m, and the two measurements differ slightly suggesting a poloidal assymetry in the high frequency magnetic turbulence. Fig. 4.5 shows the expected parallel correlation length versus minor radius for three values of the poloidal spectral width, $\Delta m$= 0, .5, and 1, using MPFM magnetic field profiles. If the poloidal spectral width were exactly zero, the parallel correlation length would go to infinity at the reversal surface. The measured value for the correlation length at low frequency is best fit by a poloidal spectral width of about 0.5. The value for the parallel coherence length in the core region of MST is about 1 m independent of the poloidal spectral width.

The mean free path for collisions in MST using a typical temperature of 100 eV and density of $10^{13}$ cm$^{-3}$ is $\lambda \sim$ 10 m, significantly larger than the parallel autocorrelation length of the magnetic fluctuations. MST is in the collisionless regime and eq. 4.17 is applicable. For a typical magnetic fluctuation amplitude of 1-2% in MST, eq. 4.17 predicts a stochastic thermal diffusivity $\chi_{st} > 1000$ m$^2$/s

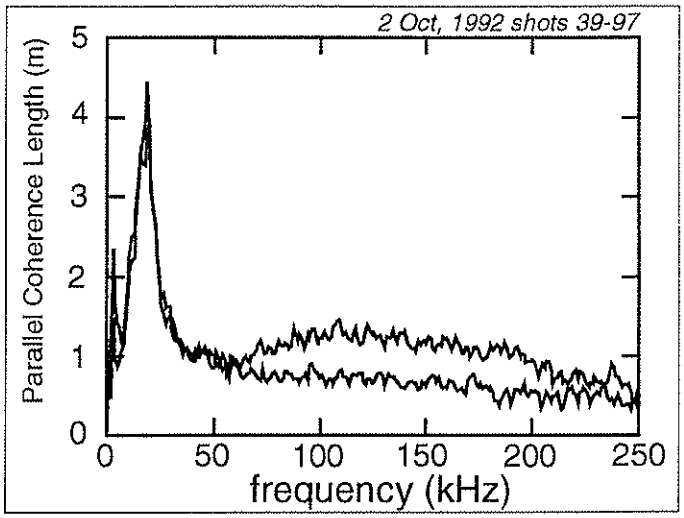


*Fig. 4.4 The parallel coherence length for the (toroidal) magnetic fluctuations measured with the fixed array coils.*

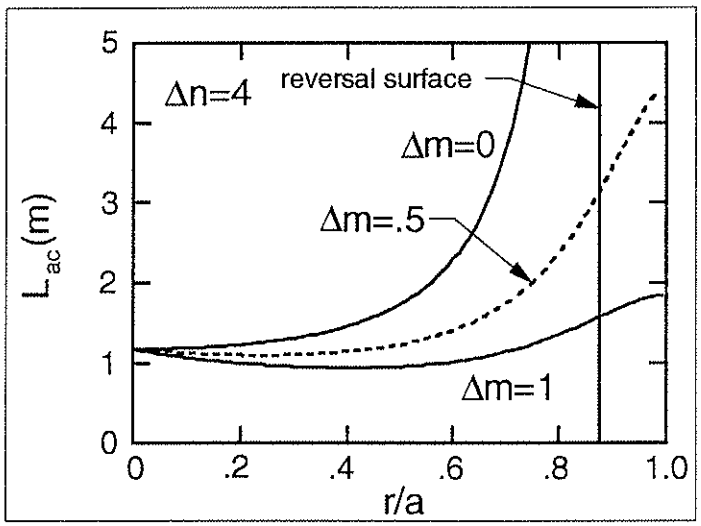


*Fig. 4.5 Calulations of the parallel auto-correlation length of the magnetic fluctuations for three values of the poloidal mode spectrum width and based on a constant spectrum of mode amplitudes across the minor radius. The poloidal spectral width of Δm=.5 best fits the edge measurements at low frequency.*

at least an order of magnitude larger than the observed global effective diffusivity. This naive comparison does not represent a conclusive proof that the stochastic diffusion eq. 4.17 is not operative in MST. What is required to test the stochastic diffusion equation carefully is a local measurement of the magnetic fluctuation induced *conductive* electron heat flux, *and* the local temperature gradient. The diffusivity can then be calculated from the equation:

$$n\chi_{st}\nabla T = \frac{3J\left\langle \tilde{T}\tilde{B}_r \right\rangle}{2eB_o}. \tag{4.20}$$

4.4.2 Stochastic particle transport

When considering particle transport due to magnetic fluctuations the situation is complicated by the apparent nonambipolar nature of the mechanism. The experimental observation that the plasma does *not* continuously charge up during the discharge (as evidenced by relatively constant plasma rotation) leads to four possible expectations regarding magnetic particle transport in a stochastic field: 1) Transport in the RFP is not governed by magnetic fluctuations, but by electrostatic fluctuations (the first term in Eq. 4.10. 2) Magnetic transport is for some reason instrinsically ambipolar despite the apparent favoring of electron transport in eqs. 4.17 and 4.18. 3) Magnetic transport is not intrinsically ambipolar but becomes ambipolar in the presence of a radial ambipolar potential generated by an initial transport of electrons. 4) Magnetic transport is non-ambipolar and the overall ambipolarity of particle transport is assured by another transport mechanism that favors ion transport.

It remains an open question whether transport in the core of the RFP (or the tokamak for that matter) is governed by electrostatic or magnetic fluctuations. If the transport is electrostatically driven, then there is no problem with ambipolarity since the mechanism is inherently ambipolar (for turbulence scale lengths larger than the ion gyro-radius). The results of this work contribute significantly to resolving the question of the transport mechanism in the core of the RFP.

R.E. Waltz (Waltz, 1982) has put forward an argument that magnetic fluctuation induced particle transport should be instrinsically ambipolar for normal modes localized to the $q$-rational surfaces. The non-ambipolar particle flux is proportional to $\mathrm{Re}\left\langle \tilde{J}_{\parallel}^{*}\tilde{B}_{r}\right\rangle$, where $\tilde{J}_{\parallel}$ is the total parallel current fluctuation. Using Ampere's Law and Fourier decomposing in the dimension perpendicular to the local equilibrium magnetic field, the non-ambipolar flux is proportional to

$$\mathrm{Re}\left\langle \tilde{J}_{\parallel}^{*}\tilde{B}_{r}\right\rangle \propto \left\langle \frac{\partial \tilde{B}_{\perp}}{\partial r}^{*}\tilde{B}_{r}\right\rangle = \frac{\partial}{\partial r}\left\langle \tilde{B}_{\perp}^{*}\tilde{B}_{r}\right\rangle - \left\langle \tilde{B}_{\perp}^{*}\frac{\partial \tilde{B}_{r}}{\partial r}\right\rangle . \tag{4.21}$$

Waltz's argument implies that $\tilde{B}_{\parallel}=0$ so that $\partial\tilde{B}_{r}/\partial r=-ik_{\perp}\tilde{B}_{\perp}$ from $\nabla\cdot\tilde{\boldsymbol{B}}=0$. The second term on the right side of Eq. 4.21 is then purely imaginary. The first term vanishes according to Waltz when averaged over the radial width of the normal mode localized to the resonant surface, because $\tilde{B}\rightarrow 0$ away from the resonant surface. The argument fails to be applicable in MST for two reasons. First, $\tilde{B}_{\parallel}\neq 0$ for the dominant (tearing) fluctuations. In fact, the parallel fluctuations ($\tilde{B}_{\theta}$) at the edge are comparable in magnitude to the edge perpendicular fluctuations ($\tilde{B}_{\phi}$). Second, numerical simulations of MHD activity

in the RFP plasma (Ho, 1991) indicate that the radial widths of the tearing modes extend across the entire minor radius and are *not* localized to the rational $q$ surfaces. The first term on the right side of Eq. 4.21 is the gradient of the magnetic Reynold's stress (or the perpendicular torque due to $\boldsymbol{J}_r \times \boldsymbol{B}$) and is important in generating flow (Craddock, 1991).

The question of the effects of a radial ambipolar electric field on the magnetic transport in a stochastic field was taken up by Callen (Callen, 1977) and Harvey *et al.* (Harvey, 1981). Harvey *et al.* derived an equation that describes the effect on the (gyro-orbit averaged) distribution function of stochastic transport in the presence of a radial ambipolar electric field:

$$\left.\frac{\partial\langle f\rangle}{\partial t}\right|_{st} = \frac{|v_{\parallel}|}{r}\mathcal{L}rD_m\mathcal{L}\langle f\rangle. \tag{4.22}$$

where $\mathcal{L} = (\partial/\partial r) - \left(eE_A/mv_{\parallel}\right)\left(\partial/\partial v_{\parallel}\right)$, $D_M = \left\langle \tilde{B}_r^{\,2}/B_o^{\,2}\right\rangle L_{eff}$ as in Eq. 4.18 and $E_A$ is the ambipolar electric field. Integrating Eq. 4.22 over the velocity distribution (the zeroth moment) gives the divergence of the transported flux: $\partial n/\partial t = -r^{-1}\partial(r\Gamma)/\partial r$ in cylindrical coordinates. Solving for the flux results in the expression

$$\Gamma_r = -\sqrt{\pi}D_M v_{th}\left(\frac{1}{n}\frac{\partial n}{\partial r} + \frac{1}{2T}\frac{\partial T}{\partial r} + \frac{eE_A}{T}\right)n. \tag{4.23}$$

Letting $E_A$ and the temperature gradient go to zero in eq. 4.23 recovers a diffusion coefficient consistent with the stochastic heat diffusivity of eq. 4.18.

For some value of the radial ambipolar electric field the flux is "turned off." $E_A$ is found by setting the factor in parentheses (Eq. 4.23) to zero,

$$E_A = -\frac{T}{e}\left(\frac{1}{n}\frac{\partial n}{\partial r}+\frac{1}{2T}\frac{\partial T}{\partial r}\right). \tag{4.24}$$

This picture is one of total electrostatic confinement of electrons (consider fixed ions for the moment). Eq. 4.24 can be obtained (for no temperature gradient) if the electrons satisfy the Boltzmann relation in the radial direction: $n_e = n_{eo}\exp\left(-e\phi_A(r)/T_e\right)$. The plasma rotation caused by $\boldsymbol{E}_A \times \boldsymbol{B}$ using eq. 4.24 is in the same direction and almost exactly the same magnitude as the ion diamagnetic drift. The observation of plasma rotation at twice the ion diamagnetic drift ($v_{Di} + v_{E\times B}$) is a signature that this mechanism is operative.

Harvey *et al.* did not consider ion transport, but their picture has been extended by Ji (Ji, 1992) to include ions. In this picture, the ambipolar electric field does not completely "turn off" the electron flux, but equilibrates the ion and electron fluxes. The resulting ambipolar electric field is (to first order) still given by eq. 4.24, and the ambipolar flux is

$$\Gamma_{r,ambipolar} \approx -2\sqrt{\pi}D_M v_{th,ion}\left(\frac{1}{n}\frac{\partial n}{\partial r}+\frac{1}{2T}\frac{\partial T}{\partial r}\right)n, \tag{4.25}$$

or about twice the diffusion predicted naively by the Rechester-Rosenbluth (Eq. 4.17, Rechester, 1978) formula but using the *ion* thermal velocity.

The last possibility regarding stochastic particle transport is that the electrons are transported stochastically with a diffusion coefficient of the form

given by eq. 4.17, but that overall ambipolar flux is maintained by ion transport due to another mechanism. The only candidate for nonambipolar transport of ions that the author is aware of is the fluctuating polarization drift (Yoshida, 1993): $\tilde{v}_{p,r} = (\omega_c B)^{-1} \partial \tilde{E}_{r,ind} / \partial t$. The inverse of the cyclotron frequency introduces a linear mass dependence, so ion transport is favored. Two factors make this an unlikely candidate for ion transport in MST: 1) The frequencies of the dominant fluctuations in MST are much lower than the ion cyclotron frequency ($\omega_{ci}^{-1} \partial / \partial t \sim 1\%$), and 2) the inductive (or electro-magnetic) electric field fluctuations are estimated to be much smaller than the electrostatic electric field fluctuations in MST.

## *4.5 Review of statistical techniques for analyzing fluctuation data*

### 4.5.1 Ensemble average and signal preprocessing

Turbulent fluctuation data is processed or reduced to a number of physically meaningful quantities by taking a large number (100-200) of time records of the signals of interest. For data presented here the records contained 512 points, sampled at 500 kHz, meaning they were about 1 ms long. Some property of the fluctuation record is evaluated, and averaged over all the records. It is assumed that either the fluctuations are propagating or that each record represents a slightly difference phase of the turbulent fluctuations so that the ensemble average approximates a magnetic flux surface average of the measured property.

Each record is preprocessed, having its mean and linear trend subtracted out, and then multiplied by a window function which tapers the

signal to zero at both ends of the record. These manipulations assure that there will be no aliasing effects introducing frequency components to the Fourier transformed signal that did not exist in the true fluctuations. The window function used for the data presented here is the Hanning window which has the shape of the cosine function: $W = \left(1-\cos\left(2\pi t/t_{record}\right)\right)/2$ (A reference for equations and techniques discussed in this section is Powers, 1988).

4.5.2 Frequency spectra

Each discretely sampled time record $x[n\Delta t]$ (after preprocessing) is fast Fourier transformed (FFT): $X[l\Delta f] = \mathrm{FFT}\left(x[n\Delta t]\right)$. $X$ is complex even though $x$ is real. The record is then "corrected" for amplifier roll-off and phase shift. The Tektronix AM502 Differential Amplifiers used for the EEA current signal were operated with a 100 kHz single pole (simple RC) filter on the input (calibration shows it is actually 80 kHz). The "corrected" EEA record is then given by $X'[l\Delta f] = (1+i2\pi l\Delta f RC)X[l\Delta f]$ where $RC = 2.0$ μs. The amplifiers used for the magnetic signals have a linear phase delay with frequency and a flat gain (over the range 10-200 kHz) and are "corrected" as follows: $X'[l\Delta f] = X[l\Delta f]\exp\left(i\phi_{delay}[l\Delta f]\right)$, where $\phi_{delay} = 1.48x10^{-5} l\Delta f$. To recover the Fourier transform of the magnetic fluctuations, the spectrum was then convolved as follows: $Y[l\Delta f] = -iX[l\Delta f]/2\pi l\Delta f$.

The frequency (power) spectrum for a record is defined as

$$P_x[l\Delta f] = \begin{cases} 2\left|X[l\Delta f]\right|^2 & l = 1,2,\ldots,N/2-1 \\ \left|X[l\Delta f]\right|^2 & l = 0, N/2 \end{cases}, \qquad (4.26)$$

where $N$ is the number of points in the time record. The factor 2 in Eq. 4.26 takes into account power in positive and negative frequencies (or equivalently rightward and leftward propagating fluctuations). The power spectrum is then (ensemble) averaged over $M$ time records.

$$\hat{P}_x[l\Delta f] = \frac{1}{M}\sum_{k=1}^{M} P_x^{(k)}[l\Delta f]. \tag{4.27}$$

The power was then "corrected" for the attenuation caused by the windowing of the original time records. The correction is a multiplicative factor given by

$$\Pi = \left(\frac{1}{N}\sum_{n=1}^{N} W[n\Delta t]^2\right)^{-1}. \tag{4.28}$$

The statistical uncertainty associated with the ensemble averaged power sepctrum is determined by the number of records used in the ensemble: $\sigma_P = \hat{P}/\sqrt{M}$.

The power spectrum is a measure of the relative amplitude (squared) of fluctuations at different frequencies for the signal in question. It is real and positive definite.

### 4.5.3 Cross-power, coherence, and phase

The cross-power between two records, defined in analogy with the (auto-) power spectrum is, after preprocessing, integrating, and correcting for amplifier roll-off and phase shift

$$P_{xy}[l\Delta f]=\begin{cases}2X^{*}[l\Delta f]Y[l\Delta f] & l=1,2,\ldots,N/2-1\\ X^{*}[l\Delta f]Y[l\Delta f] & l=0,N/2\end{cases}. \tag{4.29}$$

The cross-power is ensemble averaged and corrected for the window function in exactly the same way as the power spectrum (Eqs. 4.27 and 4.28). The cross-power is not in general real, so two related real quantities are determined from it: the coherence and the relative phase. The coherence is the amplitude normalized magnitude of the ensemble averaged cross-power. The coherence is

$$\gamma_{xy}[l\Delta f]=\frac{\left|\hat{P}_{xy}[l\Delta f]\right|}{\sqrt{\hat{P}_{x}[l\Delta f]}\sqrt{\hat{P}_{y}[l\Delta f]}}, \tag{4.30}$$

and is real with magnitude between zero and unity. Two signals with unity coherence are identical except for a possible phase shift and constant multiplicative factor. The statistical uncertainty in the coherence is $\sigma_{\gamma}=\sqrt{1-\gamma^{2}}/\sqrt{M}$. The relative (or cross-) phase between two signals is

$$\phi_{xy}[l\Delta f]=\arctan\left(\frac{\mathrm{Im}\left(\hat{P}_{xy}[l\Delta f]\right)}{\mathrm{Re}\left(\hat{P}_{xy}[l\Delta f]\right)}\right). \tag{4.31}$$

The transported radial flux of electrons due to magnetic fluctuations is given by the second term in Eq. 4.10, where the brackets indicate a flux surface average of the product of the fluctuating quantities. If the fluctuations are propagating or have a different phase from record to record (in $\phi$ and $\theta$), then an ensemble

average of time records from "identical" discharges approximates a flux surface average. The transported flux of electrons due to magnetic fluctuations can be written in two equivalent ways:

$$\Gamma_{r,e,mag} = \frac{-\sum_l \mathrm{Re}\left(\hat{P}_{JB}\right)}{eB_o} = \frac{-1}{eB_o}\sum_l \sqrt{\hat{P}_J}\sqrt{\hat{P}_B}\,\gamma_{JB}\cos\left(\phi_{JB}\right). \tag{4.32}$$

4.5.4 Wavenumber spectra

The power in the fluctuations of a particular signal as a function of both frequency and wavenumber, $S(k,\omega)$, can be calculated approximately by a two point measurement of the signal (Beall, 1982). For each record, the (auto-) power of one signal, $P_X$, or the average power of the two signals is calculated as well as the relative phase for that record, $\phi_X$. The relative phase for a single pair of records is

$$\phi_{xy}^{(J)}[l\Delta f] = \arctan\left(\frac{\mathrm{Im}\left(X[l\Delta f]^* Y[l\Delta f]\right)}{\mathrm{Re}\left(X[l\Delta f]^* Y[l\Delta f]\right)}\right). \tag{4.33}$$

The wavenumber (as a function of frequency) for that record pair is the relative phase divided by the spatial separation ($\Delta$) of the two measurements, $k^{(J)} = \phi^{(J)}/\Delta$. The ensemble averaged power in frequency-wavenumber space is estimated by

$$\hat{S}(k,\omega)=\begin{cases}\dfrac{2\Pi}{M}\displaystyle\sum_j P_x^{(j)}[l\Delta f]\Psi_p\left(k^{(j)}[l\Delta f]\right) & l=1,2,\ldots,N/2-1\\ \dfrac{\Pi}{M}\displaystyle\sum_j P_x^{(j)}[l\Delta f]\Psi_p\left(k^{(j)}[l\Delta f]\right) & l=0,N/2\end{cases}, \quad (4.34)$$

where $\Pi$ is the window function correction factor (Eq. 4.28) and $\Psi_p$ is zero or one depending on the value of $k$. The resolvable wavenumbers range from $-\pi/\Delta$ to $+\pi/\Delta$. If the $k$-space range is divided into P bins, indexed by $p$, then

$$\Psi_p=\begin{cases}1 \text{ if } (p-1/2)\Delta k<k^{(j)}<(p+1/2)\Delta k\\ 0 \qquad\qquad \text{otherwise}\end{cases}, \quad (4.35)$$

where $\Delta k=2\pi/\mathrm{P}\Delta$.

*4.6 General characteristics of electron current fluctuations*

4.6.1 Electron current frequency spectrum

Fig. 4.6 shows a typical frequency power spectrum for the electron current fluctuations measured with one channel of the EEA facing the electron flow direction. For comparison, the three components of the magnetic fluctuation power are also shown. The spectrum is featureless and is broader than any of the magnetic fluctuations signals, falling off with a power law dependence of roughly $\omega^{-1}$. The breadth of the electron current spectrum is not surprising, since Ampere's Law ($\tilde{\boldsymbol{J}}=ik\times\tilde{\boldsymbol{B}}$) weights the current fluctuations by a power of the wavenumber, $k$, which probably increases with frequency. A more quantitative comparison of the current fluctuations is complicated by two

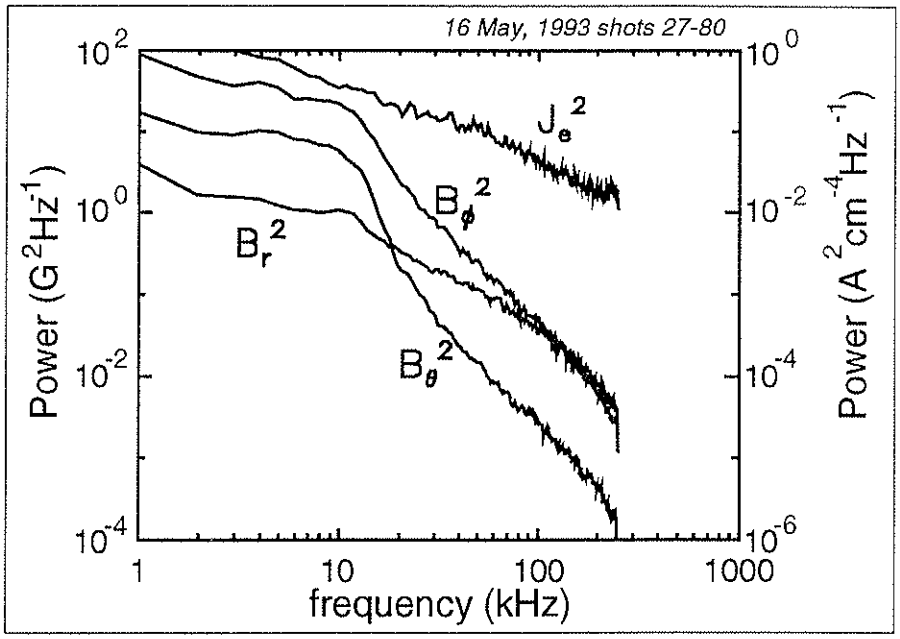


*Fig. 4.6 Frequency power spectrum for forward electron current and components of magnetic field 2.5 cm from the wall; Ip=210 kA.*

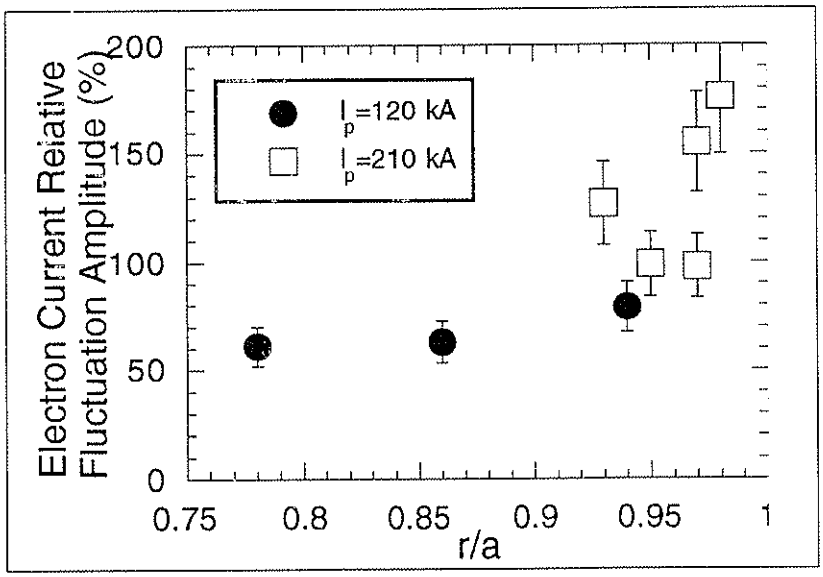


*Fig. 4.7 The relative fluctuation amplitude for the electron current fluctuations at I = 120 kA and 210 kA. (120 kA data taken from 24 May, 1993 shots 61-168 and 210 kA data taken from 16 May, 1993 shots 27-128, 9 May, 1993 shots 51-165, 19 Mar, 1993 shots 120-169, and 20 May, 1993 shots 57-190)*

considerations: First, though the equilibrium current is carried by the fast electron component of the electron distribution (Ch. 3), the extent of the bulk electron component's contribution to the current fluctuations (or for that matter, the ion contribution) is not known. Second, the fast electron current fluctuations are not very coherent with the dominant magnetic fluctuations (see below). The comparison should be made only with that component of the magnetic fluctuations that is *not* curl -free. The curl-free component of the edge magnetic fluctuations is due to current fluctuations in the core of the plasma, near the rational $q$ surfaces.

The relative fluctuation amplitude in the fast electron current fluctuations is shown in Fig. 4.7 as a function of radius (electron current measurements inside r/a~.94 were obtained for reduced plasma current discharges, $I_p$=120 kA to prevent damage to the probe; The data shown in Fig. 4.7 are from the same discharges as the transport measurements reported below). At the extreme edge of the plasma, the electron current fluctuation amplitude is more than 100% of the average level. This fact is apparent from the raw signal (Fig. 2.13). Further inside the plasma, the relative fluctuation amplitude falls off to around 60% of the average level due mostly to an increase in the d.c. level of the signal. The electron current fluctuation amplitude (~100%) is much higher than the fluctuation amplitude measured for the total current fluctuations (~10%) using a magnetic coil array probe or "fork" probe (approximating $\nabla \times \boldsymbol{B} = \mu_o \boldsymbol{J}$) (Shen, 1992b). Again, the uncertainty of the bulk electron contribution to the current fluctuations makes a quantitative comparison difficult, but qualitatively there is reason to expect a higher fluctuation amplitude for EEA measurements. The EEA measurement is extremely localized (aperture diameter is 0.034 cm)

compared to the fork probe sample area (~1 cm diameter) and as such is sensitive to short wavelength fluctuations that the fork probe averages over.

4.6.2 Electron current wavenumber spectra

The two channel EEA and the three channel EEA were employed in concert to measure the wavenumber spectra and coherence lengths of the fast electron current fluctuations. The two probes were located at the same toroidal angle, but were separated by 60° poloidally (Fig. 4.8). Both probes were inserted so that the apertures were 3.5 cm from the wall to measure the poloidal wavenumber spectrum of the forward flowing electron current fluctuations. The two-point method discussed above was used with each of the three channels of the three channel EEA respectively with the forward facing channel of the two channel EEA. The average of the three $k_\theta$ spectra is shown in Fig. 4.9 for two frequency bands (found by summing $S(k,\omega)$ over the frequency band of interest and normalized to maximum of unity) and cast in terms of the poloidal mode number, $m$ ($m = k_\theta a$). At low frequency the spectrum is centered near $m$=0 indicating poloidally symmetric fast electron current fluctuations, and the width is narrow indicating a long poloidal correlation (or coherence) length (see below). At higher frequency the peak is closer to $m$=1. The $m$=0 nature of the low frequency fast electron current fluctuations is intriguing because the dominant low frequency magnetic fluctuations are $m$=1. In Chapter 3, data was presented showing that the equilibrium fast electron current could account for all of the edge parallel current, i.e. the dynamo current. Since the dynamo current sustains the equilibrium magnetic field, it must be $m$=0. This observation does not represent evidence for or against either of the two popular

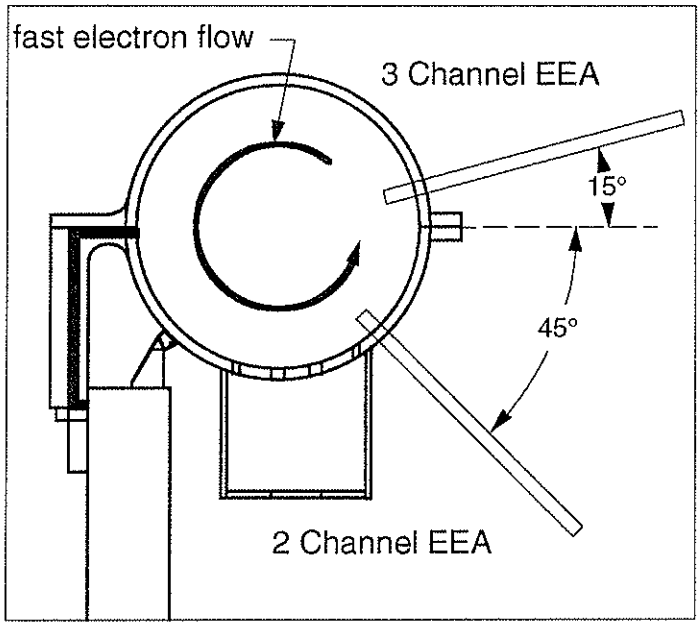


*Fig. 4.8 Poloidal cross-section of MST showing the experimental arrangement for measurement of electron current wavenumber spectra and coherence lengths.*

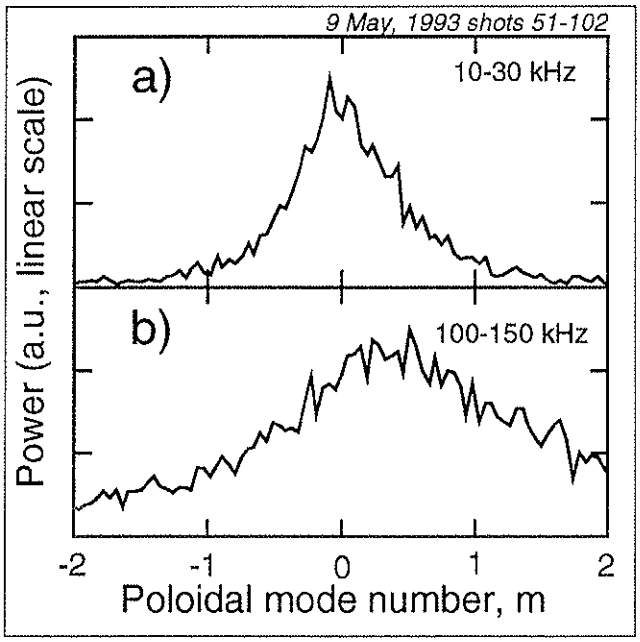


*Fig. 4.9 Poloidal mode number spectra for electron current fluctuations in the frequency bands a) 10-30 kHz and b) 100-150 kHz.*

dynamo theories. The MHD dynamo results from the correlation of $m$=1 velocity and magnetic fluctuations, coupling to drive a $m$=0 (and perhaps a $m$=2) current. The KDT picture does not comment on the mode structure of the current and could be consistent with the observations also. If the electron current fluctuation spectrum had exhibited $m$=1 (or higher $m$) structure, that would have represented evidence that the detected current was *not* the dynamo current. In addition, the $m$=0 nature of the electron current explains (or predicts) the observation that the current fluctuations have a low coherence with the magnetic fluctuations (below). Even though, "instantaneously" the electron current may be correlated with the magnetic fluctuations, the relative phase between the current and magnetic fluctuations has a $m$=1 poloidal structure. For propagating fluctuations, or record to record phase shifts, the coherence is low because the relative phase is not statistically well-defined.

The three channels of the three-channel EEA are separated in the direction perpendicular to the local magnetic field. For edge measurements the perpendicular direction is close to the toroidal direction. Using the two most widely spaced channels (~0.8 cm) the perpendicular wavenumber spectrum of the electron current fluctuations was measured by the two-point method. 3.5 cm from the wall the $k_\perp$ is very broad, but centered near zero (Fig. 4.10) for low frequencies. Cast in terms of an effective toroidal mode number, $n_{eff} = k_\perp R$, the center is at $n_{eff}$<50 (but positive) with $\Delta n$~200. The width of the spectrum, with significant power at wavenumbers above 50 $m^{-1}$ qualitatively explains the difference in the fluctuation amplitude measured with the EEA versus the fork probe (see above). At higher frequencies, the center is shifted to negative $n$, similar to the observation that high frequency magnetic fluctuations have

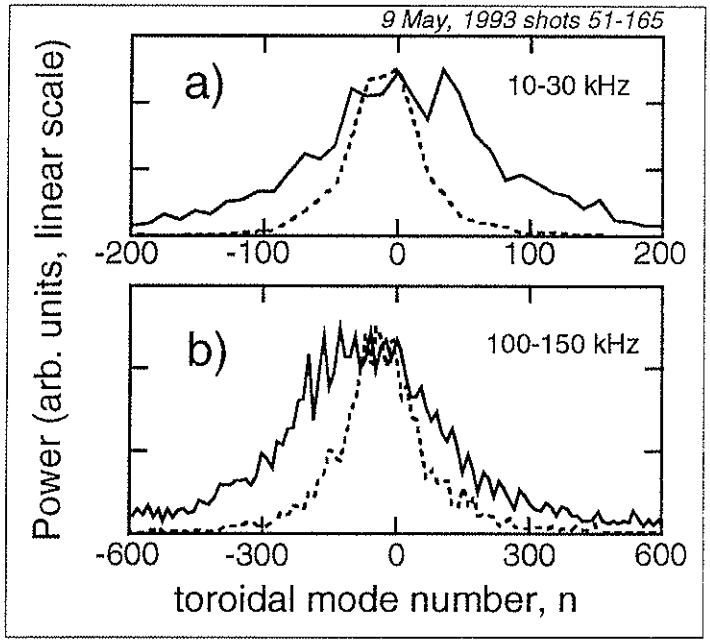


*Fig. 4.10 Perpendicular wavenumber spectra for the electron current fluctuations at 3.5 cm from the wall (solid) and 5 cm from the wall (dashed) integrated over the frequency bands a) 10-30 kHz and b) 100-150 kHz.*

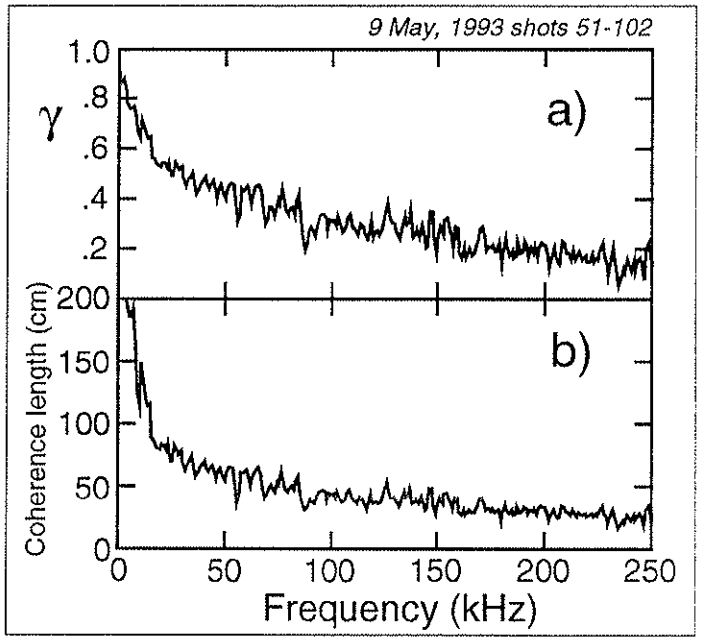


*Fig 4.11 a) Coherence between EEA signals separated 60° poloidally. b) Poloidal coherence length for electron current fluctuations.*

negative toroidal mode numbers relative to the low frequency tearing mode fluctuations (Shen, 1992a). The spectrum becomes narrower in both frequency bands deeper inside the plasma (Fig. 4.10).

### 4.6.3 Electron current coherence lengths

The distance over which a signal becomes decorrelated when measured at two points simultaneously is the correlation length or the coherence length. It is a measure of the width of the wavenumber spectrum since a large number of modes present simultaneously causes decorrelation over short distances. Practically, the method used to obtain the coherence length is to measure the coherence between two measurements of the same signal separated by a distance $\Delta x$ and assuming the coherence falls off exponentially with separation as $\gamma(\omega,\Delta x) = \exp(-\Delta x/L(\omega))$ then $L$ is the coherence length.

The average coherence between the signal from a channel of the three-channel EEA and the forward facing channel of the two-channel EEA in the experimental arrangement described above for the wavenumber spectrum measurements is shown in Fig. 4.11a (3.5 cm from the wall). The poloidal coherence length as a function of frequency (Fig. 4.11b) is about 1 m at low frequency, falling to 25 cm above 200 kHz. Perhaps a more physically interesting measurement would be the parallel coherence length of the electron current fluctuations since the electrons are flowing (collisionlessly) along the field. Because the perpendicular coherence length is much shorter than the parallel (or poloidal) coherence length it would be critical to know precisely the equilibrium field pitch at the point of measurement to ensure that perpendicular decorrelation was not affecting the parallel correlation measurement. It is clear,

however, that the poloidal coherence length is a lower bound on the parallel coherence length.

The perpendicular coherence length of the (fast) electron current fluctuations was determined by measuring the coherence between the three channels of the three-channel EEA. Fig. 4.12a shows the coherence between adjacent EEA channels (separated .4 cm) and between the two "outside" channels. Again, fitting to an exponential, this time with three separation points instead of two ($\Delta x$ = 0 cm, .4 cm, and .8 cm), the perpendicular coherence length was found to be about 5 cm at low frequency falling to 1 cm above 100 kHz (Fig. 4.12b, 3.5 cm from the wall). Further inside the plasma (5 cm from the wall), the perpendicular coherence length is about twice as long at all frequencies (Fig. 4.12b), consistent with the observation that the perpendicular wavenumber spectrum narrows at deeper insertion.

An estimate of the radial coherence length of the electron current fluctuations was made by measuring the change in the poloidal coherence when the two EEAs were moved from the position where both were 3.5 cm from the wall, to a position where one probe was 2 cm from the wall and the other was 5 cm from the wall. The drop in coherence between the two cases determines the radial coherence length of the fluctuations by the equation

$$\gamma_B(\omega) = \gamma_A(\omega)\exp\left(-\Delta r/L_r(\omega)\right), \tag{4.36}$$

where the $A$ subscript indicates the case where the probes were at the same radial position, and $B$ indicates the case when the probes were separated by $\Delta r$ = 3 cm. The radial coherence length of the fluctuations is shown in figure

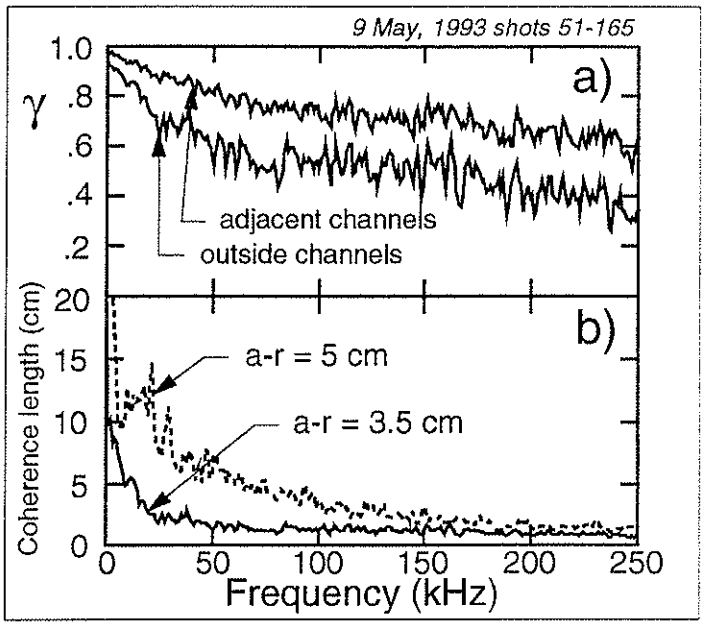


*Fig. 4.12 a) Coherence between signals of the three-channel EEA at 3.5 cm from the wall. b) Perpendicular coherence length for electron current fluctuations 3.5 cm from the wall (solid) and 5 cm from the wall (dashed).*

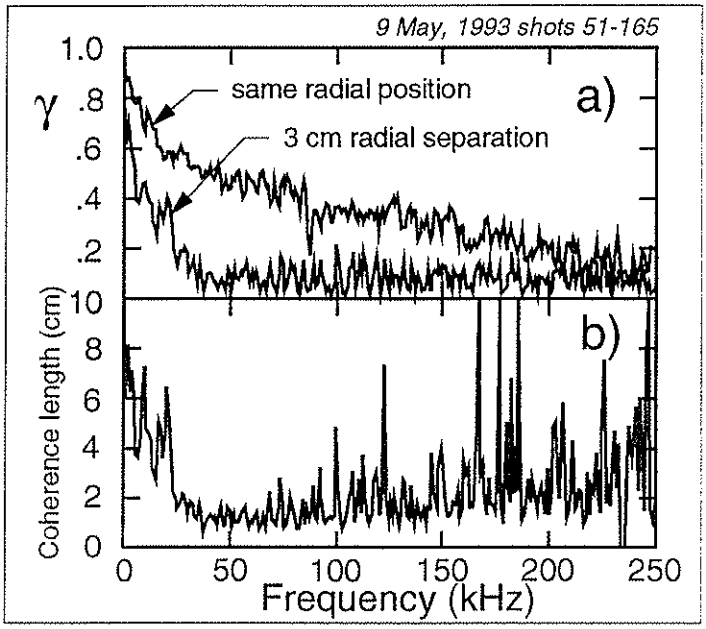


*Fig. 4.13 a) Coherence between poloidally separated EEA signals (60° separation) at the same radial position and separated 3 cm radially. b) Radial coherence length of the electron current fluctuations.*

4.13, and is comparable to the perpendicular coherence length at the same position (about 3.5 cm from the wall).

It is appropriate to compare the measured coherence lengths for the electron current fluctuations with those for the magnetic fluctuations. It is difficult to measure the low frequency coherence lengths for the magnetic fluctuations since they are dominated by global modes with very long coherence lengths. Estimates can be obtained, however, from the mode spectra. The coherence length is determined by the width of the wavenumber spectrum by $L = \pi/\Delta k$. The width of the poloidal mode number spectrum is $\Delta m$ = 0-1 (Assadi, 1994), making the poloidal coherence length greater than 2 m (Fig. 4.4). The toroidal (~perpendicular) coherence length is about 1 m ($\Delta n = 4$) at low frequency. At high frequency (~100 kHz) the parallel coherence length is about 1 m (Fig. 4.4) and the perpendicular coherence length is about 10 cm (Stoneking, 1992). The radial coherence length is approximately half the perpendicular (or toroidal) coherence length at all frequencies (Shen, 1992b). All the coherence lengths for the magnetic fluctuations are considerably longer than those for the electron current fluctuations.

The qualitative picture of the electron current fluctuations in MST provided by the above measurements is one of long, thin filaments aligned with the local magnetic field. The filaments have dimensions roughly given by the coherence lengths, a few centimeters across and more than a meter long.

*4.7 Measurement of magnetic fluctuation induced electron particle transport*

4.7.1 Edge measurements at $I_p$=210 kA

Transport measurements were made at the extreme edge (r/a>.9) of MST in discharges with toroidal plasma current of 210 kA and line averaged plasma density of $1.0\text{x}10^{13}$ $cm^{-3}$. Fig. 4.14 shows the global signals for a typical shot. Also shown for comparison are the signals for 120 kA discharges (dashed) in which transport measurements were performed to r/a~0.75.

The coherence between the electron current fluctuations and the magnetic fluctuations is small, generally between 20% and 40%. A typical example is shown in Fig. 4.15 measured at r/a=.97. The measured coherence is statistically significant. Since the number of records used in the ensemble is about 200, the statistical uncertainty in the coherence is $\sim 1/\sqrt{M} = 7\%$ (above Eq. 4.31). The relative phase between the electron current fluctuations and the radial magnetic fluctuations is close to zero at low frequency, but rises to $\pi/2$ radians at high frequency. The$\pi/2$ phase shift at high frequency is expected for current fluctuations due to local magnetic fluctuations (in the absence of radial propagation). This is seen from the Fourier transform of Ampere's law,

$$\left(\tilde{J}_\theta^* \tilde{B}_r\right) = \left(ik_\phi \tilde{B}_r^* \tilde{B}_r\right) - \left(\frac{\partial \tilde{B}_\phi^*}{\partial r} \tilde{B}_r\right). \tag{4.37}$$

The first term has a $\pi/2$ phase. The second term vanishes if there is no radial propagation of the turbulence ($k_r = 0$). The radial flux of fast electrons due to magnetic fluctuations at r/a=.97 is, from eq. 4.32, $\Gamma_r$<$5\text{x}10^{20}$ $m^{-2}s^{-1}$. Estimates

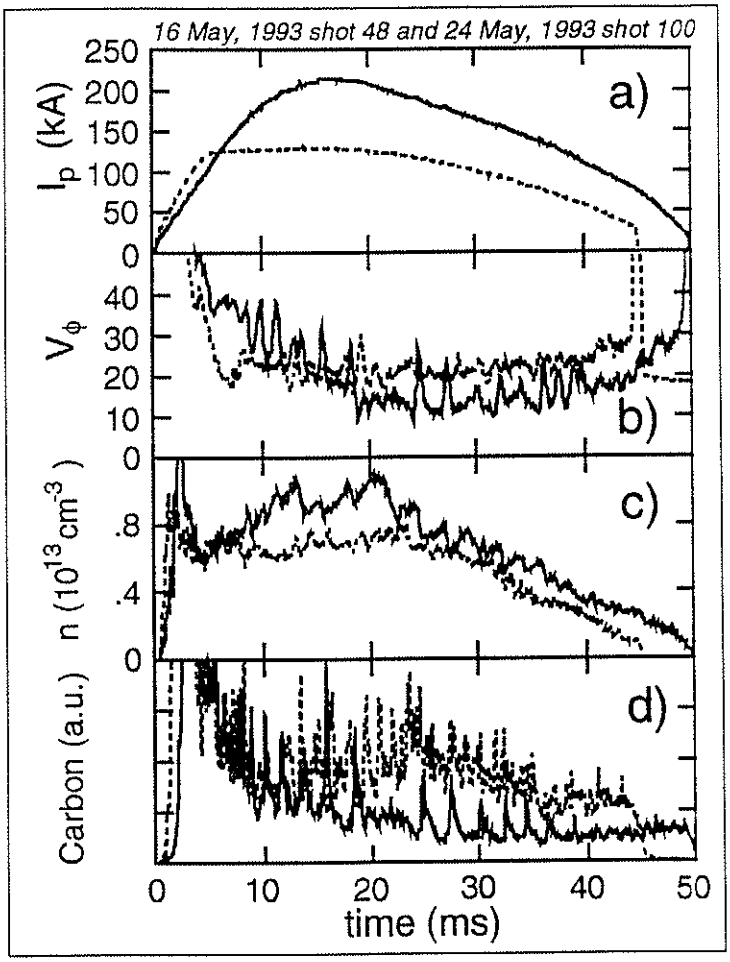


*Fig. 4.14 A comparison of operations signals from a typical 210 kA discharge (solid) and a 120 kA discharge (dashed): a) plasma current, b) toroidal voltage, c) central chord averaged plasma density and d) C III radiation monitor signals.*

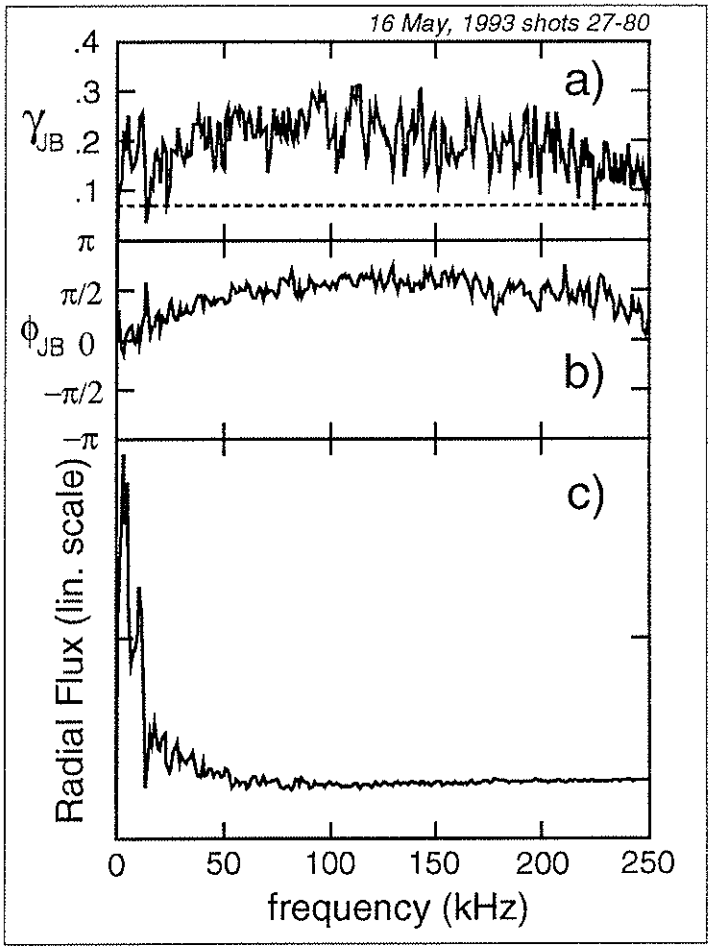


*Fig. 4.15 a) Coherence between electron current fluctuations and radial magnetic fluctuations at r/a=.97, Ip=210 kA, b) the relative phase between Je and Br, and c) the spectrum of the radially transported electron flux.*

of the total radial electron particle flux from $H_\alpha$ emission profiles are $\Gamma_r$=5x$10^{21}$ $m^{-2}s^{-1}$ (Sinitsyn, 1993). This result is consistent with previous measurements of the electrostatic fluctuation driven particle flux (Rempel, 1991) which was found to be sufficient transport to account for all the expected particle flux. Particle (and) energy transport is expected to be significant only in regions of magnetic field stochasticity. The measurements presented here suggest the flux surfaces are relatively intact at the extreme edge of MST (near the last closed flux surface, LCFS). The proximity of the conducting vacuum vessel may account for the presence of intact flux surfaces despite the large amplitude of the magnetic fluctuations. The numerical simulations of the RFP also suggest that flux surfaces close to the conducting wall are closed (Schnack, 1985).

4.7.2 Transport profile at $I_p$=120 kA

In discharges with plasma current of 120 kA, probes can be inserted to r/a=0.75 without catastrophic damage. Results of transport measurements in these low current discharges is shown in Fig. 4.16 (squares). Also shown in Fig. 4.16 are the measurements at 210 kA. The higher current case points have been normalized to the same plasma density as the 120 kA discharges ($\bar{n}$ =.7$\times 10^{13}$ $cm^{-3}$). The total particle flux was estimated, consistent with the edge neutral pressure, and the plasma density profile, and is indicated by the range between the dashed lines on Fig. 4.16. Measurements of electrostatic fluctuation induced particle transport are also shown in Fig. 4.16. Inside r/a=0.85, the fast electron flux due to magnetic fluctuations is consistent with the total expected electron flux. The interpretation is that the magnetic flux surfaces are destroyed inside r/a~0.85, approximately the location of the reversal

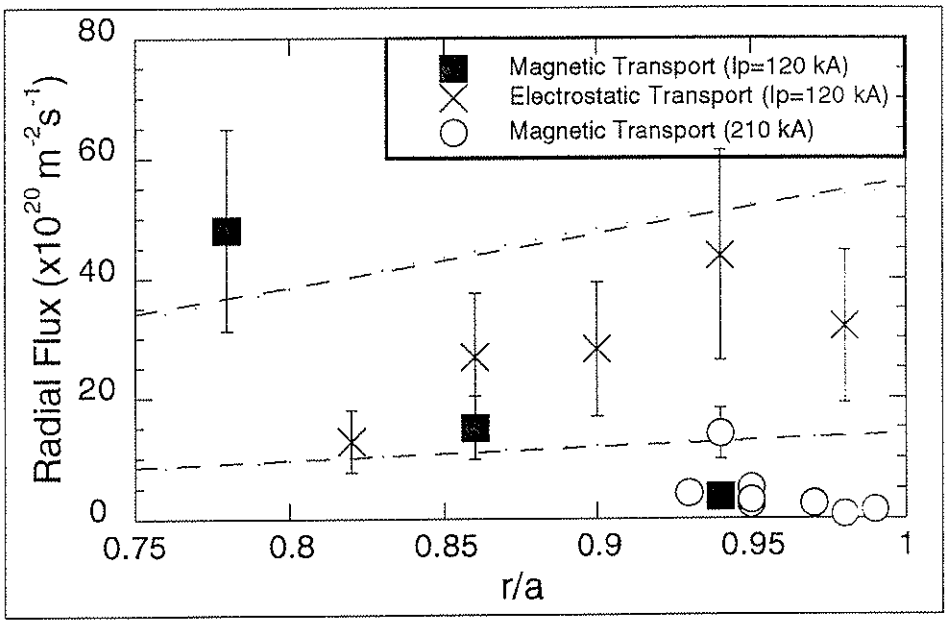


*Fig. 4.16 The profile of the magnetic fluctuation induced fast electron transport increasing to the level of the total flux (dots) inside r/a=0.85. Profile of electrostatic fluctuation induced transport is shown for comparison. 210 kA measurements have been normalized to the same plasma density. See Fig. 4.7 for date and shot ranges for data shown here.*
*(Electrostatic fluctuation measurements provided courtesy of H. Ji)*

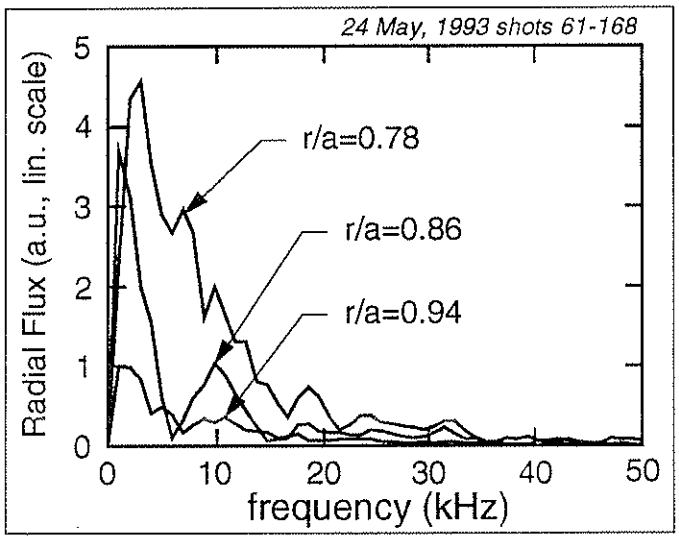


*Fig. 4.17 The spectrally resolved radial flux of fast electrons due to magnetic fluctuation induced transport at 120 kA.*

surface. The electrostatic fluctuation driven transport which is large at the edge falls off in the region where the magnetic transport is observed to increase. In Fig 4.17 the flux is shown as a function of frequency (i.e. the real part of the cross-power divided by $eB_o$) for the 120 kA cases. The flux is dominated by the low frequency part of the spectrum, because a) the fluctuation power is concentrated at low frequency, and b) the phase goes to $\pi/2$ radians at high frequency (as in Fig. 4.15). The results reinforce the expectation that the low frequency tearing fluctuations, resonant at the rational $q$ surfaces, are responsible for the field stochasticization and resulting transport.

### 4.7.3 Comparison with stochastic transport theory

The fast electron density profile for the 120 kA discharge conditions is shown in Fig. 4.18, calculated in the same manner as described in Ch. 3. By combining the fast electron density profile, and the fast electron transport flux (due to magnetic fluctuations), the fast electron particle diffusion coefficient can be estimated from $\Gamma_{r,mag} = -D_{fast,mag}\nabla n_{fast}$. In the region where the magnetic fluctuation induced transport becomes dominant (r/a~.8), the fast electron diffusion coefficient is $D_{fast,mag} = 500 \pm 200$ m$^2$/s. This value is five to ten times greater than the global particle diffusion coefficient required to reproduce the measured density profile and fueling profile (measured from the $H_\alpha$ radiation) and is consistent with the observation (Ch 3) that the fast electron population comprises 10-20% of the bulk electron population at the edge. Another way of saying this is that the fast electron density gradient scale length is roughly equal to the global density gradient scale length (within a factor of two).

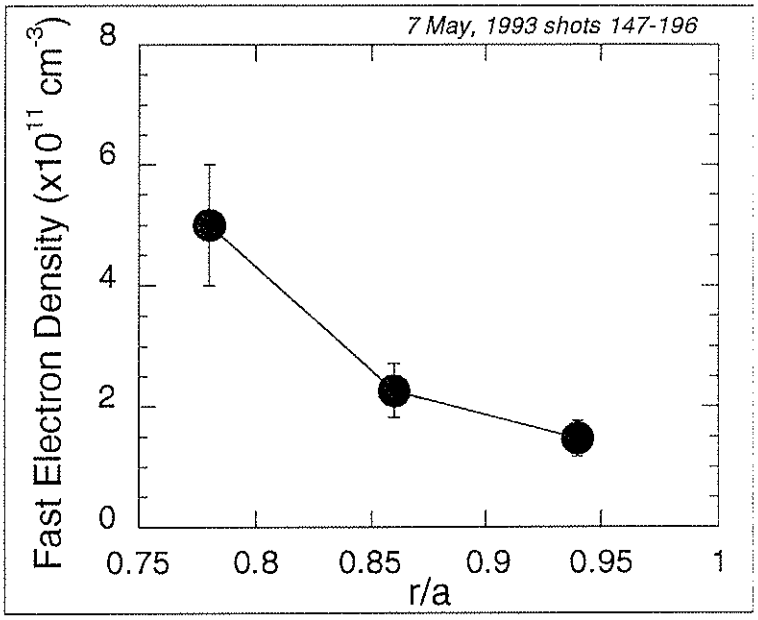


*Fig. 4.18 The fast electron density profile at $I_p$=120 kA.*

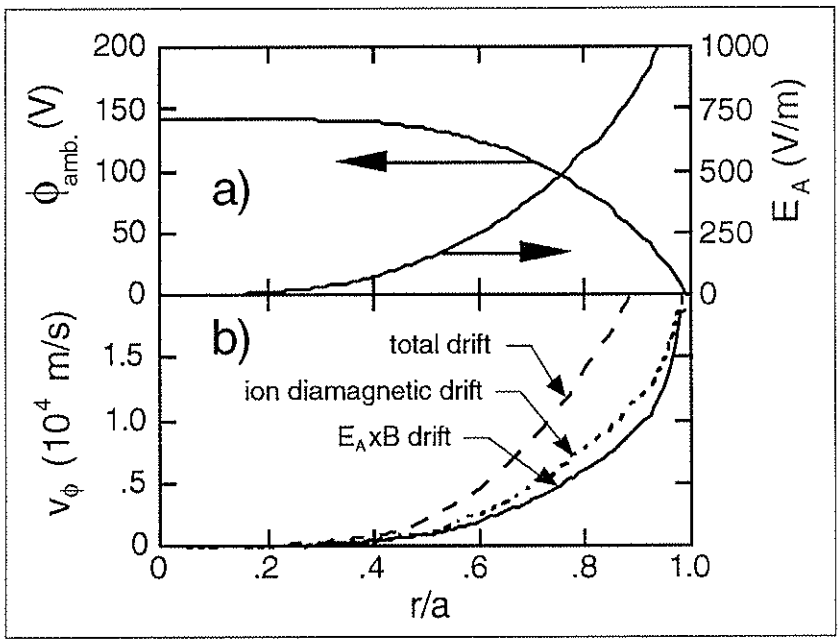


*Fig. 4.19 a) The predicted ambipolar electric field (Eq.4.24) and potential in the presence of stochastic transport. b) the toroidal flow velocity resulting from the ExB and diamagnetic drifts.*

While the fast electron diffusion is five to ten times faster than the global (or ion) diffusion rate, the value obtained from the measurements is about 4 times smaller than the naive application of the Rechester-Rosenbluth type stochastic test particle diffusion would predict (Rechester, 1978). For 80 eV fast electrons, Eq. 4.17 predicts stochastic diffusion at roughly 2000 $m^2/s$. It should be emphasized that the maximum possible transport due to magnetic fluctuations is roughly five times greater than the measured transport. If the coherence between the current fluctuations and the radial magnetic fluctuations were unity, the transport would agree with the Rechester-Rosenbluth prediction, and RFP transport would be significantly worse than it is.

Particle transport must be ambipolar to avoid continuous charging of the plasma. In section 4.4.2 it was shown that Waltz's argument (Waltz, 1982) for intrinsically ambipolar transport due to magnetic fluctuations does not apply to MST. The most obvious mechanism for preserving ambipolar transport is the effects of a radial ambipolar electric field as discussed by Harvey *et al.* (Harvey, 1981). Ji's extension (Ji, 1992) of the work of Harvey *et al.*, shows that a radial ambipolar electric field reduces the transported flux to twice the *ion* stochastic diffusion rate. For the plasma conditions of interest here ($T_i$~60 eV), Eq. 4.25 predicts the global particle diffusion coefficient to be roughly 100 $m^2/s$ consistent with observations (within a factor of two). The magnitude of the electric field necessary to suppress electron transport and maintain ambipolarity is given by Eq. 4.24. A model plasma density and temperature profile ($n/n_o = T_e/T_{eo} = 1-(r/a)^4$) was used to calculate the expected ambipolar electric field (Fig. 4.19a). Since electrons initially escape the plasma along the

stochastic field, the plasma charges positively, and the ambipolar electric field acts to electrostatically confine bulk electrons. The electric field should be about 500 V/m at r/a~.7 in MST. The plasma rotation caused by the *ExB* drift is in the same direction and is the same magnitude as the ion diamagnetic drift ($v_{Di} \approx 5$ km/s for the discharge conditions of interest here). The signature for the presence of an ambipolar electric field due to stochastic diffusion is a plasma rotation (toroidally near the edge of the RFP) with magnitude about twice the ion diamagnetic drift speed (Fig. 4.19b). In MST, the toroidal rotation of the plasma has been inferred from two measurements: 1) The global tearing fluctuations appear at about 20 kHz in the magnetic fluctuation frequency spectrum. If the fluctuations are stationary in the plasma frame, the rotation speed is inferred to be $v = 2\pi Rf/n \approx 10^4$ m/s in the ion diamagnetic drift direction (Sarff, 1993) where $R$ is the major radius, $f$ is the observed frequency of the fluctuations, and $n$ is the toroidal mode number of the fluctuations. The radial location where the plasma has this rotation speed in expected to be near the low order rational surfaces in side the reversal layer (r/a~.6). 2) Measurements of the Doppler shift of a carbon impurity line indicate that the impurity ions flow at roughly $10^4$ m/s ($\sim 2v_{Di}$) in the ion diamagnetic drift direction averaged over r/a from about 0.3 to about 0.7 (Den Hartog, 1993). Another interesting point worth noting is the observation that the magnetic fluctuations seem to propagate in the electron diamagnetic drift direction outside the reversal surface (Shen, 1992). This is consistent with observations of the propagation of local edge turbulence in ZT-40M (Weber, 1990). It has been suggested (Sarff, 1993) that the change in rotation direction reflects the presence of a strong negative electric field (directed inward) at the extreme

edge of the RFP. This is another promising line of research to pursue in the future through measurements of the edge plasma potential. A strong negative electric field at the edge could make the core plasma potential negative (consistent with measurements in the tokamak), but the electric field in the central region is still expected to be directed outward.

The measurements presented in this chapter support the conjecture that global particle transport in the RFP is governed by the stochastic transport of ions. Electrons are for the most part electrostatically confined, the fast tail of the distribution carrying out the electron contribution to the ambipolar particle flux.

### 4.7.4 Energy dependence of stochastic transport

Information about the energy dependence (or equivalently the parallel velocity) dependence of stochastic transport was investigated by varying the repeller bias voltage and taking an ensemble of records at each bias setting. The goal was to test the velocity dependence of Eq. 4.17, the canonical stochastic diffusion coefficient. Since the repeller bias voltage sets the minimum electron parallel velocity required to reach the collecter, the measured signal is the integral over the first moment of the distribution from that minimum velocity to infinity as explained in Ch.2. By correlating the fluctuations in the measured current with the radial magnetic fluctuations the transport flux of electrons with energy greater than $V_r$ is determined. The measurement was performed at r/a~.95 in the region where the magnetic fluctuation induced transport is small compared to the total particle loss rate, but is not zero. The data shown in Fig. 4.20 compares the dependence of the EEA signal on repeller bias (the parallel velocity distribution) with the measured radial flux of

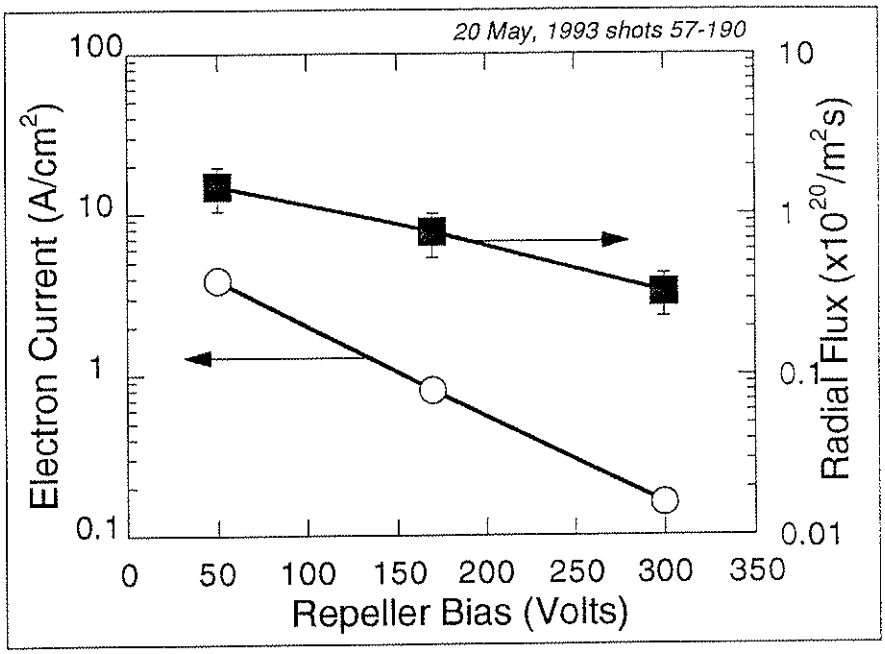


*Fig. 4.20 The energy spread of the radially transported flux is "hotter" than the parallel fast electron distribution at r/a=0.95, $I_p$=210 kA.*

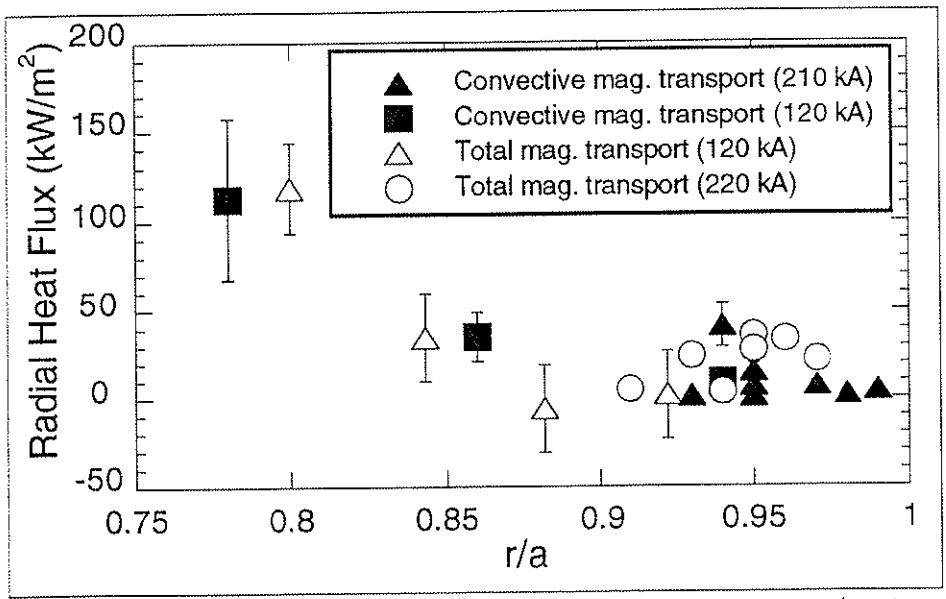


*Fig. 4.21 A comparison of the convective heat transport due to magnetic fluctuations and the total heat transport due to B fluctuations measured with the pyro-bolometer (data courtesy of G. Fiksel).*

electrons measured with the repeller electrode biased to the given value. The immediately apparent result is that the transported flux has a broader distribution in energy, implying that the stochastic diffusion favors higher velocity electrons, as predicted by the canonical Rechester-Rosenbluth type diffusion equation. More carefully, the transported flux with energy greater than the repeller bias can be expressed as

$$\Gamma'_r\left(V_{repeller}\right) = \int_{\sqrt{2V_r/m}}^{\infty} D(v)\nabla f(v)dv. \qquad (4.38)$$

If the diffusion is linearly dependent on velocity as predicted by the stochastic diffusion equation, then Eq. 4.38 is the first moment of the distribution and the dependence of the flux on repeller bias should be the same as the dependence of the parallel current on repeller bias. Fitting an exponential to the electron current signal in Fig. 4.21 gives an effective parallel temperature of 80 eV. The falloff of the transported flux has a 150 eV dependence, roughly twice the parallel effective temperature. Eq. 4.38 can be rexpressed in light of these fits as

$$\Gamma'_r(V_r) \propto \exp\left(-V_r/2T_{eff}\right) \propto \int_{V_r}^{\infty} D(E)E^{-1/2}\exp\left(-E/T_{eff}\right)dE, \qquad (4.39)$$

assuming there is no (effective) temperature gradient (consistent with results of Ch. 3). The dependence of the diffusion on the electron energy is found by taking the derivative of Eq. 4.39 with respect to the repeller bias and then making the substitution of $E$ for $V_r$. Solving for the diffusion coefficient,

$$D(E) \propto \sqrt{E}\exp\left(E/2T_{eff}\right) \text{ or } D(v) \propto v\exp\left(mv^2/4T_{eff}\right). \qquad (4.40)$$

That the stochastic diffusion coefficient is a stronger function of velocity than predicted by Eq. 4.17, supports the thesis that the ambipolar electric field suppresses the transport of low energy electrons preferentially.

4.7.5 Convective nature of transport

The convective energy carried out of the plasma with the fast electrons is found from the particle transport rate times the average particle energy:

$$Q_{r,convective} = \Gamma_r\left(\frac{1}{2}T_{\|,eff} + T_\perp\right). \qquad (4.41)$$

The results of the previous section showed that the effective parallel temperature for the transported population is about twice the actual parallel temperature. For fast electron temperatures $T_\| = 100$ eV and $T_\perp = 30$ eV, the convective energy transport profile is shown in Fig. 4.21 as the solid symbols. The open symbols indicate the measurements of the magnetic fluctuation induced energy transport with the fast pyrobolometer (the second term in Eq. 4.11) (Fiksel, 1994). The results are consistent with all of the measured (magnetic fluctuation induced) energy flux being convectively carried out of the plasma. This result is consistent with the observation that the global effective thermal diffusivity $\chi_{eff} = a^2/2\tau_E$ is comparable to the global particle diffusion coefficient. It is desirable to determine the experimental value for the true thermal diffusivity in order to compare it to the Rechester-Rosenbluth model for

electron thermal transport. Several facts conspire to defeat such a measurement in MST. In order to determine the experimental value for $\chi$, the radial *conductive* heat flux must be measured, along with the density and temperature profiles to solve, $Q_{r,conductive} = n\chi\nabla T$. Since the Rechester-Rosenbluth model is a test particle theory for electrons, the fast electron density and temperature profiles are the quantities of interest. As shown in Ch.3 however, within the uncertainty of the measurement, the fast electron temperature profile is flat at the edge of MST. This fact combined with the observation that the measured energy transport is dominated by the convective term, make it impossible to estimate the thermal diffusivity from the measurements. It is clear in any case, that the thermal diffusivity is not important in the energy confinement picture of the RFP. Energy is transported convectively, so the particle diffusion coefficient is the important confinement quantity.

### 4.7.6 Implications for RFP confinement

This work makes a significant contribution to the understanding of RFP confinement, but the picture is far from complete. In order to track the flow of particles and energy through the RFP plasma, profile measurements of density, electron temperature, ion temperature, radiation power, $H_\alpha$ radiation, and the impurity charge states (summarized by $Z_{eff}$) are required. A crude comparison of the results of this work is now made with the known scaling of the transport parameters in MST.

The central electron temperature (measured by Thomson scattering) in MST is found to have the following dependence on toroidal plasma current and central chord averaged plasma density (Hokin, 1993a):

$$T_{eo} = 8.3 \times 10^3 \bar{n}_e^{-0.34} I^{1.09}. \tag{4.42}$$

Energy flows into the electron population from the external circuit via the plasma resistance, i.e. Ohmic or Joule heating. Some of that energy is collisionally transferred to the ion population, some is radiated when electrons encounter impurity ions and some is transported out of the plasma. For this analysis it is assumed that the transported loss channel is dominant. It was argued in section 4.1.2 that the classical energy equilibration time between ions and electrons is long compared to the global energy confinement time, so the collisional loss to ions may be negligible. It is observed that the ion temperature in the RFP is comparable to the electron temperature (anomalously high), but the details of the heating channel are not well-established. The view taken here is that the ions are heated independently of the electrons, presumably through a cascade of energy from the equilibrium field through fluctuations at increasingly shorter scales (Mattor, 1992). The negligibility of the radiated power is even less solid, however, scaling studies show that radiated power is generally constant (30% of Ohmic) at sufficiently low density (or sufficiently high I/N) (Hokin, 1993a). Under the stated assumptions, the input power is balanced by transport losses. The results of this work indicate that transport losses are dominated by convective loss through stochastic particle transport at the ion stochastic diffusion rate.

$$P_{Ohmic} = Q_{r,convective}\left(4\pi^2 aR\right) \tag{4.43}$$

$$I^2\eta\left(\frac{g2R}{a^2}\right) = \frac{3}{2}T_e D_M v_{\parallel}\nabla n\left(4\pi^2 aR\right) \tag{4.44}$$

$g \approx 5$is the "screw-up" factor for the resistivity due to the helical path a current carrier takes in negotiating a toroidal transit in the RFP equilibrium field. Assuming $T_i \approx T_e \approx T$, the following proportionality holds:

$$I^2 Z^* T^{-3/2} \propto D_M n L_n^{-1} T^{3/2}, \tag{4.45}$$

where $Z^*$ is the plasma resistance anomaly (over the $Z^*$=1 Spitzer value) and $L_n$ is the density gradient scale length. The resistance anomaly is found to increase linearly with plasma current (Hokin, 1993b); however, it is not known if this is truly reflecting the energy going into the electrons or if the increase in $Z^*$ with current is due to increasing power to the ions through the fluctuations that never passes through the electrons. Recall that $D_M$ depends on the square of the magnetic fluctuation amplitude times the parallel correlation length of the fluctuations. The parallel correlation length depends only on the number of dominant modes in the spectrum and should be constant for a given $q$ profile. In the OHTE RFP the amplitude of the magnetic fluctuation amplitude was found to decrease with the Lundquist number, as $S^{-1/2}$ (LaHaye, 1984). In MST the trend is less clear, but perhaps more weakly dependant on $S$ (Assadi, 1984). Numerical simulations done by Nebel *et al.* (Nebel, 1989) indicate that the magnetic fluctuation amplitude should be independent of $S$. Here it is

assumed that $Z^*$ and $D_M$ are constant as well as $L_n$. The resulting dependence of the temperature on current and density is,

$$T = 5.5\times10^3\left(\frac{L_n Z^*}{D_M}\right)^{1/3}\frac{I^{2/3}}{n^{1/3}}. \qquad (4.46)$$

For $L_n$=3a/4, $D_M$=4x10$^{-4}$ m, and $Z^*$=3, independent of current and density, the scaling relation becomes $T = 7.7\times10^4\left(I^{2/3}/n^{1/3}\right)$. The analysis is extremely crude and relies on many weak assumptions. It is significant that the correct density scaling is obtained from the assumptions. The current scaling obtained here is more pessimistic than the results of the observed scaling. The observed scaling would be (approximately) obtained if the magnetic fluctuation amplitude scaled with plasma current to the power -1/2, but was independant of density. Such a prediction is not inconsistent with the observed dependence of the fluctuation amplitude with current in MST (Assadi, 1994), but the author knows of no theoretical justification for expecting such scaling. A more sophisticated analysis requires improved profile information in MST as well as a more detailed understanding of the ion energy flow channel. In summary, confinement scaling is in rough agreement with the expectation that stochastic, convective transport dominates the energy losses in MST given the observation that the fluctuation amplitude is only weakly dependent on current and density, that radiation losses are constant above a threshold value of I/N, and under the assumption that the dependence of the resistance anomaly on current results from changes in the ion heating in a way that does not affect electron heating.

*4.8 Conclusions of Transport Measurements*

The results of measurements presented in this work and supported by the results of Fiksel, *et al.* (Fiksel, 1994), indicate that inside of r/a~0.8 particle and energy transport in the RFP is dominated by magnetic fluctuation induced transport. The results are consistent with the expectation from 3D MHD codes (Schnack, 1985) that the magnetic flux surfaces in the RFP are substantially destroyed inside the reversal layer. Despite the large magnetic fluctuations and resulting global stochasticization of the field, the thermal confinement in the RFP is more than an order of magnitude better than a naive application of the heuristic model put forward by Rechester and Rosenbluth would predict. The results of this work indicate that the thermal transport is dominated by convective loss of fast electrons, the energy loss rate being determined by the rate at which particles are lost. A radial ambipolar electric field limits electron losses to the ion stochastic loss rate, determining the overall particle diffusion *and* effective thermal diffusivity of 50-100 $m^2/s$.

## References

S. Assadi, S.C. Prager, and K.L. Sidikman, "Measurement of nonlinear mode coupling of tearing fluctuations," **69**, 281 (1992).

S. Assadi, "Measurement of magnetic turbulence structure and nonlinear mode coupling of tearing fluctuations in the Madison Symmetric Torus reversed field pinch," Ph.D. thesis, University of Wisconsin-Madison (1994).

J.M. Beall, Y.C. Kim, and E.J. Powers, "Estimation of wavenumber and frequency spectra using fixed probe pairs," J. Appl. Phys. **53**, 3933 (1982).

C.W. Barnes and J.D. Strachan, "Sawtooth oscillations in the flux of runaway electrons to the PLT limiter," Nucl. Fusion **22**, 1090 (1982).

C.W. Barnes and J.D. Strachan, "Measurements of fluctuations in the flux of runaway electrons to the PLT tokamak limiter," Phys. Fluids **26**, 2668 (1983).

J.D. Callen, "Drift-wave turbulence effects on magnetic structure and plasma transport in tolamaks," Phys. Rev. Lett. **39**, 1540 (1977).

P.J. Catto, J.R. Myra, P.W. Wang, A.J. Wootton, and R.D. Bengtson, "Estimating the runaway diffusion coefficient in the TEXT tokamak from shift and externally applied resonant magnetic-field experiments," Phys. Fluids B **3** 2038 (1991).

G.G. Craddock and P.H. Diamond, "Theory of shear suppression of edge turbulence by externally driven radio-frequency waves," Phys. Rev. Lett. **67**, 1535 (1991).

D.J. Den Hartog, A.F. Almagri, R.J. Fonck, S.C. Prager, and J.S. Sarff, "Measurement of flow velocity fluctuations and the MHD dynamo in the MST reversed-field pinch," Bull. Am. Phys. Soc. **38**, 1979 (1993) and Wisconsin Plasma Physics Report PLP#1131 (1993).

G. Fiksel, S.C. Prager, W. Shen, and M. Stoneking, "Measurement of magnetic fluctuation induced energy transport," Phys. Rev. Lett. **72**, 1028 (1994).

H.P. Furth, J. Killeen, and M.N. Rosenbluth, "Finite-resistivity instabilities of a sheet pinch," **6** 459 (1963).

R.W. Harvey, M.G. McCoy, J.Y. Hsu, and A.A. Mirin, "Electron dynamics associated with stochastic magnetic and ambipolar electric fields," Phys. Rev. Lett. **47**, 102 (1981).

S. Hokin, A. Almagri, M. Cekic, B. Chapman, N. Crocker, D.J. Den Hartog, G. Fiksel, J. Henry, H. Ji, S. Prager, J. Sarff, E. Scime, W. Shen, M. Stoneking, and C. Watts, "Reversed-field pinch studies in the Madison Symmetric Torus," J. of Fusion Energy **12**, 281 (1993).

S. Hokin, A. Almagri, M. Cekic, B. Chapman, N. Crocker, D.J. Den Hartog, G. Fiksel, J. Henry, D. Holly, H. Ji, S. Prager, J. Sarff, W. Shen, M. Stoneking, and C. Watts, "Global confinement and edge transport measurements in the MST

reversed-field pinch," in *Proceedings of the 20th EPS Conf. on Controlled Fusion and Plasma Physics*, Lisboa, Portugal (1993b)

S. Hokin, "A particle transport model with neutrals," Wisconsin Plasma Physics Report PLP#1048 (1989).

H. Ji, H. Toyama, K. Miyamoto, S. Shinohara, and A. Fujisawa, "Fluctuation and electron-heat transport in a reversed-field pinch," Phys. Rev. Lett. **67**, 62 (1991).

H. Ji, private communication (1992).

R.H. Kraichnan, "Inertial-range spectrum of hydromagnetic turbulence," Phys. Fluids **8**, 1385 (1965).

J.A. Krommes, C. Oberman, and R.G. Kleva, "Plasma transport in stochastic magnetic field. part 3. kinetics of test particle diffusion," J. Plasma Phys. **30**, 11 (1983).

R.J. LaHaye, T.N. Carlstrom, R.R. Goforth, G.L. Jackson, M.J. Schaeffer, T. Tamano, and P.L. Taylor, "Measurements of magnetic field fluctuations in the OHTE toroidal pinch," Phys. Fluids **27**, 2576 (1984).

Y.L. Ho and S.C. Prager, "Nonlinear reversed-field pinch dynamics with nonideal boundaries," Phys. Fluids B **3**, 3099 (1991).

P.C. Liewer, "Measurements of microturbulence in tokamaks and comparisons with theories of turbulence and anomalous transport," Nucl. Fusion **25**, 543 (1985).

N. Mattor, P.W. Terry, and S.C. Prager, "Anomalous ion heating from the dynamo in a reversed-field pinch," Comments on Plasma Phys. and Contr. Fusion, **15**, 65 (1992).

R.A. Nebel, E.J. Caramana, and D.D. Schnack "The role of m=0 modal components in the reversed-field-pinch dynamo in the single fluid magnetohydrodynamics model," Phys. Fluids B **1**, 1671 (1989).

E.J. Powers, J.Y. Hong, and C.P. Ritz, *Reference Guide for Intelligent Signal Analysis*, Intelligent Signal Processing v. 3.1, Austin TX (1988).

A.B. Rechester and M.N. Rosenbluth, "Electron heat transport in a tokamak with destroyed magnetic surfaces," PRL **40**, 38 (1978).

T.D. Rempel, C.W. Spragins, S.C. Prager, S. Assadi, D.J. Den Hartog, and S. Hokin, "Edge electrostatic fluctuations and transport in a reversed-field pinch," Phys. Rev. Lett. **67**, 1438 (1991).

M.N. Rosenbluth, R.Z. Sagdeev, J.B. Taylor, and G.M. Zaslavski, "Destruction of magnetic surfaces by magnetic field irregularities," Nucl. Fusion **6**, 297 (1966).

W.L. Rowan, C.C. Klepper, C.P. Ritz, R.D. Bengtson, K.W. Gentle, P.E. Phillips, T.L. Rhodes, B. Richards, and A.J. Wootton, "Global particle confinement in the Texas Experimental Tokamak," Nucl. Fusion **27**, 1105 (1987).

J.S. Sarff, S. Assadi, A.F. Almagri, M. Cekic, D.J. Den Hartog, G. Fiksel, S.A. Hokin, H. Ji, S.C. Prager, W. Shen, K.L. Sidikman, and M.R. Stoneking, "Nonlinear coupling of tearing fluctuations in the Madison Symmetric Torus," Phys. Fluids B **5**, 2540 (1993).

J.A. Schmidt, "Plasma convection in a toroidal octupole," Phys. Rev. Lett. **24**, 721 (1970).

D.D. Schnack, E.J. Caramana, and R.A. Nebel, "Three-dimensional magnetohydrodynamic studies of the reversed-field pinch," Phys. Fluids **28**, 1305 (1985).

E. Scime, S. Hokin, N. Mattor, and C. Watts, "Ion heating and magnetihydrodynamic dynamo fluctuations in the reversed-field pinch," Phys. Rev. Lett. **68**, 2165 (1992a).

E. Scime, M. Cekic, D.J. Den Hartog, S. Hokin, D. Holly, and C. Watts, "Ion heating and magnetihydrodynamic dynamo fluctuations in the reversed-field pinch," Phys. Fluids B **4**, 4062 (1992b).

W. Shen, R.N. Dexter, S.C. Prager, "Current-density fluctuations and ambipolarity of transport," Phys. Rev. Lett. **68** 1319 (1992).

W. Shen and J.C. Sprott, "Modified polynomial function model for reversed field pinches," Phys. Fluids B **3**, 1225 (1991).

D. Sinitsyn and S. Hokin, "Particle transport measurements in the MST reversed-field pinch," Bull. Am. Phys. Soc. **38**, 1978 (1993) and Wisconsin Plasma Physics Report PLP#1138.

M.R. Stoneking, S.A. Hokin, W. Shen, and G. Fiksel, "Fast electron equilibrium distribution and particle transport at the edge of MST," Bull. Am. Phys. Soc.**37**, 1606 (1992), and Wisconsin Plasma Phys. Report PLP#1099 (1992).

T. Uckan, C. Hidalgo, J.D. Bell, J.H. Harris, J.L. Dunlap, G.R. Dyer, P.K. Mioduszewski, J.B. Wilgen, C.P. Ritz, A.J. Wootton, T.L. Rhodes, and K. Carter, "ATF edge plasma turbulence studies using a fast resiprocating Langmuir probe" J. Nucl. Mater. **176**, 693 (1990).

R.E. Waltz, "Magnetic fluctuations, ambipolarity, charge filamentation, and plasma rotation in tokamaks," Phys. Fluids **25**, 1269 (1982).

P.G. Weber, K.F. Schoenberg, J.C. Ingraham, G. Miller, R.W. Moses, C.P Munson, R.A. Nebel, M.M. Pickrell, G.A. Wurden, H.Y.W. Tsui, C.P. Ritz, R. Veerasingam, E. Klevans, and R.F. Ellis, "Confinement studies in the ZT-40M reversed field pinch," in *Proceedings of the 13th Int. Conf. on Plasma Physics and Controlled Fusion*, IAEA Vienna, vol. 2, p. 509 (1990).

A.J. Wootton, B.A. Carreras, H. Matsumoto, K. McGuire, W.A. Peebles, Ch.P. Ritz, P.W. Terry, and S.J. Zweben, "Fluctuations and anomalous transport in tokamaks," Phys. Fluids B **2**, 2879 (1990).

Z. Yoshida, private communication (1993).

B. Zurro, C. Pardo, J. Vega, F. Medina, and A. Rodriguez-Yunta, "Evidence for magnetic fluctuations as the electron heat-loss mechanism in the core of the TJ-1 tokamak," in *Proceedings of the 20th EPS Conf. on Controlled Fusion and Plasma Physics,"* Lisbon, vol. 17C, p.I-36 (1993).

# 5. Summary and Conclusions

## *5.1 Fast electron generation*

Measurements of the fast electron population in MST and presented in this work (chapter 3) support the thesis that a kinetic dynamo mechanism (Jacobson, 1984) for sustaining the poloidal current is not dominantly operative in MST. The fast electron population at the edge of MST, measured with two electron energy analyzer (EEA) probes and a thermocouple calorimeter, is well fit by a drifted-Maxwellian distribution with a parallel temperature comparable to but not greater than the central electron temperature of about 100 eV (at low plasma current $I_p$<250 kA). The distribution is observed to have a drift velocity of about $2x10^6$ m/s, and a density that is 10-20% of the edge bulk electron density. The current carried by the fast electron distribution matches the total parallel current measured with an insertable Rogowski probe independent of plasma density. A careful cross-calibration of the EEA, the calorimeter, and the fast pyrobolometer yielded a measurement of the fast electron perpendicular temperature that is 30 eV, much smaller than the parallel temperature and comparable to the edge bulk electron temperature.

The measurement of the cold perpendicular fast electron temperature represents a significant piece of evidence against a kinetic dynamo mechanism in MST. The kinetic dynamo relies on the transport of fast electrons from the core region where they are accelerated by the applied toroidal electric field to the edge (through a stochastic magnetic field). The perpendicular energy

distribution of the fast electrons generated by such a mechanism should reflect the core electron distribution.

A second piece of experimental evidence against the KDT mechanism in MST is the observation reported here that the fast electron number density is insensitive to the ratio of the applied electric field to the critical electric field for runaway production. A calculation of the runaway electron source function for high and low density cases investigated in MST predicts a large difference in the runaway (or slideaway) electron source rate, being much larger at low density. However, the experiment shows relatively constant fast electron density, actually *decreasing* slightly at lower density, opposite to the trend predicted by a slideaway phenomenon.

A final piece of evidence against the KDT in MST is provided by the experimental measurement of the fast electron diffusion coefficient of about 500 $m^2/s$. Coupling this measurement with the fast electron collision frequency (from the measured temperature) yields a radial random walk step size in the stochastic magnetic field of about 4 cm in one 90° collision time. Because the radial wander between collisions is much smaller than the minor radius, a fast electron that is accelerated parallel to the field in the core region loses its parallel momentum many times over before reaching the edge region. The KDT requires collisionless transport of field-aligned electron momentum from the core region to provide the edge poloidal current. The KDT mechanism is not likely to be operative in MST due to the relatively collisional (on a particle confinement time scale) nature of the fast electron population.

*5.2 Magnetic fluctuation induced particle transport*

It has long been suspected that the high level of magnetic fluctuations observed in the RFP may be responsible for plasma transport. Measurements reported here confirm that inside r/a~0.8, the magnetic fluctuation induced transport of fast electrons can account for all the observed particle losses. Moreover, the observed energy transport due to magnetic fluctuations is consistent with the convective losses carried by the fast electrons. The measured particle transport rate (i.e. the diffusion coefficient) is however significantly smaller than the heuristic model for fast (test) electron transport in stochastic field would predict (Rechester, 1978). A resolution of this apparent conflict is suggested: the stochastic transport of fast electrons creates a radial ambipolar electric field that acts to equilibrate electron and ion transport rates. The magnitude of the electric field necessary to suppress electron transport (Harvey, 1981) is consistent with the observed toroidal rotation speed of the MST plasma if the toroidal rotation is dominated by the ExB drift and the ion diamagnetic drift.

*5.3 Suggestions for further work*

The results presented in this work point to several lines of continued research in the RFP.

The most obvious next step in investigating the nature of fast electron generation and transport is to perform a kinetic calculation based on the results presented here. The calculation is similar to the ones done by Harvey *et. al.*,

(Harvey, 1981), for the tokamak and by Schoenberg and Moses (Schoenberg, 1991) for the RFP and the analytic calculation done by Catto, *et al.*, (Catto, 1994). The kinetic equation to be solved is the one solved by Harvey, *et al.*:

$$\frac{\partial f}{\partial t} - \frac{eE_{\parallel}(r)}{m}\frac{\partial f}{\partial v_{\parallel}} = \frac{|v_{\parallel}|}{r}\mathcal{L} r D_m(r) \mathcal{L} f + C\{f\}, \qquad (5.1)$$

where $\mathcal{L} = (\partial/\partial r) - \left(eE_A(r)/mv_{\parallel}\right)\left(\partial/\partial v_{\parallel}\right)$. This equation includes the effects of an ambipolar electric field, diffusion in a stochastic magnetic field, parallel acceleration (including the effects of the dynamo electric field), and collisions, all of which have been seen to be important in the parameter regime ecountered in MST. The results will differ from those of Harvey, *et. al.*, because of the difference in magnetic fluctuation level and the profile of the parallel electric field. They will differ from Catto, *et. al.*, and Shoenberg and Moses in the inclusion of the ambipolar electric field.

Further measurements of the magnetic fluctuation induced transport of fast electrons should be done in a variety of discharge conditions. This is a challenging prospect as it requires construction of probes that can survive at deep insertion in discharges with higher plasma current than those investigated to date. Of particular interest will be the effects on the measured transport with the application of d.c. helicity injection. It is expected that poloidal current injection at the edge of the RFP will stabilize the tearing modes, reduce the fluctuations and hence the transport. Results of transient poloidal current drive (Sarff. 1994) are suggestive that fluctuations may be reduced sufficiently to create regions of good flux surfaces with significant reduction of transport.

More work can be done on the scaling of confinement in the RFP in light of the confirmation that magnetic fluctuations are important in determining the confinement properties. A careful investigation of the dependence of the magnetic fluctuation level on plasma current and density is critical to this program. Future measurements of the electron temperature profile with a multi-point Thomson scattering system, the $Z_{eff}$ profile, and more complete FIR interferometer chord set for density profile measurements will provide crucial information on the electron energy confinement channel.

Tangential to the present work, but of great interest is the nature of the high frequency magnetic fluctuations in the RFP. The possible existence of a nonlinear cascade (or inertial range) in the magnetic turbulence should be investigated. A careful measurement of the high frequency dispersion relation, and the nonlinear coupling of the high frequency modes can be made with a combination of insertable probes and the dense array of coils mounted to the MST vacuum vessel. The scaling of the high frequency spectrum with plasma current (i.e. $B_o$) and density (i.e. $v_A$ ) should also be performed.

## References

P.J. Catto, J.R. Myra, and A.J. Wootton, "Analytic model for the runaway distribution function in the presence of spatial diffusion," Phys. Plasmas **1**, 684 (1994).

R.W. Harvey, M.G. McCoy, J.Y. Hsu, and A.A. Mirin, "Electron dynamics associated with stochastic magnetic and ambipolar electric field," Phys. Rev. Lett. **47**,102 (1981).

A.R. Jacobson and R.W. Moses, "Sustainment dynamo reexamined: nonlocal electrical conductivity of a plasma in a stochastic magnetic field," Phys. Rev. Lett. **52**, 2041 (1984).

A.B. Rechester and M.N. Rosenbluth, "Electron heat transport in a tokamak with destroyed magnetic surfaces," Phys. Rev. Lett. **40**, 38 (1978).

J.S. Sarff, S.A. Hokin, H. Ji, S.C. Prager, and C.R. Sovinec, "Fluctuation and transport reduction in a reversed field pinch by inductive poloidal current drive," submitted to Phys. Rev. Lett. (1994).

K.F. Schoenberg and R.W. Moses, "Magnetic turbulent electron transport in the reversed-field pinch," Phys. Fluids B **3**, 1467 (1991).